Titre: Title:	Development of a Multi-Physics Numerical Framework for Lithium-Ion Cell Thermal Runaway
Auteur: Author:	Mathieu Louis Thierry Goureau
Date:	2024
Type:	Mémoire ou thèse / Dissertation or Thesis
Référence: Citation:	Goureau, M. L. T. (2024). Development of a Multi-Physics Numerical Framework for Lithium-Ion Cell Thermal Runaway [Mémoire de maîtrise, Polytechnique Montréal]. PolyPublie. https://publications.polymtl.ca/62491/

URL de PolyPublie: PolyPublie URL:	https://publications.polymtl.ca/62491/
Directeurs de recherche: Advisors:	Bruno Savard, & Étienne Robert
Programme: Program:	Génie mécanique

POLYTECHNIQUE MONTRÉAL
affiliée à l'Université de Montréal

Development of a Multi-Physics Numerical Framework for Lithium-Ion Cell Thermal Runaway

MATHIEU LOUIS THIERRY GOUREAU
Département de génie mécanique

Mémoire présenté en vue de l'obtention du diplôme de *Maîtrise ès sciences appliquées*
Génie mécanique

Décembre 2024

POLYTECHNIQUE MONTRÉAL
affiliée à l'Université de Montréal

Ce mémoire intitulé :

Development of a Multi-Physics Numerical Framework for Lithium-Ion Cell Thermal Runaway

présenté par **Mathieu Louis Thierry GOUREAU**
en vue de l'obtention du diplôme de *Maîtrise ès sciences appliquées*
a été dûment accepté par le jury d'examen constitué de :

David VIDAL, président
Bruno SAVARD, membre et directeur de recherche
Etienne ROBERT, membre et codirecteur de recherche
Julian SELF, membre

DEDICATION

À Sabine et mes parents.

ACKNOWLEDGEMENTS

I would like to express my deepest gratitude to Professor Bruno Savard, my research director. Your guidance, insights, and encouragement throughout the project were sincerely appreciated and enabled me to showcase the best of my work.

I would also like to warmly thank Professor Étienne Robert, my co-director. Your advice and input at various stages of the project truly helped me to make progress. Thank you for believing in me during these two years.

I am also thankful to Philippe Versailles, PhD, whose support and expertise were a valuable addition to my work.

I am also grateful to Safran Tech and Safran Electrical and Power for making this project possible and particularly to Aurélie Boisard, Fernandra Vendrame, and Hugo Girodon for their constructive feedback during our regular meetings. I also acknowledge funding from the Natural Science and Engineering Research Council of Canada (Alliance Program) and the Ministère de l'Économie, de l'Innovation et de l'Énergie (InnovÉÉ Program).

Last, but not least, I want to thank all my labmates: Oliver J, William, Luisa, Arona, Nammuni, Marc-André, Alexis, Marie-Laure, Mathieu CP, Olivier C, Xavier, Martin, Pierre, Gabriel, Lucas, and Taylor. You all made these past two years truly wonderful, and I hope to see you again on one side of the ocean or the other. A special thanks to Arona, Alexis, Nammuni, Marc-André, and Marie-Laure for working alongside me on the FRIBaCo project; burning (whether real or simulated) Li-ion cells with you was a pleasure.

Merci à mes parents et mes frères pour leur soutien sans faille pendant ces deux ans et demi de l'autre côté de l'Atlantique. Un merci tout particulier à Virgile pour m'avoir accompagné durant tout ce temps. Je remercie également chaleureusement mes colocataires et tous mes amis avec qui j'ai pu partager cette belle aventure.

Enfin, merci à Sabine, sans qui ce mémoire n'aurait jamais pu voir le jour.

RÉSUMÉ

L'emballement thermique est le phénomène où une batterie au lithium libère soudainement de grandes quantités de chaleur en raison de réactions chimiques internes incontrôlées. Ce phénomène s'accompagne de la libération de gaz inflammables, créant d'importants risques d'incendie, notamment dans les moyens de transport électriques qui regroupent plusieurs centaines, voire milliers, de ces cellules. Si l'emballement se propage aux cellules voisines, il peut entraîner une réaction en chaîne dans l'ensemble du bloc-batterie.

Dans ce mémoire, une revue de littérature sur l'emballement thermique et sa modélisation numérique est présentée. Le phénomène d'emballement thermique est étudié sous le prisme des batteries lithium-ion cylindriques 18650 utilisant la technologie NMC pour la cathode. Cette revue se divise en deux parties. La première décrit les causes et les différentes étapes de l'emballement thermique, ainsi que les dispositifs de sécurité intégrés par les constructeurs pour prévenir et limiter ce phénomène. Une vue d'ensemble de la génération de gaz est également fournie. Dans la seconde partie, l'état de l'art de la modélisation numérique de l'emballement thermique est présenté. Les modèles utilisés dans la littérature pour représenter les différents phénomènes sont détaillés.

Un modèle numérique de l'emballement thermique pour une batterie lithium-ion 18650 NMC est ensuite développé à l'aide du logiciel commercial ANSYS Fluent. Les principales équations et les différents modèles employés sont décrits. De plus, la géométrie et les choix d'implémentation sont explicités. Les différents modèles de combustion disponibles dans Fluent sont étudiés avant la réalisation d'une simulation complète de l'emballement thermique et sa comparaison avec des résultats expérimentaux. Finalement, le modèle est utilisé pour modéliser deux batteries simultanément.

Ce travail montre qu'il est possible de réaliser une simulation numérique capturant les principales étapes du phénomène d'emballement thermique à l'aide des outils disponibles dans ANSYS Fluent. Le modèle présenté intègre les principaux phénomènes, tels que la génération de gaz et de chaleur, le dégazage, la combustion et la propagation, tout en étant adaptable. La modélisation d'un bloc batterie est également possible, avec chaque cellule capable d'entrer individuellement en emballement thermique.

ABSTRACT

Thermal runaway is a phenomenon in which a lithium battery releases large amounts of heat and gas due to uncontrolled internal chemical reactions. This catastrophic failure is usually associated with the release of flammable gases that can auto-ignite or be ignited, creating significant fire risks. This is especially significant in the electric transport industry where hundreds or even thousands of these cells are assembled in battery packs. If thermal runaway spreads to neighboring cells, it can trigger a chain reaction throughout the battery pack.

In this master thesis, a literature review on thermal runaway and its numerical modeling is presented. It is focused on thermal runaway in cylindrical 18650 lithium-ion batteries with an NMC cathode. The review is divided into two sections. The first part provides a brief description of cylindrical cells, describes the trigger mechanisms and stages of thermal runaway, and details the safety mechanisms added to prevent and mitigate this phenomenon. An overview of the gas generation mechanism and the composition released by NMC cells is also provided. In the second part, the state of the art in numerical modeling of thermal runaway is presented, with a detailed look at the models used in the literature to represent various phenomena involved.

A numerical model of thermal runaway for an NMC 18650 lithium-ion battery is then developed using the commercial software ANSYS Fluent. The governing equations and models employed are described, along with the geometry and configuration choices. The different combustion models available in Fluent are investigated before running a full thermal runaway simulation and comparing the results with experimental data. Finally, the model is scaled up to simulate two batteries simultaneously.

Key results show that the model predicts that the cell undergoes thermal runaway following an initial pressure release at 152.7°C, reaches a maximum temperature of 472.8°C, and releases 83.17 kJ of energy. This work demonstrates that accurate numerical modeling of thermal runaway can be achieved using the models available in ANSYS Fluent. The model presented incorporates key phenomena, including gas and heat generation, venting, combustion, and propagation, while remaining adaptable and scalable. The proof of concept of modeling an entire battery pack with each cell capable of independently undergoing thermal runaway is shown.

TABLE OF CONTENTS

LIST OF TABLES

LIST OF FIGURES

LIST OF SYMBOLS AND ACRONYMS

CAD	Computer-Aided Design
CFD	Computational Fluid Dynamics
CHT	Coupled Heat Transfert
CT	Computed Tomography
CID	Current Interrupt Device
CRPD	Constant Drying Rate Period
DEC	Diethyl Carbonate
DMC	Dimethyl Carbonate
DO	Discrete Ordinates
DRDP	Decaying Rate Drying Period
EDC	Eddy Dissipation Concept
EMC	Ethyl Methyl Carbonate
EV	Electric Vehicle
FGM	Flamelet Generated Manifold
FR	Finite-Rate
FVM	Finite Volume Method
JR	jellyroll
LCO	Lithium Cobalt Oxide
LES	Large Eddy Simulation
LFP	Lithium Iron Phospahte
LIB	Lithium-Ion Battery
LMO	Lithium Manganese Oxide
NCA	Nickel Cobalt Aluminium
NMC	Nickel Manganese Cobalt
NPC	Non-premixed Combustion
PDF	Probability Density Function
PE	Polyethylene
PP	Polypropylene
PPC	Partially Premixed Combustion
PTC	Positive Temperature Coefficient
RANS	Reynold Averaged Navier-Stokes
S2S	Surface-to-Surface
SDF	Steady Diffusion Flamelet

SEI	Solid Electrolyte Interphase
SOC	State Of Charge
ST	Species Transport
TCI	Turbulence-Chemistry Interaction
TR	Thermal Runaway
UDF	User Defined Function
VLE	Vapour Liquid Equilibrium

LIST OF APPENDICES

CHAPTER 1 INTRODUCTION

Economic and environmental incentives have driven the electrification of the transport industry, positioning it as a key solution in the global effort to reduce carbon emissions and dependence on fossil fuels [1–3]. While low-carbon energy sources are available, the efficient storage of this energy remains a significant challenge [4]. In response, lithium-ion batteries (LIB), born in the early 1980s as the first rechargeable batteries using a non-aqueous electrolyte, have been developed over the past few decades as a superior alternative to other battery technologies, thanks to their high voltage, energy, and power density [5–7]. Lithium-ion batteries have rapidly expanded across a diverse range of applications, including consumer electronics, battery storage, and electric vehicles (EVs). As illustrated in Figure 1.1, the demand for LIBs has significantly increased in recent years, mostly driven by EVs [8], with forecasts predicting this trend to continue in the next decades [9].

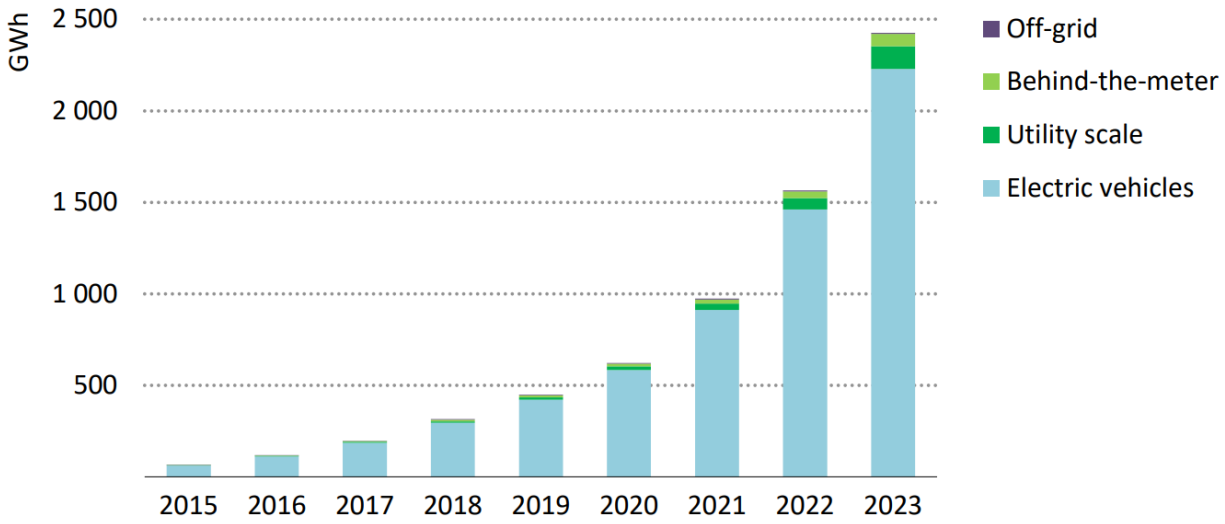

Figure 1.1 Lithium-ion battery demand in 2015-2023 [8]. "Off-grid", "Behind-the-meter" and "Utility scale" describe different types of battery storage. Licensed under CC BY 4.0

A lithium-ion battery stores and releases electrical energy based on redox (reduction-oxidation) reactions happening at its electrodes. Figure 1.2 presents the different components of a cell. It comprises two electrodes immersed in a liquid electrolyte and isolated with a separator. The positive electrode, known as the **cathode** is usually made of metal oxides while the negative one called **anode** is typically composed of graphite. The composition of the cathode varies based on the technology employed, with common examples including Manganese Cobalt Oxide (NMC) and Nickel Cobalt Aluminum Oxide (NCA). Additionally, electrical

contact is assured between the electrodes and the current collector made of copper or aluminum using polymer binders [10]. The liquid **electrolyte** is usually composed of lithium salt (lithium hexafluorophosphate $LiPF_6$) mixed with alkyl carbonates such as dimethyl carbonate (DMC), ethyl methyl carbonate (EMC), or diethyl carbonate (DEC) [11]. The **separator** is crucial for preventing short circuits inside the battery. It is composed of a microporous plastic membrane, usually polyethylene (PE) or polypropylene (PP), isolating the electrodes while letting the lithium ions pass [12].

During the charging process, a lithium ion leaves the positive electrode and migrates through the electrolyte, releasing an electron that flows through the external circuit. Once the ion reaches the negative electrode (anode), it recombines with an electron. As redox reactions are reversible, this process is mirrored during the discharge [13]. This principle is summarized in Figure 1.2. During the first charging cycles, a **Solid Electrolyte Interphase** (SEI) layer is formed on the anode due to the decomposition of electrolyte compounds on its surface. This layer continues to grow throughout the battery's life leading to an irreversibly increased impedance and capacity loss [14].

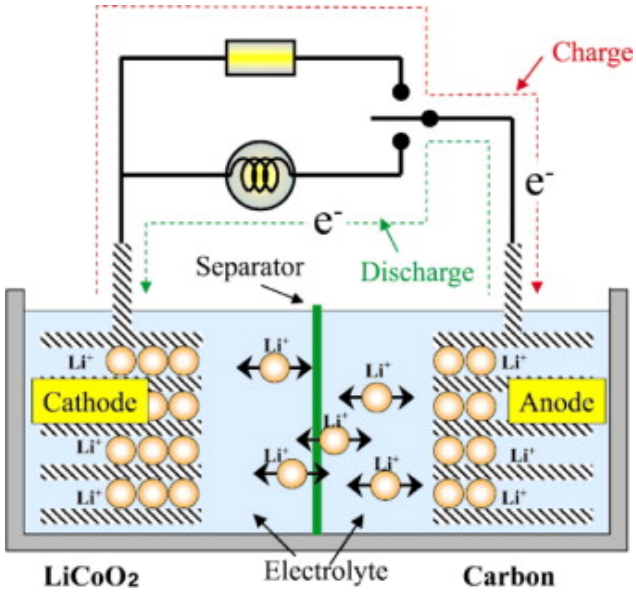

Figure 1.2 - Schematic of the working principle of a Li-Ion cell [15], reproduced with permission

Despite their undeniable advantages, Lithium-ion cells pose a significant fire safety risk due to their potential for thermal runaway (TR) [16]. Under abuse conditions, such as mechanical damage, exposure to high heat from a fire, short-circuiting, or an electrical surge, these cells can rapidly overheat, leading to safety and fire hazards as the cell generates toxic and flammable gases [13, 15].

A single cell is enough to pose a significant risk [17]. However, since one cell is insufficient to power electric means of transportation (such as EVs, e-bikes, and e-scooters), multiple cells are assembled into battery modules and packs, often containing thousands of cells, as shown in Figure 1.3. In this configuration, the TR phenomenon can propagate from cell to cell, potentially leading to a large-scale fire [18, 19].

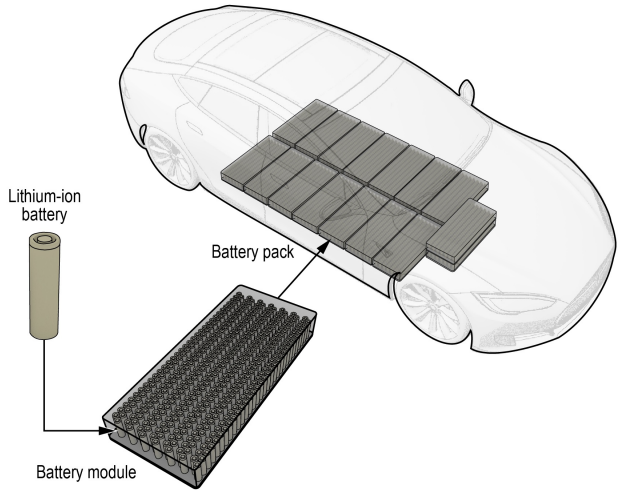

Figure 1.3 - Schematic of a battery pack inside an electric vehicle. Adapted from [20]

This work is motivated by the widespread adoption of lithium-ion technology for energy storage in the transportation industry, and the insufficient understanding of the TR phenomenon [16]. A deeper understanding is essential for accurately assessing the risks associated with lithium-ion batteries, and supporting the design of next-gen LIBs and EVs. This research is part of a project focused on applications in the aeronautic and aerospace industries, where risk assessment and mitigation are critical. This project aims to understand the phenomena that occur during the TR of cells, particularly the release of gases and their combustion, to develop numerical models.

In this context, experiments conducted at the cell or pack level provide valuable data on various processes, including heat generation, gas venting, energy release from combustion, and the propagation of TR within a battery pack. This data can be used to develop and validate numerical models to accurately simulate the TR to improve LIB safety and mitigation techniques at a lower cost. Numerical modeling is crucial for understanding and analyzing the underlying physical and chemical processes involved in a TR. It enables predicting future behavior under different conditions, saving time and resources compared to physical testing. It allows for rapid iteration and optimization of system design to mitigate the risks associated with TR. However, validating numerical models with experimental tests is important to

ensure accuracy and reliability.

The present work develops a multi-physics numerical framework for simulating TR in lithium-ion cells using ANSYS Fluent™. It includes the internal generation of heat and gaseous species, as well as their venting and combustion outside a fully charged, cylindrical, 18650-form factor (18 mm in diameter, 65 mm in height) lithium nickel-cobalt-manganese (NMC) cell undergoing thermal runaway triggered by overheating. The model is developed using sub-models already published in the literature and integrated into Fluent. The results will be compared with experimental data acquired in-house using calorimeters. Different combustion models are investigated based on their heat release rate calculation, ignition characteristics, and computational cost. Finally, a small battery pack is modeled to demonstrate the capacity of the model to capture TR propagation.

This master's thesis is organized into five chapters, beginning with this introduction. Chapter 2 reviews the existing literature on the thermal runaway phenomenon and its numerical modeling. Chapter 3 details the numerical approach, modeling methodology, and solver configuration. Chapter 4 presents an investigation of the combustion models, the primary results of the model, and their comparison with experimental data. Finally, it introduces a proof of concept using this model to simulate thermal runaway propagation within a battery pack. Chapter 5 discusses the model's limitations and future development, as well as the broader impact of this work.

CHAPTER 2 LITERATURE REVIEW

In this chapter, a literature review on thermal runaway and its numerical modeling, with a focus on cylindrical 18650 lithium-ion batteries using an NMC cathode is presented. The first section describes cylindrical cell structure, trigger mechanisms, stages of thermal runaway, safety features, and gas generation and composition in NMC cells, while the second section reviews state-of-the-art models used to represent the various phenomena involved in thermal runaway.

2.1 The thermal runaway phenomenon

Thermal runaway is the primary safety concern in LIBs. This complex phenomenon can occur in all shapes and types of LIBs; however, this section will focus specifically on cylindrical cells. An overview of this cell shape will be provided before describing the TR process, from the initial trigger to the quantity and composition of gas generated.

2.1.1 Cylindrical lithium-ion cells

Lithium-ion batteries can be categorized by their geometry into cylindrical cells, prismatic cells, pouch cells, or button cells [5, 21]. Recent research has primarily focused on the widely commercialized cylindrical cells due to their higher energy density and a wider range of applications [22–24]. The most common form factor of these cylindrical cells is 18 mm in diameter and 65 mm in height, commonly referred to as "18650 cells". The structure of this type of cell is shown in Figure 2.1 and can be divided into two parts: the top part and the jellyroll. The top part contains the positive terminal and safety features (safety vent and PTC disk), which will be discussed in Section 2.2, while the jellyroll holds the electrochemical materials introduced in Chapter 1.

Batteries are further categorized based on the active material of the cathode. The common technologies available on the market, along with their performance characteristics, are presented in Table 2.1. Lithium cobalt oxide (LCO) is primarily used in small electronic devices such as cell phones and laptops. Lithium manganese oxide (LMO) is a low-cost, safer option compared to other cathodes, but with lower energy density, making it a secondary choice for manufacturers, often used in power tools. Nickel manganese cobalt (NMC) is predominantly used in EVs outside of China and is expected to become the leading cathode material in the coming years. Nickel cobalt aluminum oxide (NCA) is utilized in Tesla's EVs and power tools,

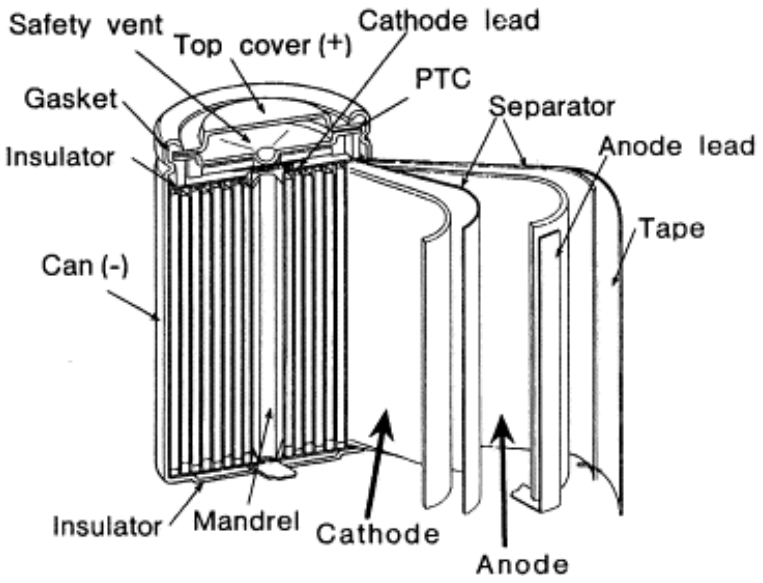

Figure 2.1 - Schematic of a cylindrical cell. The top part includes the top cover and safety features, while the jellyroll contains the anode, cathode, and separator. The liquid electrolyte is not shown but soaks the jellyroll, but other components essential to the cell's operation (insulator, leads, gasket) and manufacturing (mandrel) are included. Reproduced with permission [25]

while lithium iron phosphate (LFP) is commonly used in EVs in China and in applications requiring a long lifespan [26, 27].

Table 2.1 Cathode technologies with their performance. Adapted from [21]

Cell Type	**LCO**	**LMO**	**NMC**	**NCA**	**LFP**
Cathode active material	Lithium Cobalt Oxide	Lithium Manganese Oxide	Lithium Nickel Manganese Oxide	Lithium Nickel Cobalt Oxide	Lithium Iron Phosphate
Volumetric energy density (Wh/L)	320-500	290-340	490-580	480-670	160-260
Gravimetric Energy Density (Wh/kg)	110-180	100-120	180-210	180-250	80-120
Lifetime (cycle)	300-1000	1000-1500	500-1000	500-1000	2000-5000
Application	High Energy	High Power	High Energy and Power	High Energy and Power	Long lifespan

2.1.2 Description and causes of thermal runaway

During normal operating conditions such as charging and discharging, LIBs generate a small amount of heat that quickly dissipates to the environment. However, under specific abuse conditions [16, 28, 29], a point can be reached where the rate at which heat is produced inside the cell becomes more important than the rate at which it can be dissipated to the environment [13]. The internal temperature thus increases, accelerating the reactions and the rate at which they release heat, which further raises the temperature. At this point, the cell enters into thermal runaway. This cycle, illustrated in Figure 2.2 and known as the heat-temperature-reaction loop [16, 30], continues until failure. In the case of a Li-ion cell undergoing TR in an oxidative atmosphere, the endpoint will be the complete burning of the cell's combustible material. During this catastrophic failure, the cell typically goes through three distinct phases: internal heat and flammable gas generation, venting, and combustion.

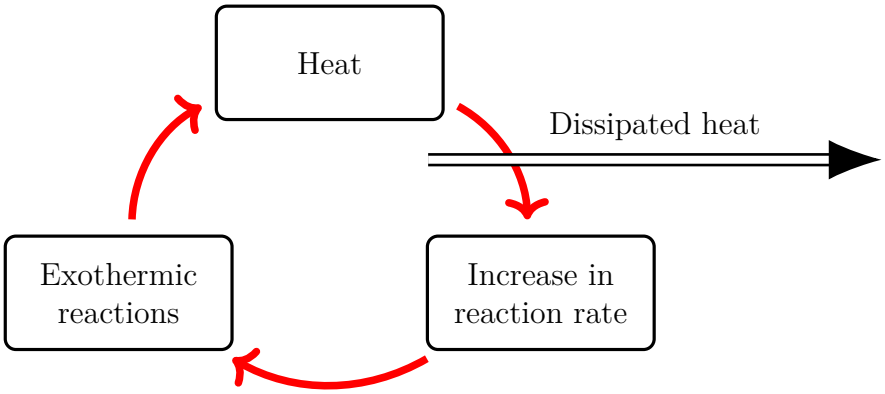

Figure 2.2 - Schematic representation of the heat-temperature-reaction loop. Adapted from [30]

The main trigger mechanisms leading to thermal runaway are [16, 28, 29]:

- **Mechanical abuse**: The cell is physically damaged, causing an internal short-circuit. This type of damage may occur from battery penetration or crushing.
- **Electrical abuse**: The cell is put under electrical stress. It can happen during the charge or discharge with a current surge or due to an external short circuit.
- **Thermal abuse**: The cell is overheating as it cannot dissipate the heat quickly enough. It is the direct cause of the TR as it can result from the previously mentioned triggers. It also occurs when the environment is a heat source (e.g., fire near the cell).

An internal short circuit caused by an internal defect can sometimes also cause TR but this phenomenon is usually the result of one of the trigger mechanisms above. Fundamentally, it occurs whenever the separator fails to prevent direct electrical contact between the cathode and the anode.

The sequence of major events during the thermal runaway of a cell under thermal abuse is chronologically presented (left to right) in Figure 2.3, where endothermic and exothermic reactions are shown in blue and red, respectively [15, 16, 31]. In the first stage, the environment is warmer and transfers heat to the cell, potentially leading to the evaporation of some of the electrolytes. A series of exothermic reactions occur in the second stage making the temperature of the cell higher than the environment. The second stage starts with the SEI layer decomposition (SEI-d) at a relatively low temperature, ranging from 100°C to 150°C. The decomposition of the SEI layer allows the lithium intercalated in the anode to react with the organic solvent of the electrolyte. This leads to the exothermic SEI regeneration (SEI-r)

which, as shown by the double-sided vertical arrow, is coupled to another reaction between the anode and the oxygen released from the decomposing cathode (O2-An). In parallel, as the temperature continues to creep up, the separator melts (Sep melting). This reaction being endothermic, it momentarily reduces the rate of increase of the cell temperature [8]. The exothermic decomposition of the electrolyte starts soon after (Elec), which produces flammable and toxic gases. As the threshold of the security vent is exceeded, a first venting occurs releasing the gases and liquid electrolyte, which marks the end of the Vapor-Liquid Equilibrium (VLE) inside the cell. If exposed to an ignition source or if their temperature is sufficiently high to trigger auto-ignition, these gases can burn when in contact with surrounding air, providing supplementary heat to the cell. Even if they do not, the exothermic decomposition reactions inside the cell can generate enough heat to reach a point where the separator collapses leading to an internal short-circuit (short). A violent rise in cell temperature follows as well as the ejection of solid particles (Solids). Additional exothermic reactions between the anode active material and the binder (An-B) coupled with reactions between the binder and the oxygen released from the cathode (O2-B) are triggered soon after the start of the third stage. Due to the high temperature, the current collector will melt (blue Alum box) toward the end of the third stage and resolidify (red Alum box) during the fourth, where all other internal exothermic reactions cease and the cell cools down. In an oxidizing atmosphere, a flame will typically be stabilized at the tip of the cell for as long as the gas is vented off.

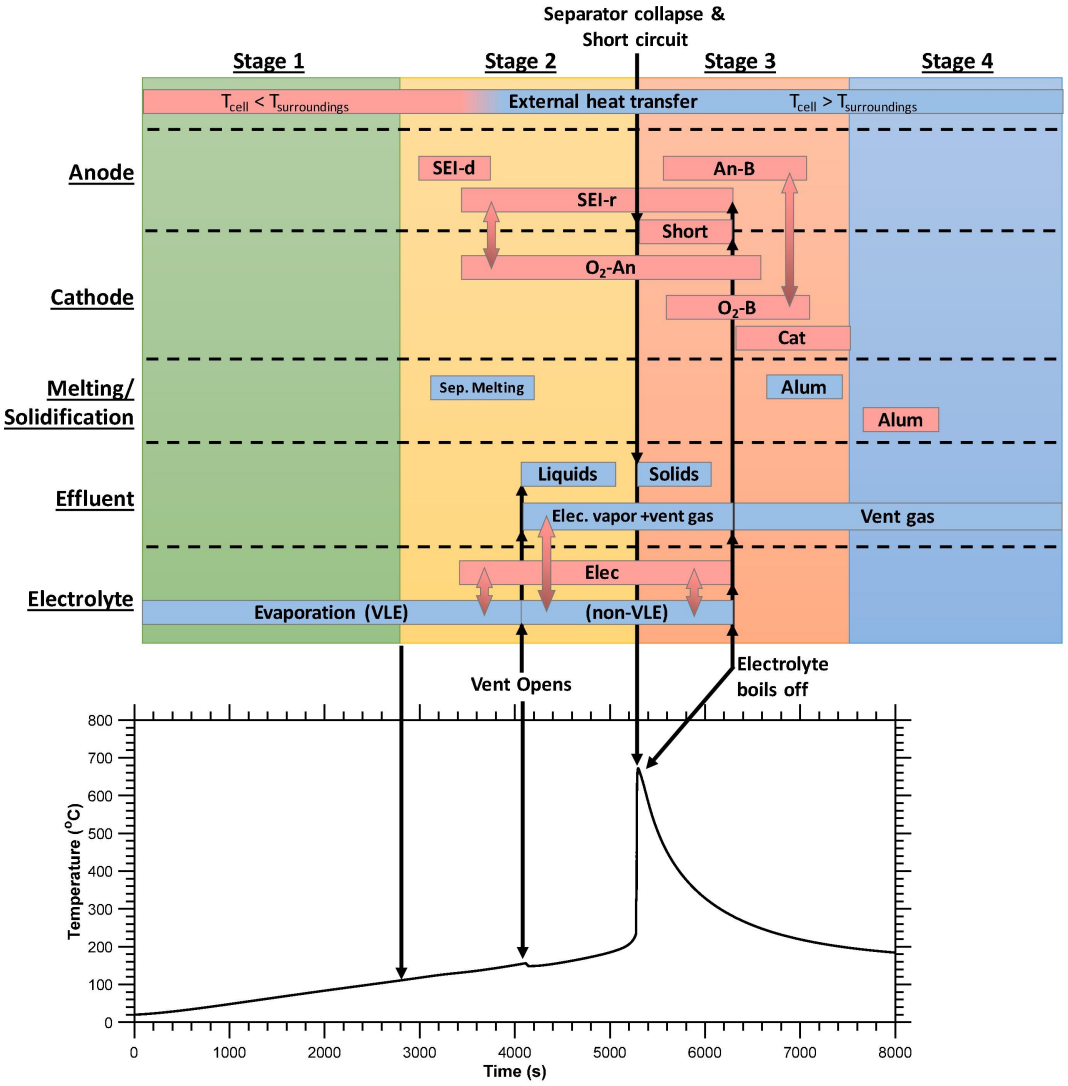

Figure 2.3 - Comparison between the sequence of events happening during TR and the cell temperature. Reactions in red are exothermic and reactions in blue endothermic [31], reproduced with permission. All acronyms and concepts are defined in the text above

2.1.3 Safety measures implemented in Li-ion cells

This section covers the safety devices incorporated into the cell by manufacturers to mitigate the risk of thermal runaway [32]. The features discussed here are internal to the cell, with external electronic and thermal management systems excluded. Table 2.2 provides an overview of the most common safety features, and Figure 2.4 illustrates the structure of the top cap of an 18650 cell.

For 18650 cells, two features are mandatory: the Current Interrupt Device (CID) and the top vent [32]. The CID is a physical disconnection between the positive terminal on the cell and the jellyroll. It consists of a flexible metallic membrane (top disk) welded to an electrical tab that is connected to the jellyroll. The top disk is insulated from the rest of the cell with plastic inserts. Under normal operating conditions, the electrical system remains closed, allowing current to flow from the jellyroll to the positive tab through the top disk. When internal pressure exceeds a defined threshold, the top disk is pushed upward, breaking the weld spot and disconnecting the cell. This disconnection is non-reversible, making the cell unusable after activation but stops the electrochemical internal reactions. The CID alone is not always enough to prevent thermal runaway [33]. To avoid an explosion, pressure inside the cell is released through vents. This venting process involves the top disk, which has a C-shaped notch creating a weak spot. When the internal pressure reaches a threshold, the top disk irreversibly bursts open, releasing the gases. The notch groove (scoring) mechanism is used in all cells for the top disk, but the depth, location, and orientation differ between manufacturers [32]. The thresholds for CID and vent activation vary among cells. The CID thresholds range from 0.92 MPa to 1.3 MPa, whereas vent activation occurs between 1.8 MPa and 2.3 MPa [34, 35].

Other non-mandatory safety devices include the Positive Temperature Coefficient (PTC) disk, the bottom vent, or a battery management system [32]. The PTC is an annular-shaped polymer disk that connects the top and bottom parts of the cell. Its resistance increases non-linearly when the temperature reaches a certain threshold (around 100°C). Although it is reversible and effective in inhibiting current surges due to its rapid response time, the PTC is not included in all 18650 cells because of the additional costs or design choices favoring high discharge current. A bottom vent can be added to the cell to further decrease the risk of sidewall ruptures, operating on the same principle as the top vent. Additionally, a battery management system can be integrated at the cell level. This protective circuit monitors the cell's voltage to prevent overcharging, over-discharging, and external short circuits. However, this solution is typically reserved for specific applications due to the increased manufacturing costs.

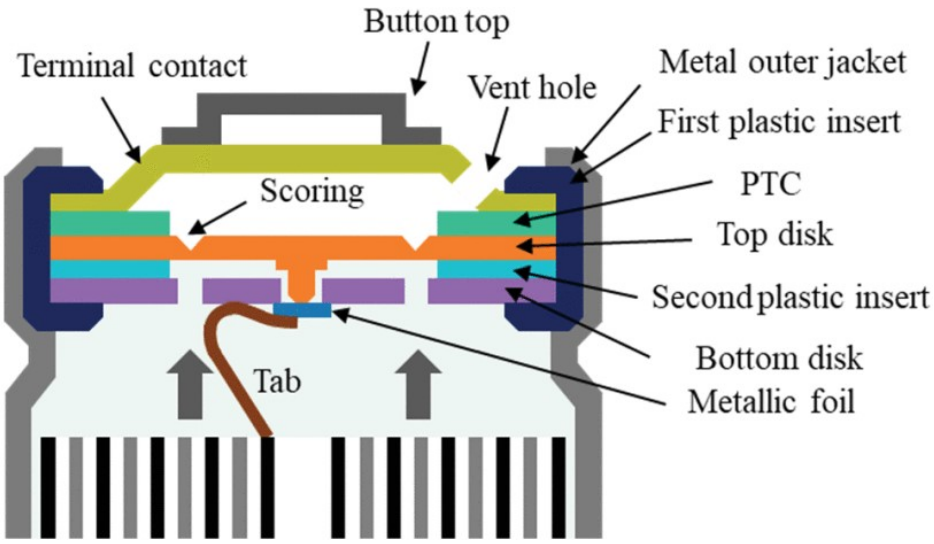

Figure 2.4 - Schematics of the top cap of a 18650 cell [32]. Licensed under CC BY 4.0

Table 2.2 - Protective devices in 18650 cells. Adapted from [32]

Protection device	Activation condition	Mandatory	Reversible	Safety Impact
CID	Internal pressure	Yes	No	Medium
Top Vent	Internal pressure	Yes	No	High
PTC	Internal temperature	No	Yes	Low
Bottom vent	Internal pressure	No	No	Medium
Protective circuit	Electrical load	No	Yes	High

2.1.4 Amount and composition of vented gas

Cells undergoing thermal runaway not only generate heat but also gases whose composition and quantity depend on the material chosen by the manufacturers for the different components. This generation of gases influences the hazard posed by fire, as the heat release rate is directly related to the composition and flow rate of the gas stream vented from cells during thermal runaway. Experimental studies have been conducted to quantify the amount and composition of the gas produced for different types of cells. The results are compiled in a meta-analysis on the heat and smoke emission during thermal runaway, based on research papers published between 2000 and 2021 [21]. In the analysis, the author studied, if provided, the composition and the total amount of gas emitted during TR from 37 different papers. The results are shown in Figure 2.5, which presents the amount of gas released per unit of energy as a function of the state of charge (SOC), ranging from fully discharged (0%) to overcharged (OC), for different battery shapes (cylindrical, pouch, and prismatic) and cathode active materials.

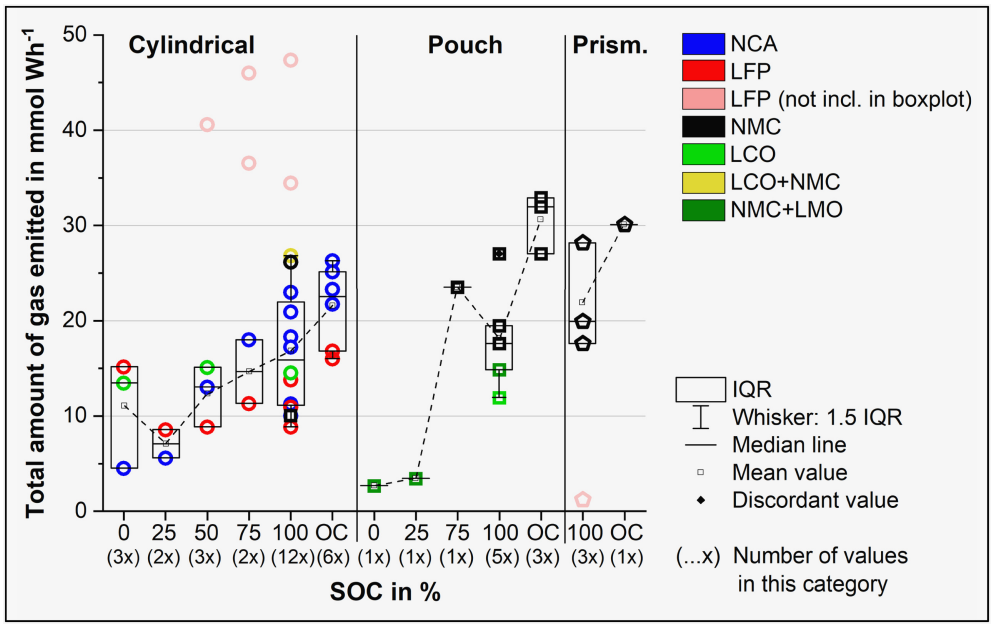

Figure 2.5 - Total amount of gas emitted during a thermal runaway per unit of energy stored in the cell from articles published in recent years [21]. Licensed under CC BY 4.0

The most studied shape is the cylindrical cell as they are widely available and standardized. For this shape, if the outlier data at the top of the chart (in pink) is excluded (they deviate strongly from the average without identified reasons), the amount of gas emitted increases with the SOC. Within the same range of SOC, the cathode material seems to have an impact on the total amount of gas emitted. NCA cells tend to produce a higher quantity of gas compared to other cathodes. The safest cathode in terms of quantity of produced gas is the LFP; an NCA cell at 50% SOC produces the same amount of gas as a LFP at 100% SOC. For pouch and prismatic cells, the small number of experimental studies makes it difficult to draw firm conclusions but the amount of gas seems to increase with SOC.

For the gas composition, all cell types and geometries release a significant amount of H_2, CO, and CO_2. Other flammable gases are also detected, mainly CH_4, C_2-hydrocarbons, and C_3-hydrocarbons [10, 28, 30, 36–42]. A small amount of O_2 is released during the cathode decomposition [10, 43]. In addition to the fire hazard, a cell undergoing thermal runaway can release toxic gases. Experimental studies have revealed that, beyond the danger posed by carbon monoxide (CO), there are also emissions of sulfur dioxide (SO_2), hydrogen chloride (HCl), hydrogen fluoride (HF), and nitrogen oxides (NO_x) [40, 44, 45]. Similarly to the quantity of produced gas, the SOC influences the composition. At low SOC (0-25%), nearly all the gas produced is CO_2. However, as the SOC increases, the proportion of CO_2 drops while the production of CO and H_2 increases [10].

Gas generation mechanism

Several mechanisms have been highlighted in the literature as possible sources of the various gases but uncertainties remain. Determining the origin of the different gases is challenging due to the venting happening through discrete, transient events that occur faster than the response time of modern measurement systems.

Based on the current understanding, H_2 is produced through the reaction of the binder with the cathode when the temperature is above 250°C. Sources of CO_2 include the combustion of other gases, the SEI decomposition, the electrolyte solvent's oxidation, and the lithium's reaction with alcohols. CO is generated through incomplete combustion and the reduction of CO_2 with the intercalated lithium at the anode. CH_4 is produced by the reduction of the electrolyte in the presence of H_2. The generation of C_2H_4 is partly due to the decomposition of the SEI and partly due to the reduction of the electrolyte at the anode [46]. Lastly, C_2H_6 is produced by the reduction of the electrolyte at the anode [36, 47]. For toxic gases, HF is produced during the breakdown of the cathode starting at 175°C, as well as from the reaction between the binder and the electrolyte and the decomposition of the lithium salt such as $LiPF_6$. $NI(CO)_4$ is formed when nickel is exposed to a CO environment at high temperatures [40]. Currently, the reactions leading to the formation of HCN are unknown.

Vented gas composition of NMC cells

This section will focus on cylindrical 18650 NMC cells. For these cells, the measured gas compositions from the literature are shown in Table 2.3 [36–38, 40]. Although all the tested batteries used an NMC cathode, the cells were sourced from different undisclosed manufacturers using different active material compositions. The cells were fully charged before inducing the TR, except for the work of Chen et al. [38] who investigated three pairs of batteries with different SOC, heating temperature, and power. In all cases, TR was induced by overheating the cell. At the time of writing, the literature does not cover abuse of 18650 NMC cells by penetration or overcharge. Gas chromatography (GC) connected to a custom test rig or an Accelerating Rate Calorimeter (ARC) was used in every test to measure the gas composition. Chen et al. [38] also used a mass spectrometer (MS).

Table 2.3 - Vented gas composition (% on a molar basis) for fully charged 18650 NMC cells, with the compositions averaged over multiple tests

Ref.	Number of tests x Number of cells	Detection method	H_2	CO_2	CO	CH_4	C_2H_2	C_2H_4	C_2H_6	C_3H_x
Golubkov et al. [36]	3 x 1	GC	30.8	41.2	13.0	6.8	n.a.	8.2	n.a.	n.a.
Yuan et al. [37]	3 x 1	GC	13.39	13.22	30.3	10.5	n.a.	0.1	0.21	0.52
Yuan et al. [37]	3 x 1	GC	12.54	19.91	28.06	12.9	<0.1	0.1	0.21	n.a.
Chen et al. [38]	3 x 1	GC-MS	15.25	29.86	7.26	5.70	0.09	4.3	0.54	0.9
Chen et al. [38]	3 x 1	GC-MS	22.41	24.95	9.9	7.5	0.1	6.0	0.77	0.80
Yan et al. [40]	1 x 10	GC	35.4	14.9	32.7	6.9	6.8	0.5	n.a.	1.0

The main species detected were H_2, CO, and CO_2, while lower concentrations of CH_4 and C_2H_4, and traces of other hydrocarbons were also found. Some toxic gases, particularly HF, HCN, or $NI(CO)_4$ were also detected [40]. The impact of SOC on the gas composition of 18650 NMC cells is currently unknown. Table 2.3 highlights the significant variability in gas composition measurements and the general lack of data regarding the temporal variation of both the composition and the flow rate of the gases vented by an NMC cell during TR.

2.2 Numerical modeling of the thermal runaway

This section presents the state of the art on the numerical modeling of thermal runaway in Li-ion cells. Numerical modeling is crucial for understanding and analyzing the underlying physical and chemical processes involved in a thermal runaway. It enables the prediction of future behavior under different conditions, saving time and resources compared to physical testing. It allows for rapid iteration and optimization of system design to mitigate the risks associated with thermal runaway.

Table 2.4 summarizes previous studies addressing the numerical modeling of TR. For each study, it is indicated whether each specific process of the thermal runaway is modeled, as

well as the geometry used. The geometry column specifies the dimensions and the number of cells included in the model. Heat generation is considered included when the cell can self-heat through internal reactions. The gas generation column indicates whether mechanisms for introducing gases into the domain are accounted for in the cell. The model is considered to have safety features when the top vent described in Section 2.1.3 is included. The combustion is included when gas phase reactions are modeled. Finally, the propagation is considered as modeled when all the heat transfer mechanisms needed to model TR propagation in a multi-cell configuration are included. For the solver column, "Fluent", "Comsol", and "Matlab" refer to the commercially available numerical solvers Ansys FLUENT®, COMSOL Multiphysics®, and MATLAB® respectively, while "AVBP" refers to the Large Eddy Simulation (LES) solver developed at CERFACS [48].

Table 2.4 - Numerical models of the thermal runaway published in the literature

Model	Year	Geo -metry	Heat genera-tion	Gas genera-tion	Safety features	Com -bustion	Propa -gation	Solver
Kim et al. [49]	2007	3D 1 cell	**Yes**	No	No	No	No	Fluent
Coman et al. [50]	2016	0D 1 cell	**Yes**	No	No	No	No	Comsol
Coman et al. [51]	2017	0D 1 cell	**Yes**	No	No	No	No	Comsol
Ostanek et al. [31]	2020	2D 1 cell	**Yes**	**Yes**	**Yes**	No	No	Matlab
Kim et al. [52]	2021	2D-axis 1 cell	**Yes**	**Yes**	**Yes**	**Yes**	No	Fluent
Mishra et al. [53]	2021	3D 25 cells	**Yes**	No	No	No	**Yes**	Fluent
Mishra et al. [54]	2022	3D 25 cells	**Yes**	No	No	**Yes**	**Yes**	Fluent
Cellier et al. [55]	2023	3D 1 cell	No	No	No	**Yes**	No	AVBP
Zhao et al. [47]	2023	2D-axis 1 cell	**Yes**	**Yes**	No	**Yes**	No	Fluent
Ostanek et al. [56]	2023	3D 1 cell	**Yes**	**Yes**	**Yes**	No	**Yes**	Fluent
Zhang et al. [57]	2023	3D 1 cell	**Yes**	**Yes**	**Yes**	**Yes**	**Yes**	Fluent
Ostanek et al. [58]	2024	3D 25 cell	No	No	No	**Yes**	**Yes**	Fluent

The literature reviewed covers a range of models using different approaches and solvers to model the thermal runaway. Recent articles adopt a Reynolds-Averaged Navier Stokes (RANS) approach to solve the flow field outside the cell, with Ansys Fluent as the main solver as it can handle every aspect of the studied phenomenon. Cellier et al. [55] is an exception, choosing to use an LES approach with AVBP. In the RANS approach, the governing equations are derived by Reynolds-averaging the instantaneous equations. This requires additional modeling, particularly for turbulence and combustion, to close the model. In contrast, the LES approach involves filtering the instantaneous equations. LES explicitly computes the larger turbulent scales, while the smaller scales still require modeling [59, 60]. RANS is typically favored in industrial applications where numerous design iterations are necessary, as its computational cost is on the order of 10 to 1000 times lower than that of LES. As of the time of writing, commercial Computational Fluid Dynamics (CFD) codes predominantly use the RANS approach [60].

The first subsection covers solid-phase modeling. The second subsection examines flow modeling during venting, including the activation of different safety devices. The third subsection focuses on modeling the combustion of vented gases. Finally, the last subsection addresses the modeling of thermal runaway propagation.

2.2.1 Solid phase modeling

Despite the considerable difficulty of assembling a global cell model from sub-models of individual components, attempts can be found in the literature for heat and gas generation models within the condensed materials of the cell. These models consider the contributions of the different chemical reactions occurring in a cell undergoing thermal runaway, referred to as “thermal-abuse reactions”.

Heat generation

Heat generation is the starting point for TR. Current models only consider the major reactions between the components of the jellyroll. A 1-D mathematical model was developed by Hatchard et al. [61] based on the kinetics of the reactions between the electrodes and the electrolyte. It showed it is possible to predict the thermal behavior of an 18650 Li-ion cell based on the kinetics of the main reactions. Kim et al. [49] generalized this model in a three-dimensional, finite-volume Li-ion battery cell model. The exothermic reactions considered are the SEI decomposition, the anode-solvent reaction, the cathode-solvent reaction, and the electrolyte decomposition. This model enables the study of more complex cell geometries and illustrates the effect of non-isotropic properties in the jellyroll, due to the different layers

of materials as shown in Figure 2.1. Due to the cylindrical and layered nature of the jellyroll, the reactions propagate first in the axial and tangential directions (layer-parallel direction) before occurring in the radial direction (layer-normal direction).

A similar model was developed by Melcher et al. [62], and considers the same exothermic reactions with the constant fuel assumption (constant concentration of reactants). Additional heat contributions due to electrical sources such as Joule or Ohm heating are also considered. This model can compute the time it takes a cell to undergo thermal runaway under various heating conditions but cannot resolve the decay period due to the constant fuel assumption. Coman et al. [63] extended the existing model by incorporating a short-circuit mechanism to convert the energy stored in the cell into heat. This extension is also based on the Arrhenius formulation and is triggered at a specific threshold temperature. This approach was experimentally validated by the authors, but only for a specific 18650 NCA cell. However, because the trigger temperature can vary significantly between different cell chemistries, applying this model to other types of cells requires additional experimental tests to determine the appropriate reaction parameters.

Gas generation

Gas generation is strongly linked to heat generation. Knowing the quantity of gas inside the cell with respect to time is necessary to model accurately the venting mechanism. As shown in Section 2.1.4, the gas generation mechanisms are not well understood and are modeled with different degrees of complexity. The most commonly used approach is to assume that the rate of gas generation for a given reaction is proportional to the rate of heat generation by that reaction [64]. Consequently, the total gas mass flow can be calculated based on the thermal-abuse reaction rates as follows:

$$\dot{m}_{\text{gas}} = \sum_i \delta_i R_i \tag{2.1}$$

where for each reaction i, δ_i is the mass of gas generated per reaction and R_i the reaction rate. The number of reactions depends on the modeling approach. Kim et al. [52] used a one-step kinetic model that provides the degree of reaction progress. Ostanek et al. [56] used a common thermal abuse model with four reactions fitting the values of δ_i using experimental data. Other models used a more detailed approach with more reactions [31, 47, 57]. For all models, the gas mixture is considered to have a fixed composition taken from the work of Golubkov et al. [10, 36].

A second approach is to include the phase-changing phenomenon happening in the cell.

Indeed, the evaporation of liquid electrolytes plays a non-negligible role in both the heat generation of the cell (endothermic phase change) and the gas generation (evaporation) [50, 65]. This phenomenon is included in several models to better match experimental data. Coman et al. [50] developed a 0-D model including the venting of the electrolyte as an ideal gas flowing isentropically through an orifice when the pressure reaches a threshold. The authors published a second model implementing the evaporation of the electrolyte [51] but only until the first venting. To further understand the effect of electrolyte evaporation throughout the entire thermal runaway process, Ostanek et al. [31] developed a 0-D model that includes heat and gas generation by electrolyte evaporation and melting of the separator and current collector. This model was used to study the evaporation rate of the electrolyte. The authors demonstrated that rapid evaporation can delay or even suppress thermal runaway. This work was then implemented by the same authors into a 3D RANS model to study the vented gas flow field structure during the venting process. The electrolyte evaporation is split into three different periods with different sources of electrolyte vapor: the liquid-vapor equilibrium period, the constant drying rate period, and the decaying rate drying period. The effect of the electrolyte evaporation rate was not analyzed using the 3D model.

Finally, a third approach is to consider all solid or liquid ejecta from the cell. Experimental tests show the ejection of incandescent sparks and sometimes liquid electrolytes [47, 66]. Most violent runaways can include an entire section of the jellyroll or even the top part of the casing. Currently, the mechanisms behind these events are unknown and are not included in numerical models. One model accounted for the presence of solid ejecta in the energy balance [56]. The authors assumed a fixed amount of solid ejecta carried out of the cell with the vent gas and fitted the parameters linked to the phenomenon with experimental data. The impact of solid ejecta on the external flow field and propagation was studied by Zhang et al. [57] using a Discrete Phase Model (DPM) to add carbon particles.

2.2.2 Venting and safety devices modeling

The study of turbulent flow fields emerging from venting 18650 batteries is important for understanding the combustion and heat transfer phenomena associated with thermal runaway. Several numerical investigations have explored the non-reactive flow through venting holes [56, 67].

Li et al. [67] conducted a RANS simulation on various commercially available 18650 batteries. Each cell cap was scanned using computed tomography to extract a detailed CAD model. The Mach number and turbulent mixing distribution were calculated for an internal-to-ambient pressure ratio ranging from 1.2 to 8. The article identifies the locations of choke points, which

are determined by geometry and are not expected to change with variations in pressure ratio. The results highlight the emergence of these choke points at various positions within the caps. At a choke point, the mass flow rate becomes independent of the downstream pressure in the flow field; thus, for certain caps, increasing the surface of vented holes on the positive tab does not impact the flow rate since the choked flow occurs near the current collector [34]. This study shows that the different cap geometries led to various spatial distributions of the vented gas and can impact the heat transfer from the cell.

Building on this model, Ostanek et al. [56] incorporated the gas generation mechanism to further examine the turbulent flow structure. This RANS model focuses on the initial venting phase, demonstrating the formation of vortices that enhance mixing between the ambient air and the vented gases within the first microseconds after the vent opens. During this short period shown in Figure 2.6, the jet velocity can reach up to 500 m/s, primarily influenced by internal pressure. The velocity then drops to less than 1 m/s once the internal pressure is released within 100 μs. As the cell continues to heat, internal reactions accelerate significantly affecting the flow dynamics.

During the thermal runaway, the maximum jet velocity computed by the model increases to around 100 m/s due to the increased internal pressure caused by rapid gas generation. This leads to jets emerging from the cell with a shallower angle, thus enhancing the spatial distribution of combustible gases. Additionally, the venting flow is non-symmetric, attributed to the presence of the burst disk which partially blocks some venting holes. This broader distribution and asymmetry can have critical safety implications, as it can significantly impact simulations of heat transfer from the cell.

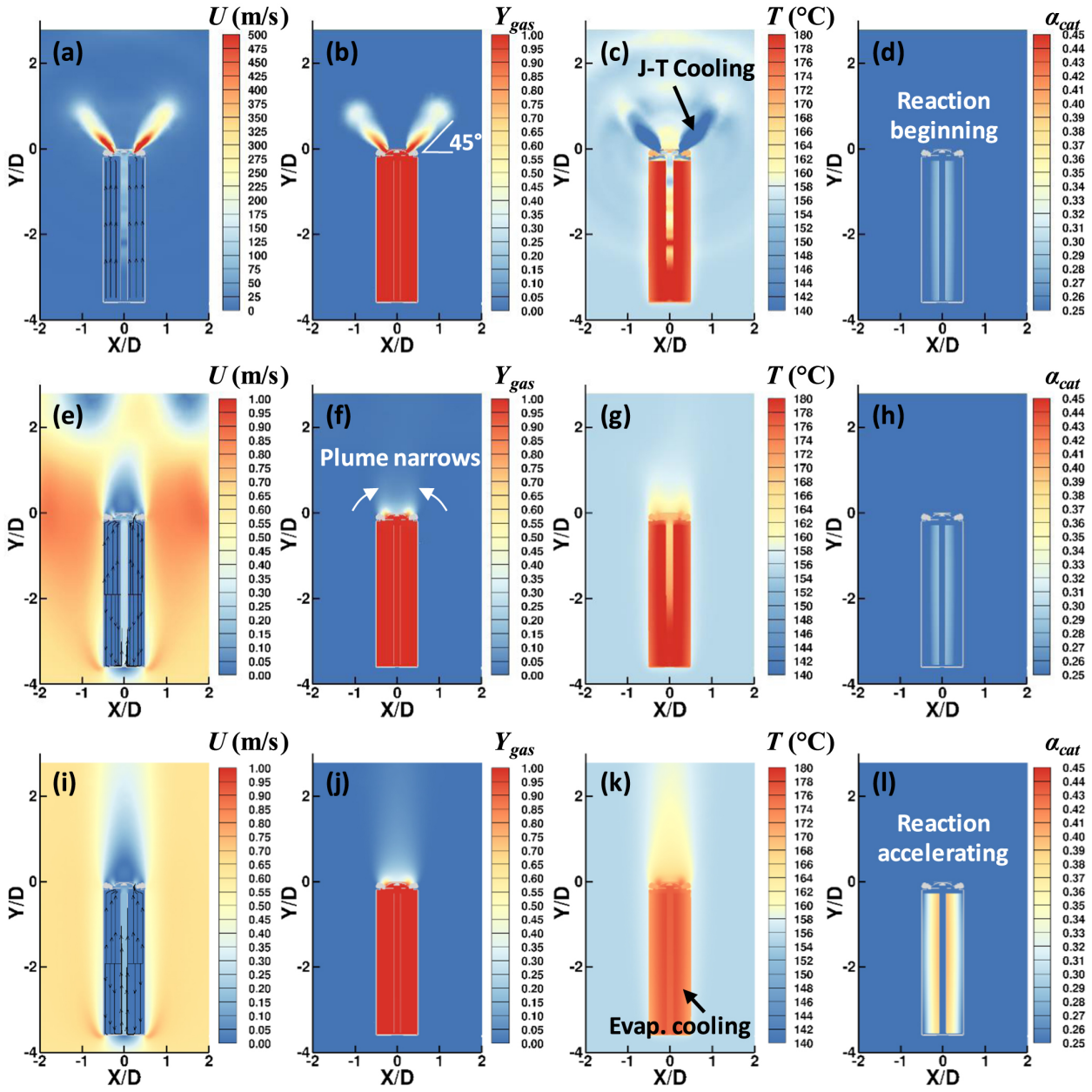

Figure 2.6 - XY cut view showing velocity magnitude contours (a,e,i), mass fraction of vented gases (b,f,j), temperature (c,g,k), and progress of cathode decomposition reaction (d,h,l) at three different times after the first venting: 129.59 μs after venting (a-d), 94.4 ms after venting (e-h), 124.4 s after venting (i-l) [56]. Licensed under CC BY 4.0

2.2.3 Gas combustion modeling

This section reviews the state of the art on the models for the combustion of the gases released during the thermal runaway. The models presented above solely considered phenomena occurring inside the cell and the venting of the gases. However, due to their high temperature and chemical reactivity, it is very likely as observed experimentally that a flame will spontaneously ignite or be triggered by hot and reacting solid ejecta. When stabilized close to the vent, such flame poses a significant risk of propagating the thermal runaway to neighboring cells. For that reason, numerical modeling of the combustion of the vented gases has been performed to quantify the heat released by this combustion.

Numerical combustion models

This subsection presents the main combustion models used in commercial CFD codes. Combustion can generally be categorized into two primary flame regimes [60]:

- Premixed flames: where the fuel and oxidizer are **mixed** before the combustion.
- Non-premixed flames: where the fuel and oxidizer are **not mixed** before the combustion.

The flames can also be classified based on the turbulence level (laminar vs. turbulent) but the flow of gases vented by the cell is usually highly turbulent [67] leading to this section mostly focusing on turbulent combustion.

As of this writing, very few models integrate combustion into the study of thermal runaway [47, 52, 54, 57], and only the work by Cellier et al. [55] focuses exclusively on combustion. However, since Cellier's model does not consider other mechanisms relevant to thermal runaway, it will be discussed later in the context of combustion mechanisms specifically.

All models, except for that of Cellier et al., typically use a commercial CFD code (Fluent) with the Reynolds-Averaged Navier Stokes (RANS) approach. In this approach, these unclosed non-linear terms include the Reynolds stresses, turbulent and Reynolds-averaged (RA) diffusive fluxes of species and enthalpy, as well as the RA species reaction rates, which are particularly important in turbulent combustion. The closure for species reaction rates is very complex and is typically derived from physical approaches that compare the chemical and turbulent timescales [60,68]. The most common approaches include geometrical analysis (the flame front is considered as a surface moving with the turbulent flow field), turbulent mixing (the chemical timescale is shorter than the turbulent timescale reducing combustion

to solely a mixing problem), and one-point statistics (combination of the reaction rates from Arrhenius law with joint probability density functions) [68]. From these key concepts, RANS combustion models have been developed and applied to battery fires. The most common (No-model, Eddy-Dissipation Concept, Non-premixed or partially premixed combustion with the flamelet approach) are briefly presented below. Their main assumptions are given in Table 2.5.

The first approach involves neglecting the effects of turbulence. Using the Arrhenius reaction rate, this finite-rate or "no-model" approach computes the reaction source term directly from the Reynolds-averaged species concentrations and temperature. However, this model is generally only applicable to laminar flames or in cases of extremely high turbulence intensity. In other situations, it can lead to errors reaching several orders of magnitude [60].

The Eddy-Dissipation model assumes that the reaction rate is solely controlled by turbulent mixing, as the fuel burns rapidly [69]. In this model, the reaction zone is composed of cold products and hot reactants mixed by turbulence. The Eddy-Dissipation model was extended into the Eddy-Dissipation Concept (EDC) model to incorporate detailed chemical mechanisms [70]. In this model, combustion is assumed to occur within small turbulent structures. Each computational cell is considered to contain a constant-pressure reactor occupying a fraction of its volume, where reactions are solved over a turbulence-dependent timescale removing the infinitely fast chemistry assumption. More recently the EDC model was generalized with the Partially Stirred Reactor model [71, 72].

The models discussed above utilize a Species Transport approach, in which each individual species is transported in the gas phase. However, for non-premixed combustion, the mixture fraction approach can be employed under several assumptions: constant thermodynamic pressure, equal and constant species heat capacities, Fick's law for molecular diffusion, and separated fuel and oxidizers stream [60]. This mixture fraction is computed based on the atomic mass fraction [73]:

$$f = \frac{Z_i - Z_{\mathrm{i,ox}}}{Z_{\mathrm{i,fuel}} - Z_{\mathrm{i,ox}}} \tag{2.2}$$

where Z_i is the elemental mass fraction for element i. Under the assumption of chemical equilibrium, the flow variables are directly related to the mixture fraction. However, this hypothesis is inadequate for most practical applications, and additional information on the flame structure is required to establish a unique relationship between the mixture fraction and thermochemical properties [60]. It can be achieved using the flamelet approach which considers the turbulent flame as an ensemble of thin, 1D laminar diffusion flames [74]. These flames can be parameterized by the mixture fraction and the scalar dissipation rate and give the local flame structures. To obtain the averaged flow variable, the model is closed

with an assumed-shape PDF approach [75]. Other non-premixed combustion models, such as the Conditional Momentum Closure model [76] and Unsteady Laminar Flamelets [77], are rarely utilized in the context of battery fires. This non-usage arises because these models are either not implemented in common commercial codes (Conditional Momentum Closure) or implemented but not usable in a transient setup (Unsteady Flamelets).

The premixed combustion approach is not typically employed in battery fires, as the cell primarily produces fuel rather than a fuel/oxidizer mixture [10, 36]. However, it may be relevant in studies addressing explosion hazards in confined spaces resulting from vented gas mixed with ambient oxidizer [78]. Nonetheless, some models combine the non-premixed and premixed approaches into a partially-premixed approach. In addition to the mixture fraction, a scalar variable representing the reaction progress is used and varies from 0 in fresh reactants to 1 in burnt products. As for non-premixed combustion, models based on chemical equilibrium and steady diffusion flamelets exist and assume the flame front is infinitely thin. For more accurate modeling, the Flamelet-Generated Manifold (FGM) model does not assume the infinite thickness of the flame front and can be used for extinction or ignition modeling [79]. This model remains parameterized by laminar flamelets but can use either diffusion flamelets or any configuration of premixed flamelets.

Table 2.5 - Main combustion models and their assumptions. Model names follow ANSYS Fluent nomenclature

Approach	Combustion model	Main assumptions
Species Transport	Finite-Rate (No model)	No turbulence OR infinitely fast turbulent mixing
	Eddy-Dissipation Concept	Chemistry solved in small perfectly-stirred reactors
Non-premixed combustion	Chemical Equilibrium	Infinitely fast chemistry
	Steady Diffusion Flamelets	Flamelet hypothesis Infinitely thin flame front
Partially premixed combustion	Chemical Equilibrium	Infinitely fast chemistry
	Steady Diffusion Flamelets	Flamelet hypothesis Infinitely thin flame front
	Flamelet Generated Manifold	Flamelet hypothesis

Application to battery flames

While various combustion models can be applied to battery flames, their use in the context of thermal runaway presents specific challenges. The geometry of the battery cell requires a 3D analysis of the combustion processes, which significantly increases simulation costs and necessitates additional modeling. Given the wide range of chemical mechanisms and combustion models, a thorough validation process is essential to select the most accurate model for each specific application.

To fully understand the effect of the venting on the combustion, all previous stages of the thermal runaway must be modeled, requiring the RANS approach to limit computational costs. Kim et al. [52] modeled the turbulent combustion of the vented gases using the Eddy-Dissipation/Finite-rate approach available in the species transport combustion model of Fluent. The chemical mechanism used is based on 5 reactions [80, 81] for the 6 species measured by Golubkov et al. [36] for an NCA cell, with the addition of O_2, N_2, and H_2O. Similarly, Zhang et al. [57] used the same combustion mechanism with five reactions and 6 species [80, 81] with the Eddy-Dissipation Concept Model, which is also part of the species transport approach. Finally, Zhao et al. [47] solved the gas combustion using a partially premixed combustion model assuming the vented gases are a mixture of fuel and oxygen generated by the cathode decomposition. No precise information on the combustion model is given.

For validation purposes, Kim et al. [52] compared their results with experimental data provided by Chen et al. [38], while Zhao et al. [47] and Zhang et al. [57] conducted in-house experiments. For the species transport approach, the flame appears for 5 to 6 seconds, which is two to three times shorter than observed in the experiment, where the flame lasted between 7 to 14 seconds with a maximum flame length of around 35 cm [38]. The model was run using different states of charge (SOCs): a flame appears for SOCs of 50% and 100% with varying maximum flame heights and durations. However, no flame is observed for a SOC of 25%. This indicates that the SOC of the battery plays a significant role in the amount of gas released and the heat generation rate. According to the authors, the heat produced by the gas-phase reactions dominates the total heat generated by the cell. This seems to correlate with experimental results [82]. However, the amount of heat generated is one order of magnitude higher than experimental values [30, 83]. For the partially premixed approach, the flame lasted 20 seconds with a predicted height lower than the flame obtained experimentally [47]. No conclusion can be drawn from this model as the authors do not provide any information on the combustion model (fuel composition, mass flow rate, heat release rate). Zhang et al. [57] compared cell temperature and thermal runaway timing with experimental

results; however, no comparison was made regarding the combustion process.

To maintain manageable computational costs of numerical simulation while including more chemical species and reactions, Cellier et al. [55] developed a reduced chemical mechanism. It is based on the San Diego Mechanism [84] (57 species and 268 reactions) and reduced to 24 species and 93 reactions using five cases chosen to represent a diversity of events found in battery fires. The authors then used the reduced mechanism to run a 3D LES simulation of vented gas combustion using the CFD solver AVBP. They used the vented gas composition and parameters from the NMC battery tested by Golubkov et al. [36]. Only the outside of the battery is modeled with the vented gases injected in the domain using a mass flow inlet with prescribed turbulence to model the flow through the cap. The ignition was induced using a sphere of hot gases to represent a forced ignition caused by sparks or ejected incandescent matter. Two configurations were studied: one with five venting holes and another with three. The five-hole geometry showed an attached flame with no residual flammable gases. In contrast, the three-hole geometry showed a flame extinguishing 20 ms after ignition and unburnt vented gases accumulating outside the cell. The overall amount of heat was higher with five holes. Thus, the geometry and number of the vent holes have a significant impact on the flame behavior, the amount of heat released can be reduced at the cost of having unburnt gas outside the cell that can ignite elsewhere. The new mechanism showed a reduction of computational time by a factor of 5 in comparison to the complete mechanism. However, the computational cost remain very high due to the use of LES.

2.2.4 Thermal runaway propagation

For most applications, cells are typically assembled in packs containing multiple units side-by-side. To match the energy of one liter of gasoline, approximately 50 liters of cells are needed leading to EVs containing thousands of cells. It is important to quantify the propagation risk and find design features to reduce its likelihood of occurrence. Many parameters are at play such as the number of cells, their layout, the shape and ventilation of the container, etc. As seen in the previous sections, modeling a single cell is challenging, and therefore, modeling a pack is even more complex as it requires the coupling of several cells. Only a few attempts are reported in the literature.

The configuration of batteries within a pack varies between manufacturers. Although numerous form factors exist, this section specifically addresses packs that utilize 18650 cells positioned side by side. The most studied configuration is a pack composed of 25 18650 cells, arranged in a 5x5 pattern as shown in Figure 2.7 [53, 54, 58]. The main propagation phenomena are the heat transferred by conduction, convection, and radiation from a cell

undergoing thermal runaway, the hot jet of gases impinging on another cell, the combustion of vented gases producing heat, and the heat transfer from the environment.

Mishra et al. [53,54] have studied the impact of vented gases on the thermal runaway propagation in a pack of 18650 cells with non-reactive and reactive flow models. The batteries are enclosed in a box initially filled with air and can self-heat through thermal abuse reactions. One cell is called the "trigger cell" and ejects hot gases for two seconds at the beginning of the simulation. The radiation is modeled using the Surface-to-Surface approach [85]. The non-reactive model aims to study the impact of the cell-to-cell gap (distance between two cells), the overhead gap (distance between the top of a cell and the upper surface of the box), and the vent placement as defined in Figure 2.7a) [53]. Key conclusions from this model are that an increased cell-to-cell and overhead gap reduces the risks of propagation. Furthermore, if the cell has a case failure and vents from its side, the neighboring cells have a higher risk of entering thermal runaway due to the direct impingement of the hot jet. Finally, an external opening on the battery pack such as ventilation can affect the propagation depending on its location relative to the trigger cell. In the reactive case, the combustion of the gases is modeled using the non-premixed approach [54]. The gas composition is taken from Golubkov et al. [36] for an LCO 18650 battery. The results from this model show an increased risk of propagation due to the additional heat generated by the combustion.

To quantify the contribution of each mechanism, Ostanek et al. [58] conducted several quasi-steady-state 3D simulations on the 25-cell pack. The cells are in a box with open walls but with a ceiling placed at 11.2 mm from the vent. The trigger cell vents hot gases at a mass flow rate of 2 g/s, with gas composition based on NCA cell experiments. The combustion is included with the Eddy-Dissipation model. Soot concentration is modeled with a one-step mechanism, affecting only the optical thickness of the fluid. Radiation effects are modeled using the Discrete Ordinates (DO) model. No solid-phase reactions are included. The different heat transfer mechanisms are isolated by altering the boundary conditions in the model. The simulations employ a detailed cap model [86] that generates three primary jets from the cell. According to Figure 2.7b), one jet is directed along the +Z axis, and two additional jets are directed along +X/+Y and -X/+Y. All jets impact the ceiling of the battery pack. As visible in Figure 2.7, the trigger cell is numbered 13 and is located in the middle of the pack. Cells Z1, Z2, -X1, X1, -Z1, and X1Z1 refer to cells 18, 23, 12, 14, 8, and 19, respectively. The results are shown in Figure 2.8, and indicate that the cells impinged by the hot jets (Z1 and Z2) received the highest heat flow. The heat radiating from the heated ceiling is estimated to be approximately 75 W and affects all neighboring cells uniformly. Finally, the cell's case radiates less than 15 W, impacting only directly adjacent cells. These values are computed by setting the investigated surface at 600°C. This approach can lead to an underestimation

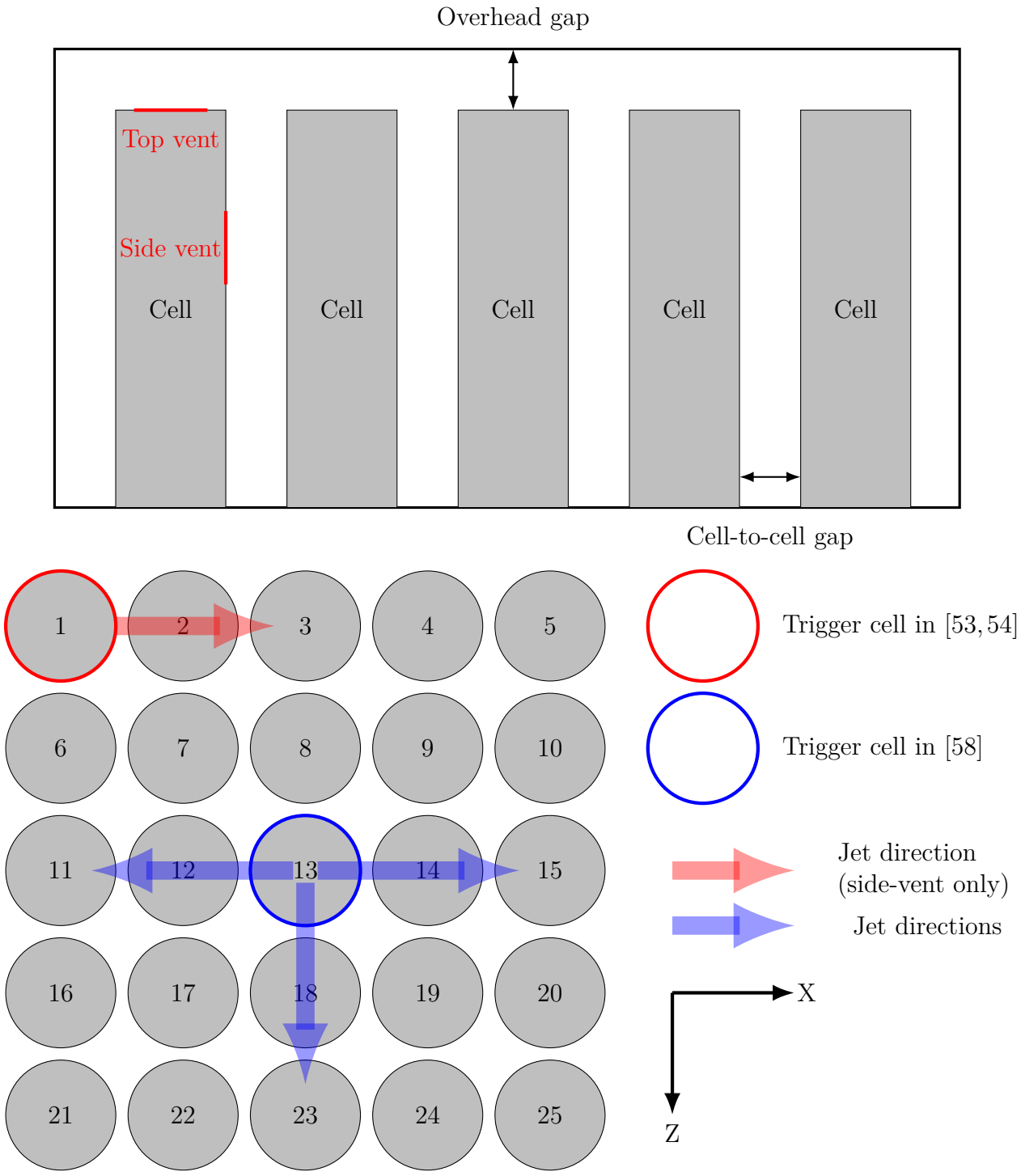

Figure 2.7 - Side view (top) and top view (bottom) of the 5x5 pack used in [53, 54, 58]

of the radiative heat load, as some surfaces may reach temperatures higher than 600°C. The heat emitted from soot and combustion is negligible (less than 1 W) compared to the other mechanisms. The total heat flow, ranging from 80 W to 135 W, is sufficient to trigger a thermal runaway. The three models presented here are yet to be validated with experimental results.

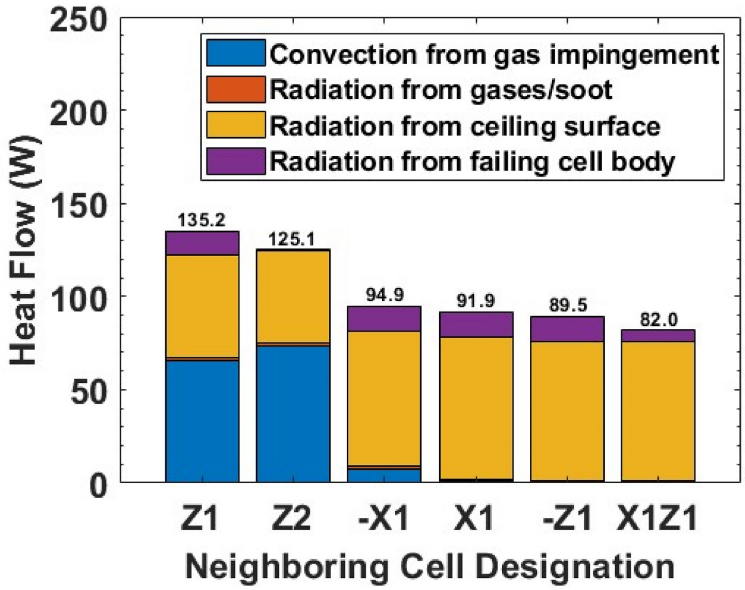

Figure 2.8 - Contribution from different propagation mechanisms on neighboring cells [58]. Licensed under CC BY 4.0

2.3 Literature gap and project objectives

The review shows that, despite significant progress, the complexity of thermal runaway in lithium-ion batteries still presents challenges. Indeed, the numerical modeling of thermal runaway is highly complex and requires accounting for each phenomenon and their coupling. Each part of a thermal runaway can be modeled with a varying level of detail (e.g., simplified 2D vs. complete 3D geometry) and each of these individual models needs to be coupled and adapted for the battery type investigated. Currently, the modeling of thermal runaway can be divided into four aspects: **heat and gas generation within the jellyroll**, **venting process**, **combustion of vented gas**, and **propagation inside a battery pack**.

For **heat and gas generation in the jellyroll**, the literature largely agrees on the modeling approach. Heat generation is typically modeled using a series of reactions described by Arrhenius-type equations. The number of these reactions varies depending on the current understanding of the specific materials involved in the thermal runaway sequence. Similarly,

the gas generation is modeled as proportional to the heat generation with the inclusion of the electrolyte vaporization. However, data on the gas composition is lacking due to the high number of parameters at play and the general complexity of measuring gases vented by a burning cell.

The modeling of the **venting process** remains simplified with the use of the ideal gas law and the equation for an isentropic flow through an orifice. More detailed studies involve simulating the flow through a detailed geometry of the battery top, which varies for each cell available on the market. Furthermore, only the burst disk is acknowledged as the most crucial safety feature.

Combustion remains the least studied phenomenon. Few studies on TR have included it, and they often omit to report combustion-related data relevant to fire safety (e.g., heat release rate, ignition, etc.). A wide variety of combustion models are available in commercial solvers (species transport with different approaches for the chemical reaction rates, composition PDF transport, non-premixed combustion, or partially premixed combustion) each with their strengths and weaknesses, which have yet to be verified/compared in the context of battery combustion.

Finally, since **propagation** depends on accurately modeling the other aspects, it is currently studied experimentally rather than numerically. As of today, a complete simulation of the TR combining chemical reactions in the solid phases, combustion reactions in the gas phase, and thermal/mass transfers between the two phases meeting the industry standards does not exist. Only one study included all these phenomena on a single 18650 cell [57].

In this context:

- The main objective of this project is to develop a 3D, multi-physics, fully coupled framework for TR in LIBs using a commercial CFD solver and integrating internal reactions (leading to heat and gas generation), venting, and combustion.

The different phenomena are included using published models either already implemented in Fluent (as of the 2024R1 release: heat generation, combustion, and radiation) or through manual implementation, such as gas generation. The model aims to study the thermal runaway of a specific 18650 NMC cell induced by overheating to compare its prediction with experimental data acquired in-house using calorimeters. The comparisons with experimental data focus on the temperature of the cell and the heat released during thermal runaway.

This study also aims to investigate various combustion models, given their significant impact on flame stabilization and, consequently, on TR propagation. A small-scale battery pack model is developed to demonstrate the framework's ability to simulate TR propagation across

multiple cells.

This leads to the following sub-objectives:

- Investigate different combustion models available in the commercial solver based on their capacity to capture ignition and heat release rate. The tested models include two from the Species Transport approach (No model and Eddy-Dissipation Concept), the non-premixed combustion approach with the Steady Diffusion Flamelets model, and the partially premixed combustion approach with the Flamelet Generated Manifold model.
- Combine models already implemented in the commercial solver to simulate the TR of an NMC 18650 cell and compare the results with experimental data.
- Simulate a battery pack containing two identical cells to confirm the model capabilities to simulate several cells simultaneously.

CHAPTER 3 METHODOLOGY

This chapter describes the various models that have been combined in the present work to simulate thermal runaway. The solver configuration and the boundary conditions applied are also detailed.

3.1 Reacting flow modeling

The section gives the governing equations solved in the numerical model. Due to the turbulent nature of the flow field induced by the cell and the requirement to maintain computational cost low, the RANS approach is used.

3.1.1 Reynolds-averaged governing equations

The RANS formulation is based on the Reynolds decomposition: any instantaneous quantity f is split into its mean component $\overline{f}$ and its fluctuating component f'. When the density is not constant (reacting and/or compressible flow), Favre-averaging is preferred. For an instantaneous quantity f, Favre averaging is defined as:

$$\tilde{f} = \frac{\overline{\rho f}}{\overline{\rho}} \tag{3.1}$$

Similarly to Reynolds averaging, the quantities are split into mean and fluctuating components, $\tilde{f}$ and f'' respectively. In this model, the Favre-Averaged formulation is used for all reacting flow governing equations. These include the standard mass conservation and the momentum conservation:

$$\frac{\partial \overline{\rho}}{\partial t} + \nabla \cdot (\overline{\rho}\tilde{\boldsymbol{u}}) = 0 \tag{3.2}$$

$$\frac{\partial \overline{\rho}\tilde{\boldsymbol{u}}}{\partial t} + \overline{\rho}\tilde{\boldsymbol{u}} \cdot \nabla \tilde{\boldsymbol{u}} = -\nabla \overline{p} + \nabla \cdot \overline{\boldsymbol{\tau}} - \nabla \cdot \widetilde{(\overline{\rho}\boldsymbol{u}''\boldsymbol{u}'')} - \overline{\rho}\boldsymbol{g} \tag{3.3}$$

where ρ is the mass density, $\boldsymbol{u}$ is the velocity vector, p the pressure, $\overline{\rho}\boldsymbol{g}$ is the gravitational body force and, $\boldsymbol{\tau}$ is the viscous stress tensor. The second and third terms on the RHS of Eq.(3.3) are unclosed and their closure is discussed in the next subsection. In fluid regions,

the Favre-averaged enthalpy equation is:

$$\frac{\partial}{\partial t}\left(\overline{\rho}\tilde{h}\right)+\nabla\cdot\left(\overline{\rho}\tilde{\boldsymbol{u}}\tilde{h}\right)=\nabla\cdot\overline{\lambda\nabla T}-\sum_{j}\nabla\cdot\overline{h_{\mathrm{j}}\boldsymbol{j_j}}+\overline{\tau:\nabla\boldsymbol{u}}+\frac{\overline{Dp}}{Dt}-\nabla\cdot\left(\overline{\rho}\widetilde{\boldsymbol{u}''h''}\right)+\overline{\rho}\tilde{\boldsymbol{u}}\cdot\boldsymbol{g} \quad (3.4)$$

All the terms on the right side are unclosed. Common closures are used such as the gradient-diffusion assumption for the enthalpy turbulent flux $\overline{\rho}\widetilde{\boldsymbol{u}''h''}$ and the laminar diffusive enthalpy fluxes $\overline{h_i\boldsymbol{j_i}}$. Furthermore, the viscous heating term is neglected. With all the closures, the following form of the Favre-averaged total energy equation is solved:

$$\frac{\partial}{\partial t}\left(\overline{\rho}\left(\tilde{e}+\frac{\tilde{\boldsymbol{u}}^2}{2}\right)\right)+\nabla\cdot\left(\overline{\rho}\tilde{\boldsymbol{u}}\left(\tilde{h}+\frac{\tilde{\boldsymbol{u}}^2}{2}\right)\right)=\nabla\cdot\left(\lambda_{\mathrm{eff}}\nabla\tilde{T}-\sum_{i}\tilde{h_{\mathrm{i}}}\overline{\boldsymbol{j_i}}\right)+\overline{\rho}\tilde{\boldsymbol{u}}\cdot\boldsymbol{g} \quad (3.5)$$

where, e is the internal energy, $\lambda_{\mathrm{eff}}=\overline{\lambda}+\lambda_t$ with λ and λ_t the laminar and turbulent thermal conductivity. $\boldsymbol{j_i}$ is the diffusion flux of species i.

The enthalpy is defined as:

$$h=\sum_{i}Y_ih_i \quad (3.6)$$

with:

$$h_i=\int_{T_{\mathrm{ref,i}}}^{T}c_{\mathrm{p,i}}dT+h_i^0(T_{\mathrm{ref,i}}) \quad (3.7)$$

where T is the temperature, Y_i is the mass fraction of species i, and $h_j^0(T_{\mathrm{ref,i}})$ is the formation enthalpy of species i at the reference temperature.

The Favre-averaged conservation equation for the species is:

$$\frac{\partial\overline{\rho}\tilde{Y_i}}{\partial t}+\nabla\cdot(\overline{\rho}\tilde{\boldsymbol{u}}\tilde{Y_i})=-\nabla\cdot\overline{\boldsymbol{j_i}}-\nabla\cdot\left(\overline{\rho}\widetilde{u''Y_i'}\right)+\overline{R_i} \quad (3.8)$$

where, for the species i, $\tilde{Y_i}$ is the mass fraction, $\boldsymbol{j_i}$ is the diffusion flux, and $\overline{R_i}$ is the chemical source term. The right-hand side terms are unclosed and require modeling: the closing of $-\nabla\cdot\overline{\boldsymbol{j_i}}-\nabla\cdot\left(\overline{\rho}\widetilde{u''Y_i'}\right)$ is detailed next subsection while $\overline{R_i}$ is closed using a combustion model.

The compressibility effects are accounted for through the computation of density with the Reynold-Averaged compressible form of the ideal gas law:

$$\overline{\rho}=\overline{\left(\frac{p}{\frac{\mathcal{R}}{M_W}T}\right)}\simeq\frac{\overline{p}}{\frac{\mathcal{R}}{\overline{M_W}}\tilde{T}} \quad (3.9)$$

where P is the local static pressure, $\mathcal{R}$ is the universal gas constant, and M_W is the molecular weight of the mixture.

3.1.2 Turbulence modeling

In this work, the **Realizable k-ε** turbulence model is used [87]. This two-equation model considers the eddy-viscosity μ_t as an isotropic scalar computed as a function of the Favre-averaged turbulent kinetic energy $\tilde{k}$ and Favre-averaged turbulence dissipation rate $\tilde{\varepsilon}$. For that purpose, two additional transport equations are solved for $\tilde{k}$ and $\tilde{\varepsilon}$:

$$\frac{\partial \overline{\rho}\tilde{k}}{\partial t} + \nabla \cdot \overline{\rho}\tilde{k}\tilde{\boldsymbol{u}} = \nabla \cdot \left[\left(\overline{\mu} + \frac{\mu_t}{\sigma_k}\right)\nabla\tilde{k}\right] + G_k + G_b - \overline{\rho}\tilde{\varepsilon} - Y_M \tag{3.10}$$

$$\frac{\partial \overline{\rho}\tilde{\varepsilon}}{\partial t} + \nabla \cdot \overline{\rho}\tilde{\varepsilon}\tilde{\boldsymbol{u}} = \nabla \cdot \left[\left(\tilde{u} + \frac{\mu_t}{\sigma_\varepsilon}\right)\nabla\tilde{\varepsilon}\right] + \overline{\rho}C_1 S\tilde{\varepsilon} - \overline{\rho}C_2\frac{\tilde{\varepsilon}^2}{\tilde{k} + \sqrt{\nu\tilde{\varepsilon}}} + C_{1\varepsilon}\frac{\varepsilon}{\tilde{k}}C_{3\tilde{\varepsilon}}G_b \tag{3.11}$$

with:

$$C_1 = \max\left[0.43, \frac{\eta}{\eta+5}\right];\ \eta = S\frac{\tilde{k}}{\tilde{\varepsilon}};\ S = \sqrt{2S_{ij}S_{ij}} \tag{3.12}$$

S_{ij} is the mean strain rate defined as $S_{ij} = \frac{1}{2}\left(\frac{\partial \tilde{u_j}}{\partial x_i}\frac{\partial \tilde{u_i}}{\partial x_j}\right)$, G_k is the generation of turbulence due to the mean velocity gradients computed as follows: $G_k = \mu_t S^2$. G_b is the generation of turbulence due to the buoyancy effects [88]. Y_M represents the compressibility effects modeled according to the work of Sakar and Lakshmanan [89]. σ_k is the Prandtl number for $\tilde{k}$. In Eq.(3.11), C_2 and $C_{1\varepsilon}$ are constants. σ_ε is the Prandtl number for $\tilde{\varepsilon}$.

Finally, the eddy viscosity is computed with:

$$\mu_t = \overline{\rho}C_\mu\frac{\tilde{k}^2}{\tilde{\varepsilon}} \tag{3.13}$$

The Realizable formulation of the k-ϵ model was developed to satisfy mathematical constraints on the Reynolds stresses. This "realizability" is ensured by making C_μ variable and computed based on the flow field. The computation of this variable and additional details are provided in Appendix A.

With the eddy-viscosity modeled, several terms in the governing can be closed. The viscous RA stress tensor $\overline{\boldsymbol{\tau}}$ in Eq. (3.3) is approximated as follows:

$$\overline{\boldsymbol{\tau}} = \overline{\mu}\left[\left(\nabla\tilde{\boldsymbol{u}} + (\nabla\tilde{\boldsymbol{u}})^T\right) - \frac{2}{3}\nabla\cdot\tilde{\boldsymbol{u}}\boldsymbol{I}\right], \tag{3.14}$$

where μ is the dynamic viscosity.

The Reynolds stresses tensor in Eq. (3.3) is closed using the Boussinesq hypothesis:

$$-\overline{\rho}\widetilde{\boldsymbol{u''u''}} = \mu_t\left(\nabla\tilde{\boldsymbol{u}} + (\nabla\tilde{\boldsymbol{u}})^T\right) - \frac{2}{3}(\nabla\cdot\tilde{\boldsymbol{u}})\boldsymbol{I} - \frac{2}{3}\overline{\rho}\tilde{k}\boldsymbol{I} \tag{3.15}$$

In the species conservation and energy conservation equations, the diffusion flux $\boldsymbol{j_i}$ of the species i can be modeled as:

$$\boldsymbol{j_i} = -\overline{\rho} D_{i,m} \nabla \tilde{Y}_i \tag{3.16}$$

where $D_{i,m}$ is the mass diffusion coefficient.

The turbulent flux of species mass fraction in Eq.(3.8) is modeled using gradient-diffusion approximations:

$$\overline{\rho}\widetilde{u''Y_i''} = -\frac{\mu_t}{Sc_t}\nabla \tilde{Y}_i \tag{3.17}$$

where Sc_t is the turbulent Schmidt number equal to 0.7.

3.1.3 Combustion modeling

Different combustion models are available in Fluent to close $\overline{R_i}$. Four of them are presented here, following the nomenclature from Ansys [90].

- Species Transport with Finite-Rate Kinetics, i.e., the no turbulence-chemistry interaction model (FR).
- Species Transport with the Eddy-Dissipation Concept (EDC).
- Non-Premixed Combustion with Steady Diffusion Flamelets (SDF).
- Partially Premixed Combustion with Flamelet Generated Manifold (FGM).

Each model is described in more detail in the following sections.

Species Transport

This subsection will cover the computation of the chemical source term using the species transport approach. The approach consists of solving the transport equation given in Section 3.1 for each species involved. Two models are presented with this approach: the Finite-Rate kinetics model and the Eddy-Dissipation Concept model.

With the **Finite-Rate model**, the chemical source terms are computed using reaction rate expressions **without accounting for the effect of turbulence**, i.e, $\overline{R_i(\boldsymbol{Y}, T)} = R_i(\widetilde{\mathbf{Y}}, \widetilde{T})$.

For the species i, the net source term is computed as:

$$R_i(\mathbf{Y}, T) = M_{w,i} \sum_{r=1}^{N_R} \hat{R}_{i,r}(\mathbf{Y}, T) \tag{3.18}$$

where $M_{w,i}$ is the molecular weight of the species i and $\hat{R}_{i,r}$ is the net molar rate of creation/destruction of the species i in the reaction r given by:

$$\hat{R}_{i,r} = \Gamma(\nu''_{i,r} - \nu'_{i,r})\Big(k_{f,r}\prod_{j=1}^{N}[C_j]^{\eta'_{j,r}} - k_{b,r}\prod_{j=1}^{N}[C_j]^{\eta''_{j,r}}\Big) \tag{3.19}$$

with N the number of chemical species, $[C_j]$ the molar concentration of species j. $\nu'_{i,r}$ and $\nu''_{i,r}$ are the forward and backward stoichiometric coefficients of reaction r, respectively, while $\eta'_{j,r}$ and $\eta''_{j,r}$ are the rate exponents for the reactant and the products respectively. $k_{f,r}$ and $k_{b,r}$ the forward and backward reaction rate constants for reaction r. The forward reaction rate is calculated using the Arrhenius equation as follows:

$$k_{f,r} = A_r T^{\beta_r} e^{-E_r/\mathcal{R}T} \tag{3.20}$$

where A is the pre-exponential factor, β is the temperature exponent, E is the activation energy and $\mathcal{R}$ is the universal gas constant. The backward rate is derived from the forward rate and the equilibrium constant K_r with the following relation: $k_{b,r} = k_{f,r}/K_r$. Finally, Γ represents the effect of third bodies on the reaction rate.

When using the **Eddy-Dissipation Concept** approach [70], the reactions are assumed to happen in small turbulent structures present in a portion of the computational cells called fine scales. The net rate of production for species in Eq.(3.8) is modeled as:

$$\overline{R_i} = \overline{\rho}\kappa\frac{Y_i^* - \widetilde{Y_i}}{\tau^*} \tag{3.21}$$

where Y_i^* is the fine-scale species mass fraction after the local Favre-Averaged chemical state ($\tilde{Y}$,$\tilde{T}$) is advanced in adiabatic, constant pressure reactor over the timescale τ^* and κ is the volume fraction of the fine scale. When using the Partially Stirred Reactor (PaSR) EDC model [71, 72], the volume fraction and time scale are modeled as:

$$\kappa = \frac{t_c}{t_c + t_{\text{mix}}} = \frac{1}{1 + D_a} \tag{3.22}$$

$$\tau^* = \min(\mathrm{t_c}, \mathrm{t_{mix}}) \tag{3.23}$$

where D_a is a Damköhler number defined as the ratio of the mixing time scale t_{mix} over the chemical time scale t_c, i.e, $D_a = t_{\text{mix}}/t_c$ The chemical time scale t_c is computed as:

$$t_c = \max\left(\frac{\overline{\rho}\tilde{Y}_i}{R_i(\tilde{Y}_i, \tilde{T})}\right) \tag{3.24}$$

where ω_i are the reaction rate of dominating slower species such as H_2, O_2, H_2O, CO_2 and CH_4. The mixing time scale t_{mix} is computed with:

$$t_{\text{mix}} = C_{\text{mix}} \frac{\tilde{k}}{\tilde{\varepsilon}} \tag{3.25}$$

where C_{mix} is a constant.

Reduced-Order Combustion

When using reduced-order models, the mixture fraction approach is utilized. This conserved scalar is computed in terms of atomic mass fraction:

$$f = \frac{Z_i - Z_{i,\text{ox}}}{Z_{i,\text{fuel}} - Z_{i,\text{ox}}} \tag{3.26}$$

where Z_i is the elemental mass fraction for element i.

Instead of solving the species transport equation, a Favre-averaged version is solved for the mixture fraction $\tilde{f}$:

$$\frac{\partial}{\partial t}(\overline{\rho}\tilde{f}) + \nabla \cdot (\overline{\rho}\tilde{\boldsymbol{u}}\tilde{f}) = \nabla \cdot \left(\left(\frac{\overline{\lambda}}{\overline{c_p}} + \frac{\mu_t}{\sigma_t} \right) \nabla \tilde{f} \right) \tag{3.27}$$

where c_p is the mixture-specific heat. Additionally, instead of the total energy, the enthalpy ($\tilde{h}$) form of the energy equation is solved:

$$\frac{\partial}{\partial t}(\overline{\rho}\tilde{h}) + \nabla \cdot (\overline{\rho}\tilde{\boldsymbol{v}}h) = \nabla \cdot \left(\frac{(\overline{\lambda} + \lambda_t)}{\overline{c_{\text{p}}}} \nabla \tilde{h} \right) \tag{3.28}$$

With the **Non-Premixed Combustion approach with steady diffusion flamelets** [74], the flame is seen as an ensemble of thin, steady, laminar, one-dimensional flames called diffusion flamelets parameterized by two scalars, the mixture fraction f and the scalar dissipation χ. A series of laminar counterflow diffusion flames is solved across a range of scalar dissipation. The calculations are done only once and all the properties such as temperature, density, or species mass fraction are stored in lookup tables. However, the instantaneous thermochemical scalars must be incorporated into the turbulent flame. Therefore, the flamelet model is closed using a joint probability density function (PDF) approach to address turbulence effects. In the case of a non-adiabatic system, the scalars are computed as:

$$\tilde{\varphi} = \iint \varphi(f, \chi_{st}, \tilde{H}) P(f, \chi_{st}) df dc \tag{3.29}$$

f and χ are assumed to be independent meaning the joint PDF can be computed as the

product of two PDFs: $p_f(f)$ and $p_\chi(\chi_{st})$. The shapes of these PDFs are assumed. p_f is a β-function PDF computed using $\tilde{f}$ and the Favre-averaged mixture fraction variance $\widetilde{f''^2}$ transported using the following conservation equation:

$$\frac{\partial}{\partial t}(\overline{\rho}\widetilde{f''^2}) + \nabla \cdot (\overline{\rho}\tilde{\boldsymbol{u}}\widetilde{f''^2}) = \nabla \cdot \left(\left(\frac{\overline{\lambda}}{\overline{c_p}} + \frac{\mu_t}{\sigma_t}\right)\nabla\widetilde{f''^2}\right) + C_g\mu_t \cdot (\nabla\tilde{f})^2 - C_d\overline{\rho}\frac{\tilde{\varepsilon}}{\tilde{k}}\widetilde{f''^2} \tag{3.30}$$

where C_g and C_d are constants with a value of 2.86 and 2.0.

For p_χ, fluctuations of χ_{st} are ignored, and the PDF is assumed to have the shape of a delta function: $p_\chi = \delta(\chi - \tilde{\chi_{st}})$ with the mean scalar dissipation is modeled as follows:

$$\tilde{\chi_{st}} = C_\chi \frac{\tilde{\varepsilon}}{\tau}\widetilde{f''^2} \tag{3.31}$$

where C_χ is a constant with a value of 2.0 and τ is the turbulent timescale computed as $\tau = \frac{\tilde{k}}{\tilde{\varepsilon}}$.

The partially premixed approach is a combination of the non-premixed and premixed approaches. It utilizes the mixture fraction approach but also requires the Favre-averaged progress variable $\tilde{c}$, defined as the normalized sum of the product species mass fractions:

$$c = \frac{\sum_k \alpha_k \left(Y_k - Y_k^u\right)}{\sum_k \alpha_k \left(Y_k^{eq} - Y_k^u\right)} = \frac{Y_c}{Y_c^{eq}} \tag{3.32}$$

where the superscripts u and eq denote the unburnt reactants and the chemical equilibrium respectively. α_k are constants chosen to have c increasing monotonously in the flame front from $\tilde{c} = 0$ where the mixture is unburnt to $c = 1$ where it is burned. Furthermore, to avoid additional terms related to the mixture fraction [91], the un-normalized version is transported using the following equation:

$$\frac{\partial\overline{\rho}\widetilde{Y_c}}{\partial t} + \nabla \cdot (\overline{\rho}\tilde{\boldsymbol{u}}\widetilde{Y_c}) = \nabla \cdot \left(\left(\frac{\overline{\lambda}}{\overline{c_p}} + \frac{\mu_t}{Sc_t}\right)\nabla\widetilde{Y_c}\right) + \overline{S_{Y_c}} \tag{3.33}$$

where the mean source term $\overline{S_{Y_c}}$ is modeled using a flamelet library.

With the **Partially-Premixed Flamelet Generated Manifold** model, thermochemical properties are parameterized by mixture fraction and reaction progress [79]. Similarly to the steady diffusion flamelets, the flame is defined as an ensemble of one-dimensional flamelets. These are calculated using laminar counter-flow diffusion flames over a range of scalar dissipation rates until extinction and then converted to the reaction progress space. The FGM model is also closed using a joined assumed-shape PDF approach to include turbulence. In

the case of a non-adiabatic system, the scalars (including $\overline{S_{Y_c}}$) are computed as:

$$\tilde{\varphi} = \iint \varphi(f, c, \tilde{H}) \tilde{P}(f, c) df dc \tag{3.34}$$

Similarly to the non-premixed approach, the un-normalized mean reaction progress variance is required to compute the PDF. It is transported using the following equation:

$$\frac{\partial \overline{\rho} \widetilde{Y_c''^2}}{\partial t} + \nabla \cdot (\overline{\rho} \tilde{\boldsymbol{u}} \widetilde{Y_c''^2}) = \nabla \cdot \left(\left(\frac{\overline{\lambda}}{\overline{c_p}} + \frac{\mu_t}{Sc_t} \right) \nabla \widetilde{Y_c''^2} \right) + C_\varphi \frac{\mu_t}{Sc_t} |\nabla \widetilde{Y_c''^2}|^2 - \frac{\tilde{\rho} C_\varphi}{\tau_{\text{turb}}} \widetilde{Y_c''^2} \tag{3.35}$$

where C_φ is a constant with a value of 2.0. The results of Eqs.(3.34) and (3.29) are computed once and stored in look-up tables.

3.2 Condensed-state reaction modeling

All phenomena occurring in the solid zones are modeled as described in this section.

In solid regions, the energy equation remains (sensible enthalpy form):

$$\frac{\partial}{\partial t} (\rho h_s) = \nabla \cdot (\lambda \nabla T) + S_{\text{solid}} \tag{3.36}$$

where h_s is the sensible enthalpy, λ is the thermal conductivity of the solid material, and S_{solid} is a volumetric energy source term.

The radiation is accounted for using the Surface-to-Surface model (S2S) [85]. The model ignores all absorption, emission, or scattering of the radiation from the gas phase leaving only the "surface-to-surface" radiation. This approach is preferred to other models as the radiation from the burning combustion is negligible compared to the other sources of radiation [58].

All surfaces are assumed to be opaque, diffuse, and gray with their emissivity and absorptivity independent from the wavelength. The reflectivity is computed using the conservation of energy and Kirchoff's law. The energy flux leaving a surface k is computed as:

$$q_{\text{out,k}} = \varepsilon_k \sigma T_k^4 + \rho_k q_{\text{in,k}} \tag{3.37}$$

where ε_k is the emissivity, σ is the Stefan-Boltzmann constant, and $q_{\text{in,k}}$ is the energy flux incident on the surface from other surfaces computed as:

$$q_{\text{in,k}} = \sum_{j=1}^{N} F_{kj} q_{\text{out,j}} \tag{3.38}$$

The amount of incident energy depends on the view factor between each surface. The view factor F_{ij} between the surface i and j is computed as follows:

$$F_{\mathrm{ij}} = \frac{1}{A_i} \int_{A_i} \int_{A_j} \frac{cos\theta_i cos\theta_j}{\pi r^2} \delta_{ij} dA_i dA_j \tag{3.39}$$

where δ_{ij} is equal to 1 if the surface j is visible from the surface i and 0 otherwise.

3.2.1 Heat generation

The heat generated inside the cell is computed using a thermal abuse model developed by Kim et al. [49]. In this approach, four exothermic condensed-state reactions are considered and correspond to the decomposition of each main active component of the battery. These reactions referred to as "thermal abuse reactions" are the decomposition of the solid electrolyte interface (sei):

$$R_{\mathrm{sei}} = -\frac{dc_{\mathrm{sei}}}{dt} = A_{\mathrm{sei}} \exp\left(\frac{-E_{\mathrm{sei}}}{\mathcal{R}T}\right) c_{\mathrm{sei}}^{m_{\mathrm{sei}}}, \tag{3.40}$$

the anode-solvent reaction (ne) and SEI growth (e_{sei}):

$$R_{\mathrm{ne}} = -\frac{dc_{\mathrm{ne}}}{dt} = A_{\mathrm{ne}} \exp\left(-\frac{e_{\mathrm{sei}}}{e_{\mathrm{sei,ref}}}\right) \exp\left(\frac{-E_{\mathrm{ne}}}{\mathcal{R}T}\right) c_{\mathrm{ne}}^{m_{\mathrm{ne}}}, \tag{3.41}$$

$$\frac{de_{\mathrm{sei}}}{dt} = -R_{\mathrm{ne}}, \tag{3.42}$$

the cathode-solvent reaction (α):

$$R_{\alpha} = \frac{d\alpha}{dt} = A_{\alpha} \exp\left(\frac{-E_{\alpha}}{\mathcal{R}T}\right) \alpha^{m_{\alpha,1}} (1-\alpha)^{m_{\alpha,2}}, \tag{3.43}$$

and the decomposition of the electrolyte (elec):

$$R_{\mathrm{elec}} = -\frac{dc_{\mathrm{elec}}}{dt} = A_{\mathrm{elec}} \exp\left(\frac{-E_{\mathrm{elec}}}{\mathcal{R}T}\right) c_{\mathrm{elec}}^{m_{\mathrm{elec}}}, \tag{3.44}$$

where c_{sei}, e_{sei}, $e_{\mathrm{sei,ref}}$, c_{ne}, α, and c_{elec} are dimensionless parameters representing, respectively, the amount of metastable species containing lithium in the SEI, the thickness of the SEI layer and its reference value, the amount of lithium intercalated within the carbon at the anode, the degree of conversion at the cathode, and the concentration of electrolyte [92]. Furthermore for each reaction, R [1/s] represents the reaction rate, A [1/s] is the frequency factor, E [J/mol] is the activation energy, $\mathcal{R}$ [J/mol/K] is the universal gas constant, and m [-] is the

order of reaction. The total heat source term due to thermal abuse reactions is computed as:

$$S_{\text{solid}} = H_{\text{sei}} W_{\text{sei}} R_{\text{sei}} + H_{\text{ne}} W_{\text{ne}} R_{\text{ne}} + H_{\alpha} W_{\alpha} R_{\alpha} + H_{\text{elec}} W_{\text{elec}} R_{\text{elec}} \tag{3.45}$$

where W [kg/m^3] is the density of reactants and H [J/kg] is the heat of reaction. Constant values for A, E, m, H, and W, as well as the initial conditions for the parameters, are given in Table 3.1.

Table 3.1 Parameters for heat and gas generation models

Reaction	Parameter	Value	Unit	Ref.
SEI Decomposition	A	1.667e15	1/s	[92]
	E	1.3505e5	J/mol	[92]
	W	2.57e5	g/m^3	[92]
	H	610.4e3	J/g	[92]
	m_0	1	-	[49]
	δ	0.08	g	Fitted
Negative-Solvent Reaction	A	2.5e13	1/s	[92]
	E	1.3505e5	J/mol	[92]
	W	1.714e6	g/m^3	[92]
	H	610.4e3	J/g	[92]
	m_0	1	-	[49]
	δ	0	g	[56]
Positive-Solvent Reaction	A	2.25e14	1/s	[92]
	E	1.475e5	J/mol	Fitted
	W	7.9e5	g/m^3	[92]
	H	1.293e3	J/g	[92]
	m_0	1	-	[49]
	m_1	1	-	[49]
	δ	0.96	g	Fitted
Electrolyte Decomposition	A	5.14e25	1/s	[92]
	E	2.74e5	J/mol	[92]
	W	1.55e5	g/m^3	[92]
	H	406.9e3	J/g	[92]
	m_0	1	-	[49]
	δ	5.5	g	[56]

3.2.2 Gas Generation

The gas generation model is based on the work of Ostanek et al. [56], where each reaction generates a defined amount of gas:

$$\dot{m}_{\text{gas}} = \delta m_{\text{sei}} R_{\text{sei}} + \delta m_{\text{ne}} R_{\text{ne}} + \delta m_{\alpha} R_{\alpha} + \delta m_{\text{elec}} R_{\text{elec}} \tag{3.46}$$

with R [1/s] the reaction rate computed with Eqs.(3.40-3.44) and δm [g] the mass generated per reaction. The value of δ for each reaction is given in Table 3.1.

3.3 Model implementation

This section details the parameters used for each model and their specific implementation where required.

3.3.1 Solver

The sets of equations presented in Sections 3.1 and 3.2 are solved in a coupled manner with the commercially available software, ANSYS Fluent® Release 2024R1 [90]. Fluent uses the finite-volume method with cell-centered formulation to solve partial differential equations. The geometry is discretized into a series of polyhedral cells where the flow variables are computed at the cell centroid.

The pressure-based solver is used as it can operate across a wide range of flows and supports all combustion models. The flow is solved using a coupled algorithm for enhanced stability and accuracy, though at a higher memory cost [90]. An implicit second-order time integration scheme is used for the transient formulation to improve accuracy while default settings are kept for spatial discretization: second-order for the pressure, density, momentum, energy, and the mean mixture fraction; first-order for the turbulent kinetic energy and dissipation rate. Other parameters, such as under-relaxation factors or operating conditions, are kept at their default settings.

3.3.2 Configuration and setup parameters

The geometry in which thermal runaway is simulated consists of a cylinder (0.152 m in diameter and 0.9 m in height) in which a flow of air is circulated from bottom to top, around the cell as shown in Figure 3.2a. The geometry is chosen to reproduce the sensible enthalpy section of the experimental setup shown in Figure 3.1. This open-configuration calorimeter,

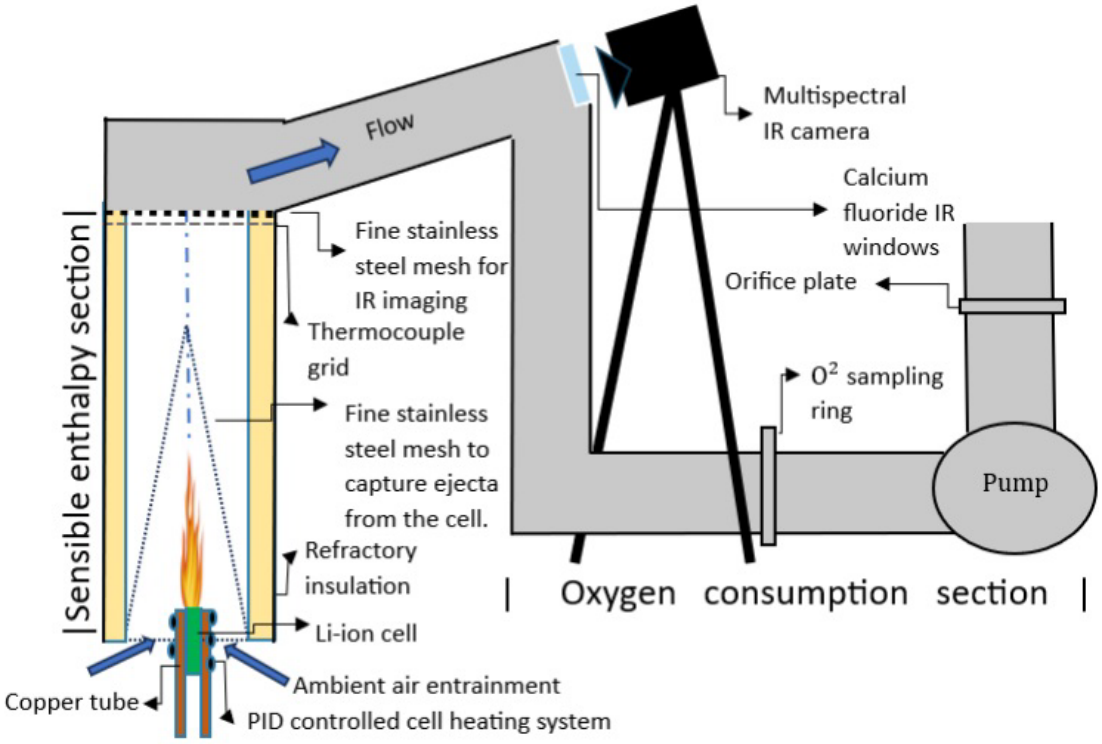

Figure 3.1 - SEOCC schematic representation. Reproduced from [95]

named SEOCC (Sensible Enthalpy and Oxygen Consumption Calorimeter), was designed and assembled to measure in real time the change in sensible enthalpy and the combustion heat release rate using the oxygen consumption method. This method is based on the principle that a constant amount of energy is released per unit mass of O_2 consumed with averaged value for hydrocarbons of 13.1 MJ per kilogram of O_2 [93,94]. This system relies on modifying a conventional cone calorimeter, tailored to accommodate a cell holder within a refractory insulation tube. Another student developed and operated the SEOCC in the laboratory.

The simplified cell cap geometry considered is based on the INR 18650-25R manufactured by Samsung SDI, with three vent holes as shown in Figure 3.3b. The cell is composed of a solid cylindrical jellyroll contained in a thin solid steel case and placed inside a copper tube. A steel support piece is placed under it. A cut view of the mesh is shown in Figure 3.2b, with a zoomed view of the bottom half in Figure 3.2c. The model counts 1,119,000 polyhedron cells with a minimal orthogonality of 0.15. The growth rate in each cell zone is set at 1.2. A boundary layer consisting of 5 layers is added on each wall, with a transition ratio of 0.272. The refined section visible in 3.2c is added using a body of influence with a maximum face size of 2 mm.

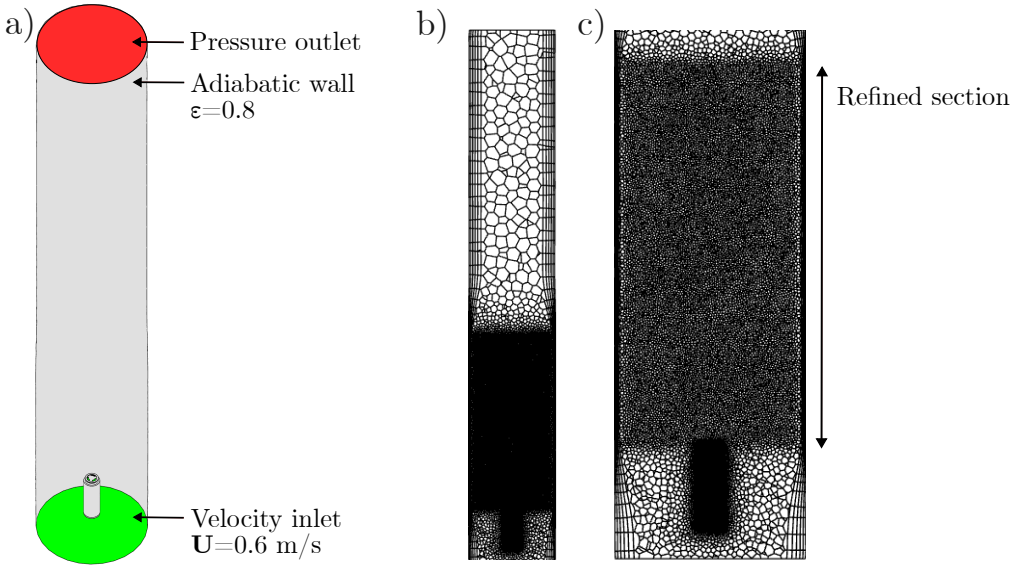

Figure 3.2 a) Isometric view of the model, b) XY cut view of the mesh, and c) XY cut view of the bottom half of the mesh containing the cell

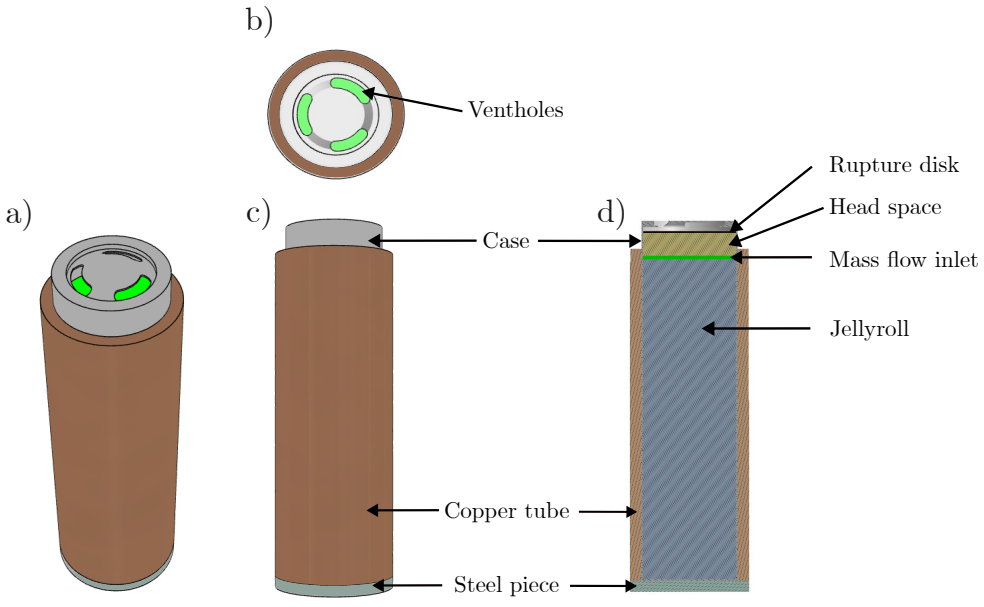

Figure 3.3 a) Isometric view b) Top view c) Side view and d) Cut view of the cell

3.3.3 Model parameters and boundary conditions

Except for the gas generation model, all phenomena are implemented using pre-existing models in Fluent. The parameters and the boundary conditions associated with each model are detailed below.

Heat generation model

Heat generation is modeled using the battery module with the conjugated heat transfer coupling model, and the jellyroll is designated as the active zone. No passive zones are selected. The thermal abuse model employs the 4-equation approach described in Section 3.2.1 with the values given in Table 3.1.

Gas generation model

For the gas generation model, the amount of gas generated by each reaction given in Table 3.1 corresponds to the theoretical total amount of gas that can be released by each reaction if it is fully completed. The actual amount depends on the initial values of the dimensionless parameter c. The effective amount is calculated as:

$$m_{\text{gas,generated}} = \frac{\delta}{\Delta c} \tag{3.47}$$

where Δc is the parameter range for each reaction. Table 3.2 gives for each reaction the theoretical amount, the range of the parameter c based on the initial value, and the effective amount of gas generated.

Table 3.2 Effective amount of gas generated

Reaction	δ [g]	Δc	$m_{\text{gas,generated}}[g]$	Ref.
SEI Decomposition	0.080	0.15	0.012	Fitted
Negative-Solvent Reaction	0	0.75	0	[56]
Positive-Solvent Reaction	0.1	0.96	0.096	Fitted
Electrolyte Decomposition	5.5	1	5.5	Fitted
Total			5.608	

The total amount of generated gas is taken from the work of Golubkov et al. [36] and the distribution between the reactions follows the approach proposed by Ostanek et al. [56]. The values of δ are fitted to trigger the venting around 150°C-170°C and generated a total of

5.6 g of gas. This model is implemented using Fluent Expressions, with one expression per reaction. Each expression computes the reaction rate of the respective reaction, as Fluent does not explicitly provide it before multiplying it by the specified amount of generated gas. The reaction rate for reaction i is calculated by dividing the heat generation rate of that reaction in each cell by its specific heat release and then averaging this value across the jellyroll.

Material properties

The default values from the database provided by Fluent are utilized for the material properties, except for the jellyroll where they are specified in Table 3.3. During thermal runaway, a cell loses several grams of mass. To account for this phenomenon, the density of the jellyroll is adjusted based on the progress of the electrolyte decomposition reaction:

$$\rho_{jr} = \rho_{jr,0}(1 - xc_{elec}) \tag{3.48}$$

where $\rho_{jr,0}$ is the initial density value and x is the fraction of jellyroll consumed based on the amount of gas generated. Since electrolyte decomposition accounts for 99% of the gas generation, the jellyroll density depends solely on this reaction. The chosen value for the fraction of jellyroll consumed is fitted to represent a loss of mass of 5.6 g. The varying density is implemented using a User-Defined Function compiled in Fluent.

Table 3.3 - Material properties of the jellyroll

Parameter	Value	Ref.
Density [kg/m^3]	[2720-2380]	[52] and Fitted
Heat Capacity [J/kg.K]	1100	[52]
Thermal Conductivity [W/m.K]	0.8	[52]
Share of jellyroll consumed [-]	0.125	Fitted

Safety measures

The gas generated, computed in Eq.(3.46), accumulates in the cell head-space, defined with a volume equal to 7% of the cell volume [50]. When the internal pressure of the head-space reaches a defined threshold of 16 MPa [67], the burst disk is removed, letting the gas flow through the vents. The venting is implemented using a script written with the Scheme programming language [96].

Combustion model

For combustion modeling, the mechanism used was developed by Cellier et al. [55] and consists of 24 species and 93 reactions. The fuel composition considered (H_2: 30.8%; CO_2: 41.2%; CO: 13.0%; CH_4: 6.8%; C_2H_4: 8.2%) is taken from Golubkov et al. [36] for a NMC cell. The fuel is added to the domain using a mass flow inlet at the top of the jellyroll as shown in Fig. 3.3.

The specific configuration of each combustion model is detailed below:

- For the Species Transport models, the Stiff Chemistry Solver is selected, and the fuel composition is specified at the mass flow inlet. The co-flow and backflow are considered to be only standard air.
- For the Non-Premixed Model with Steady Diffusion Flamelets, diffusion flamelets are generated and used to construct the PDF table. Standard air composition and fuel composition cited above are used. The mixture fraction is fixed at 1 at the gas inlet and 0 for the co-flow and backflow.
- The Partially Premixed Model with Flamelet Generated Manifold uses the same approach as the Non-Premixed Combustion model. The base progress variable computed by Fluent and defined in Section 3.1.3 is used [90]. The progress variable is set at 0 at all inlets.

Radiation model

The emissivity of all the exterior surfaces is set to 0.8 [58]. The view factors are computed before the simulation and stored in a separate file. Two sets of view factors are needed: one with the rupture disk set as the wall and a second with the rupture disk set as an interior.

Boundary Conditions

The air co-flow is added using a velocity inlet at the bottom of the domain and set at a velocity of 0.6 m/s to match the experimental setup. The walls of the domain are adiabatic. The gas exits the domain through a pressure outlet set at atmospheric pressure where air backflows at 300 K are allowed. An energy source term is applied to the copper tube to trigger the thermal runaway via overheating. The heat source is applied to follow a heating ramp of 10°C/min chosen to match experimental data, obtained following DO 311-A test procedure by RTCA [97] and computed with an Expression.

3.3.4 Simulation procedure

At the start of the simulation, the solid regions of the cell are set to 50°C to match the heating ramp used experimentally and the top disk is defined as a wall. The exterior fluid region is filled with air at standard composition (21% O_2 and 79% N_2 by volume) with an initial temperature and Y-velocity of 26.85°C and 0.6 m/s respectively.

Several strategies are used to reduce computational costs during the simulation. The timestep size is adjusted throughout the simulation. A large timestep size of 5 seconds is used during the heating phase. It is reduced to 1 μs during the venting process until the internal pressure returns to below 0.25 MPa where the timestep size can be increased without convergence issues. It is finally set to 2 ms for the combustion process and increased to 1 s at the end of all solid and gas phase reactions for the cooling phase. Timestep size management is handled using a script executed at each timestep. Other strategies include solving for the radiation only once every two timesteps.

The model was designed to run without interruption. However, due to changes in boundary conditions during venting, the simulation stops automatically, requiring Fluent to recompute the view factors. After reading the second set of view factors, the simulation can then continue.

3.3.5 Computational costs

This section gives the computational costs of the different combustion models and the costs of the thermal runaway complete simulation.

The computational costs for each combustion model are linked to the number of additional transport equations required by each combustion model: in this study, 24 for both FR and EDC, 4 for FGM, and only 2 for SDF. The computational time for 100 timesteps is provided in Figure 3.4. Additionally, the number of transport equations for the FR and EDC models increases with the number of species in the combustion mechanism. In contrast, for reduced-order approaches, the number of transport equations remains independent of the combustion mechanism. While using a more detailed mechanism can increase costs for generating and storing lookup tables, these additional costs are negligible compared to the overall simulation costs.

The complete thermal simulation with the SDF combustion model runs for up to 250 hours on 16 cores using the default parallelization parameters of Fluent.

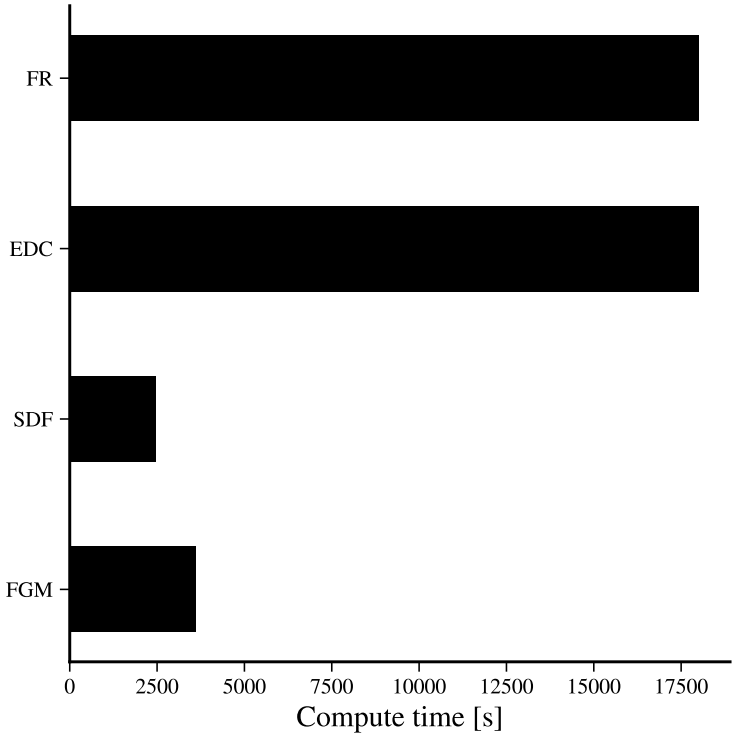

Figure 3.4 - Compute time required for 100 iterations of 16 cores

3.3.6 Critical discussion of the model implementation

The use of the RANS approach in the fluid leads to relying only on mean quantities and requires additional models but heavily reduces the computational costs. This approach is very coarse for turbulent combustion modeling, as the turbulence-chemistry interaction needs to be fully modeled, as opposed to being resolved. However, the LES alternative is not viable for the targeted design application. Some phenomena are greatly simplified: the thermal abuse is reduced to four reactions and the gas generation model uses a composition supposed constant and releases only gas. In reality, the gas composition evolves throughout the thermal runaway, and liquid and solid ejecta are also present. The radiation from the burning gases is also not included, but expected to be negligible [58] as discussed in Chapter 2.

For the geometry, simplifications were made compared to the experimental setup: the external insulation and heating wire were excluded. Additionally, the coflow is introduced via a velocity inlet that pushes air into the domain, whereas in the experimental setup, the coflow is generated by pumping air out at the outlet. For the cell geometry, the top part is also largely simplified with only the vent holes included. This approach provides a more accurate geometry compared to other numerical models [52, 57] without requiring costly in-depth

analysis of the top either through CT-scans [56] or opening the cell [34]. Finally, due to the commercial nature of ANSYS Fluent, technical difficulties can arise from the restriction in the usage of some models and access to specific quantities and equations compared to open-source solvers.

3.4 Methodology overview

This section summarizes the methodology used and provides an overview of the inputs and outputs of the model.

Figure 3.5 presents a flow chart of the model, which consists of two distinct zones: a solid zone (including the battery jellyroll, battery case, copper tube, and steel support) and a fluid zone (representing the surrounding environment). In the solid zone, heat and gas generation models are applied, with the maximum jellyroll temperature and gas mass flow rate determined and used as inputs at the mass-flow inlet. In the fluid zone, the turbulence model, the selected turbulent combustion model, and the venting submodel are solved.

The two zones are coupled, primarily exchanging heat through conduction, convection, and radiation. Mass transfer occurs via the gas generation model and the varying density of the jellyroll. Heat coupling between the solid and fluid zones is managed by Fluent, while mass coupling is manually implemented using the mass-flow inlet. The inlet receives its inputs (mass flow rate and temperature) from the solid zone: the mass flow rate ($\dot{m}_{\text{gas}}$) is calculated using the gas generation model, while the temperature is set to the maximum temperature reached in the jellyroll ($T_{\text{max,jellyroll}}$).

Table 3.4 lists the main input parameters employed in the various sub-models, specifying whether the parameter is fitted or sourced from the literature. For parameters not explicitly stated, the default values from Fluent are used. The fitting process for different parameters is described in their respective sections, except for the activation energy E of the Positive-Solvent reaction, which is detailed in Appendix B.

The model outputs include all the standard CFD quantities provided by Fluent, such as temperature, velocity, and pressure, along with model-specific quantities like the progression of thermal abuse reactions (Eqs.(3.40)-(3.44)). For comparison with experimental data, the key quantities of interest are the temperature of the battery case and the volume-integrated heat release rate resulting from thermal abuse reactions and combustion.

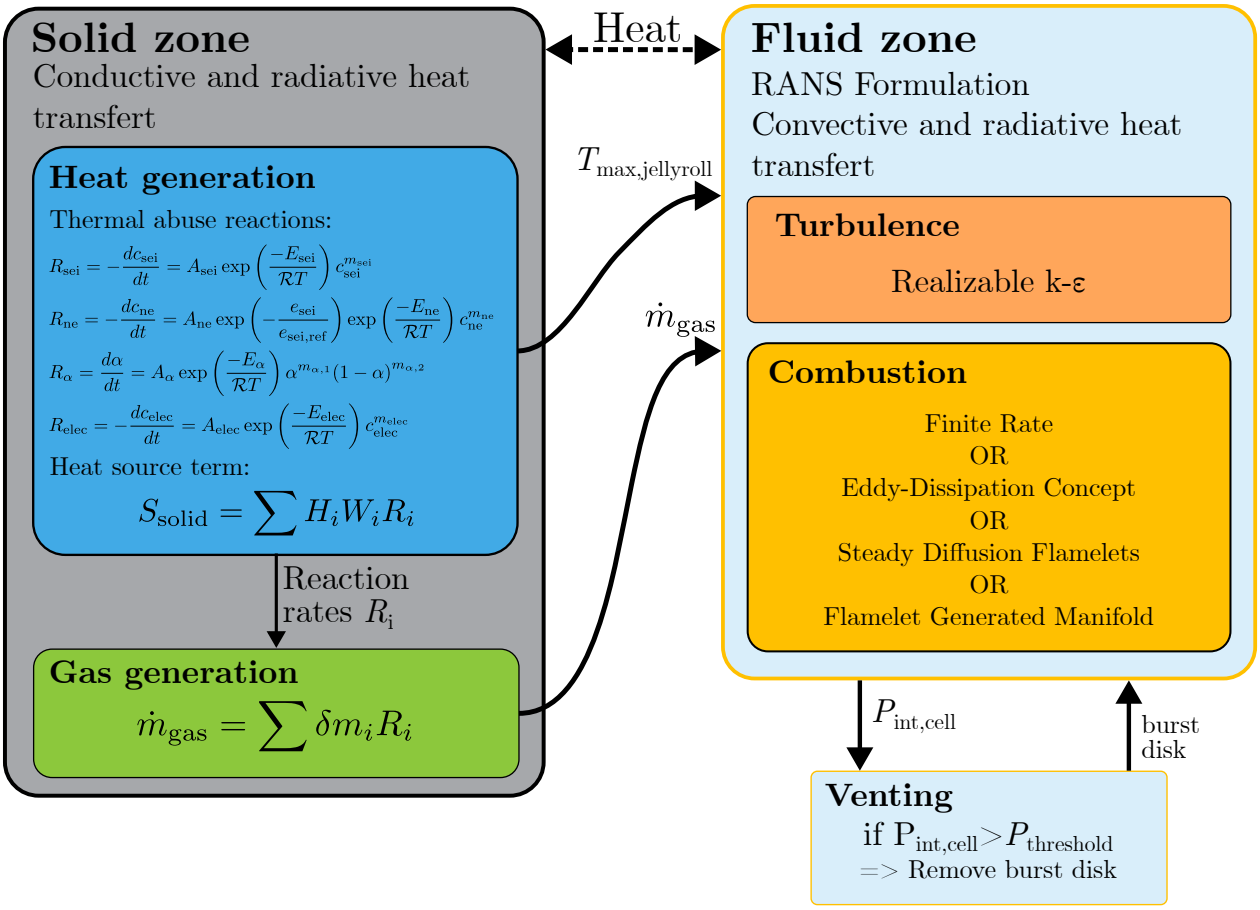

Figure 3.5 Flow chart of the coupled model

Table 3.4: List of input parameters used in the model

Parameter	Value	Unit	Ref.
Gas composition: H_2	30.8	%	[36]
Gas composition: CO_2	41.2	%	[36]
Gas composition: CO	13.0	%	[36]
Gas composition: CH_4	6.8	%	[36]
Gas composition: C_2H_4	8.2	%	[36]
A (SEI Decomposition)	1.667e15	1/s	[92]
E (SEI Decomposition)	1.3505e5	J/mol	[92]
W (SEI Decomposition)	2.57e5	g/m^3	[92]
H (SEI Decomposition)	610.4e3	J/g	[92]
m_0 (SEI Decomposition)	1	-	[49]
A (Negative-Solvent Reaction)	2.5e13	1/s	[92]
E (Negative-Solvent Reaction)	1.3505e5	J/mol	[92]
W (Negative-Solvent Reaction)	1.714e6	g/m^3	[92]
H (Negative-Solvent Reaction)	610.4e3	J/g	[92]
m_0 (Negative-Solvent Reaction)	1	-	[49]
A (Positive-Solvent Reaction)	2.25e14	1/s	[92]
E (Positive-Solvent Reaction)	1.475e5	J/mol	Fitted
W (Positive-Solvent Reaction)	7.9e5	g/m^3	[92]
H (Positive-Solvent Reaction)	1.293e3	J/g	[92]
m_0 (Positive-Solvent Reaction)	1	-	[49]
m_1 (Positive-Solvent Reaction)	1	-	[49]
A (Electrolyte Decomposition)	5.14e25	1/s	[92]
E (Electrolyte Decomposition)	2.74e5	J/mol	[92]
W (Electrolyte Decomposition)	1.55e5	g/m^3	[92]
H (Electrolyte Decomposition)	406.9e3	J/g	[92]
m_0 (Electrolyte Decomposition)	1	-	[49]

Continued on next page

Table 3.4: List of input parameters used in the model (Continued)

Parameter	Value	Unit	Ref.
δ (SEI Decomposition)	0.080	g	Fitted
δ (Negative-Solvent Reaction)	0	g	[56]
δ (Positive-Solvent Reaction)	0.1	g	Fitted
δ (Electrolyte Decomposition)	5.5	g	Fitted
Density (Jellyroll)	[2720-2380]	kg/m^3	[52] and Fitted
Heat Capacity (Jellyroll)	1100	J/kg.K	[52]
Thermal Conductivity (Jellyroll)	0.8	W/m.K	[52]
Share of jellyroll consumed	0.125	-	Fitted
Emissivity	0.8	-	[58]

CHAPTER 4 RESULTS

This chapter presents the main results from the combustion model investigation and the thermal runaway simulations. It begins with a mesh independence study, followed by results on auto-ignition and heat release calculated by the various combustion models. Next, the phases of the numerical simulated thermal runaway are described, with a focus on the main TR event. Finally, a two-cell setup is used to demonstrate the model's effectiveness in capturing battery behavior, along with a brief investigation into the impact of thermal abuse parameters.

4.1 Mesh and timestep size study

Mesh independence studies were conducted on the solid (jellyroll) and the fluid (exterior domain) zones. The effect of timestep size on thermal abuse reactions is also studied.

4.1.1 Solid zone

The jellyroll mesh was refined by reducing the maximum cell length parameter in Fluent Meshing. Four meshes were studied with maximum cell lengths of 1.5 mm, 0.5 mm, 0.4 mm, and 0.35 mm, resulting in 52,107 cells, 172,295 cells, 326,444 cells, and 483,778 cells, respectively. The tests were conducted with a timestep size of 5 ms. Figure 4.1 plots the mean jellyroll temperature during TR and Table 4.1 gives the maximum jellyroll mean temperature reached, the time when this value is reached and the total energy released by thermal abuse reactions for the different meshes. The maximum temperature reached, 750°C, is the same for all meshes, with the difference between the coarsest and finest mesh being less than 1°C. However, the temperature rise dynamics differ, as the maximum temperature is reached sooner with finer meshes, converging at a time of 7.3 s. The total energy released also converges, reaching a value of 23 kJ with minimal variation across the meshes.

Considering the minor difference between the meshes compared to total thermal runaway duration and energy released, the mesh with 172,295 is selected as a compromise between accuracy and computational costs.

The effect of the timestep size is also studied. The tests were conducted on the finest mesh presented above. Figure 4.2 plots the mean jellyroll temperature during TR and Table 4.2 gives the maximum jellyroll mean temperature reached, the time when this value is reached and the total energy released by thermal abuse reactions for the three timestep sizes studied.

Table 4.1 Compared quantities on the solid mesh study

Cell number	Max JR mean temp [°C]	Time at maximum Temp [s]	Total energy Released [kJ]
52,107	748.64	7.54	23.07
172,295	750.08	7.40	22.68
326,444	749.42	7.3	23.00
483,778	749.55	7.3	22.95

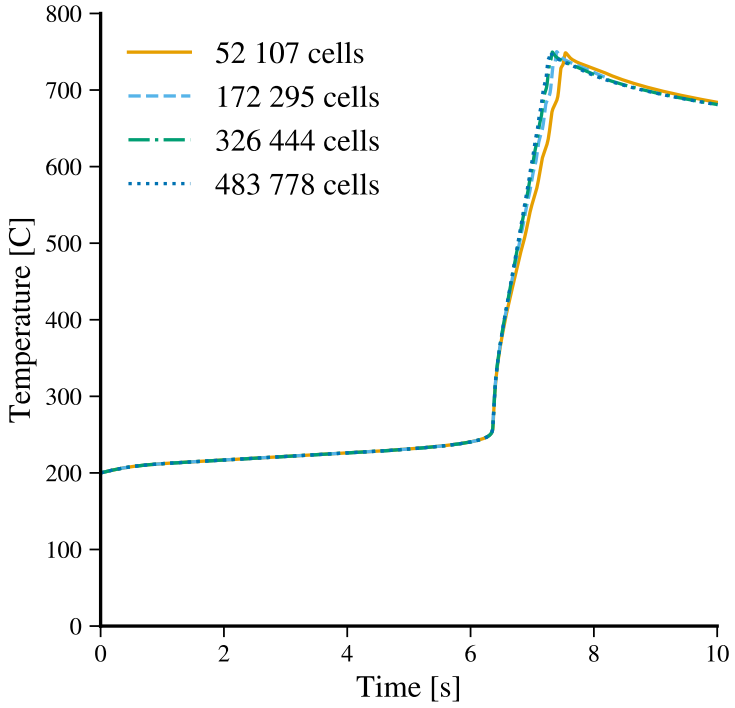

Figure 4.1 - Mean jellyroll temperature for different meshes

Table 4.2 Compared quantities on the solid timestep size study

Timestep size [ms]	Max JR mean temp [°C]	Time at max temp [s]	Total energy released [kJ]
100	772.94	9.0	23.95
5	749.55	7.3	22.95
1	750.10	7.1	24.5

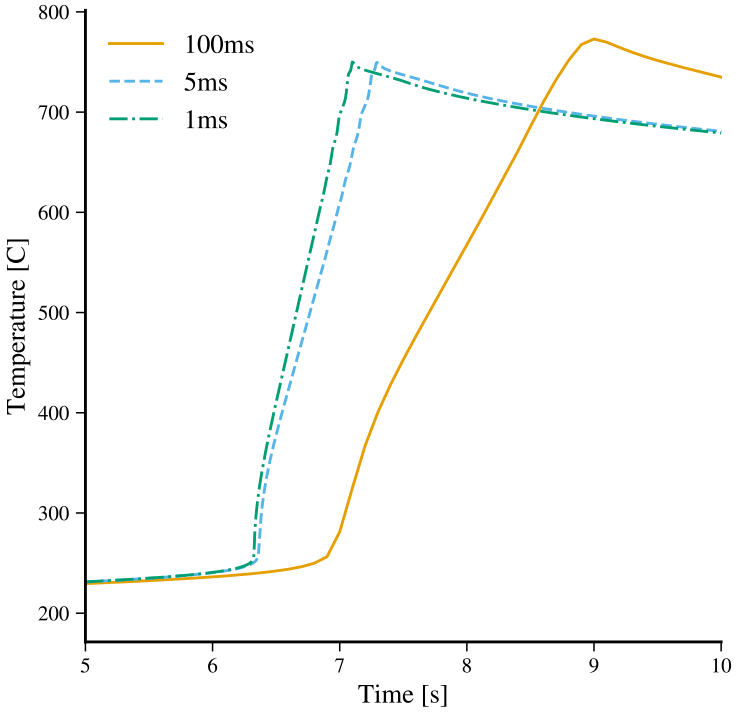

Figure 4.2 - Mean jellyroll temperature for different timestep sizes

These results show an important dependence of the thermal abuse model on the timestep size. With a timestep size of 1 and 5 ms, results are close to but are not converged, and a timestep size of 100 ms yields over-estimated values in all studied quantities.

According to Ostanek et al. [98], accurately solving the thermal abuse model requires a timestep size of 2.6 ns during the peak of heat generation due to the stiffness of the equations. This value is not usable from an industrial point of view as the simulation times would be too important. A timestep size of 1 or 2 ms offers a good compromise between accuracy and costs and is similar to the timestep size used in most numerical models in the literature [99].

4.1.2 Fluid zone

The mesh independence study for the fluid zone was conducted using the geometry presented in Figure 3.2. The Finite-Rate/No model was employed to solve the combustion, with the gas mixture vented at 1500°C to induce ignition. A timestep size of 1 ms was used.

The mesh was refined by reducing the maximum face cell length, but this refinement was applied only to a limited section of the gas domain, immediately downstream of the cell, as shown in Figure 3.2. The maximum face cell length values used were 5 mm, 2.5 mm, 2 mm, and 1.5 mm, resulting in a total of 203,859 cells, 609,008 cells, 1,015,633 cells, and 2,077,294 cells, respectively.

Figure 4.3 plots the maximum temperature after 0.1 s in the fluid zone for the different meshes. It was noted that no ignition occurred with the coarser mesh; therefore, it was excluded from further comparisons. The maximum temperatures at $t = 0.1$ s are 1929.2°C, 1947.6°C, and 1947.9°C for the meshes with 609,008 cells, 1,015,633 cells, and 2,077,294 cells, respectively. The maximum temperature during steady-state converged on the two finest meshes; therefore, the mesh with 1,015,633 cells was selected to reduce memory usage and computational costs compared to the finest mesh.

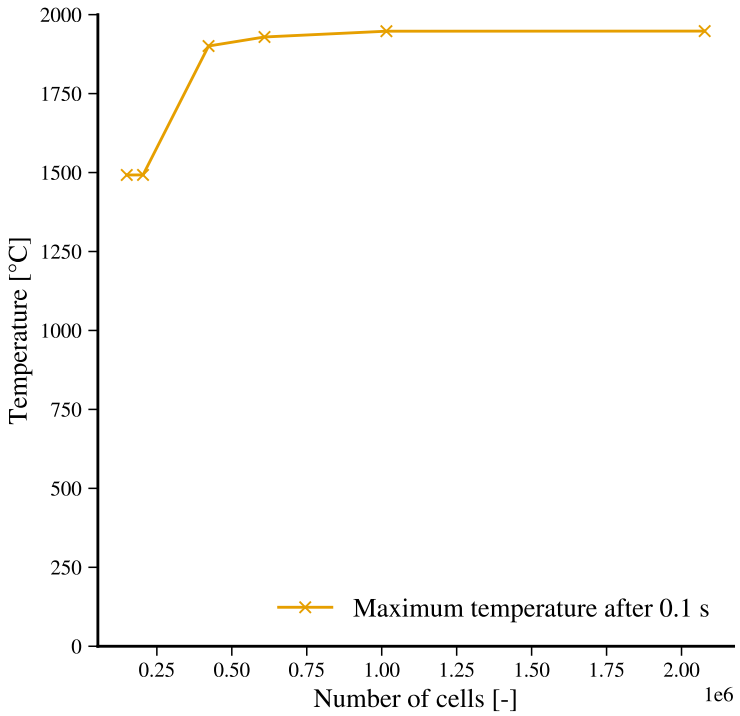

Figure 4.3 - Maximum temperature in the fluid zone for different meshes

The influence of timestep size is combustion model dependent and is discussed in the next section.

4.2 Investigation of the combustion models

In this section, the four combustion models presented in Section 3 are investigated: Finite-Rate (FR), Eddy-Dissipation Concept (EDC), Steady Diffusion Flamelets (SDF) and Flamelet Generated Manifold (FGM). Key aspects of each model are examined, including the heat release rate calculation, ignition process, and computational costs.

The combustion models are investigated using the geometry presented in Figure 3.2 with some adjustments to reduce computational costs. The total cylindrical enclosure height was reduced to 400 mm. The heat generation, venting, and radiation models are disabled. The mass flow rate at the gas inlet is set to 0.5 g/s. This mass flow value is equivalent to the slow sustained ejection of gases computed by Cellier et al. [55] from the experimental data of Golubkov et al. Unless specified otherwise, a timestep size of 1 ms is used throughout this section.

4.2.1 Heat release Rate

The heat release rate is a crucial factor in combustion studies of thermal runaway. Only Kim et al. [52] have computed the heat release rate during thermal runaway through a heat budget analysis. According to the Theory Guide provided by Ansys [90], the heat release rate is computed as follows:

$$\mathrm{HRR}_{\mathrm{Fluent}} = -\sum_i \frac{h_i^0}{M_i}\overline{R_i} \tag{4.1}$$

where h_i^0 is the specific enthalpy, M_i is the molecular weight, and $\overline{R_i}$ is the RA net rate of production of species i. However, to enable the comparison with the heat release rate measured in the calorimeter, the heat release rate needs to be approximated with the Oxygen Consumption (OC) method as defined in the standard ISO 5660-1 [100]:

$$\mathrm{HRR}_{\mathrm{OC}} = 13.1 \times 10^3 \times 1.10 \dot{m}_{\mathrm{outlet}} \frac{X_{\mathrm{O_2,inlet}} - X_{\mathrm{O_2,outlet}}}{1.105 - 1.5 X_{\mathrm{O_2,outlet}}} \tag{4.2}$$

with 13.1×10^3 the amount of energy released by mass of oxygen consumed (in MJ/kg), 1.10 is the ratio of the molecular weights of oxygen and air, $\dot{m}_{\mathrm{outlet}}$ the mass flow at the outlet in (kg/s), $X_{\mathrm{O_2,inlet}}$ and $X_{\mathrm{O_2,outlet}}$ are the oxygen mole fractions at the inlet and outlet, respectively. The heat release rate computed with both methods is investigated by forcing

the ignition of the models either by increasing the inlet temperature or setting the progress variable to 1.

Finite-Rate/No-model

Figure 4.4 shows the heat release rate computed with Eq.(4.1) and by the oxygen consumption method (Eq.(4.2)) using the FR model. To ignite the vented gas, the inlet temperature was set to 1500°C. The heat release rate computed with Eq.(4.1) increases rapidly within the first milliseconds after venting begins, while the oxygen consumption method shows a slower rise over the first 100 ms before quickly rising at $t = 100$ ms. After 0.5 s, the heat release rate values are 5.18 kW with Eq.(4.1) and 6.78 kW with the oxygen consumption method, with the latter differing from the heat release rate by 30%. The total energy released during the 0.5 s interval is 2.50 kJ with Eq.(4.1) and 2.71 kJ for the oxygen consumption method. The latter has a temporal lag because the combustion products must reach the outlet before the heat release rate can be computed. This lag is expected and is governed by the convective time of the flow.

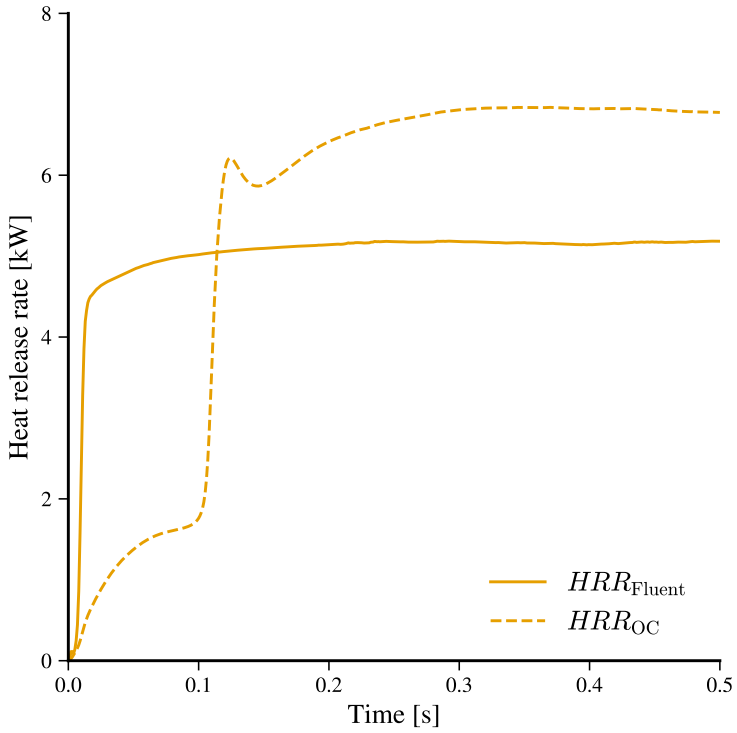

Figure 4.4 - Heat release rate computed with Eq.(4.1) and using the oxygen consumption method when using the FR model

Eddy-Dissipation Concept

Figure 4.4 plots the heat release rate computed with Eq.(4.1) and by the oxygen consumption method using the EDC model. To ignite the vented gas, the inlet temperature was set to 1800°C. The heat release rate computed with Eq.(4.1) starts by decreasing, reaching -1.5 kW within the first milliseconds after venting begins. The heat release rate then increases until reaching a steady-state value of 5.25 kW after 200 ms. With the oxygen consumption method, no negative HRR is observed. The approximated value slowly increases and reaches a value of 6.64 kW after 0.5 s. The oxygen consumption method predicts a heat release rate 26.5% higher compared to the value computed with Eq.(4.1). The total energy released during this 0.5 s interval is 1.93 kJ with Eq.(4.1) and 2.12 kJ for the oxygen consumption method.

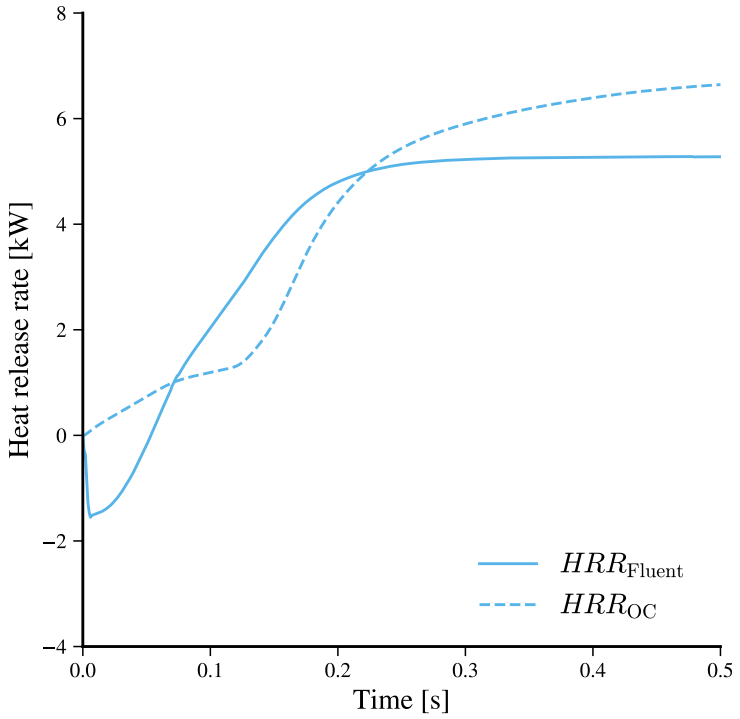

Figure 4.5 - Heat release rate computed with Eq.(4.1) and using the oxygen consumption method when using the EDC model

The observed negative HRR during the initial venting phase requires further investigation. The impact of timestep size on the negative heat release rate with the EDC model is studied by reducing the timestep by factors of 10 and 100. The heat release rate computed with Eq.(4.1) for different timestep sizes during the first 10 ms is plotted in Figure 4.6. In this configuration, the inlet temperature is set to 900°C to avoid ignition. As the timestep size

decreases, the negative heat release rate also diminishes. At a timestep size of 1 ms, heat release rate reaches -0.7 kW, compared to -0.5 kW and -0.15 kW for timestep sizes of 100 μs and 10 μs, respectively. This shows that the Eddy Dissipation Concept model computation of the heat release rate highly depends on the timestep size.

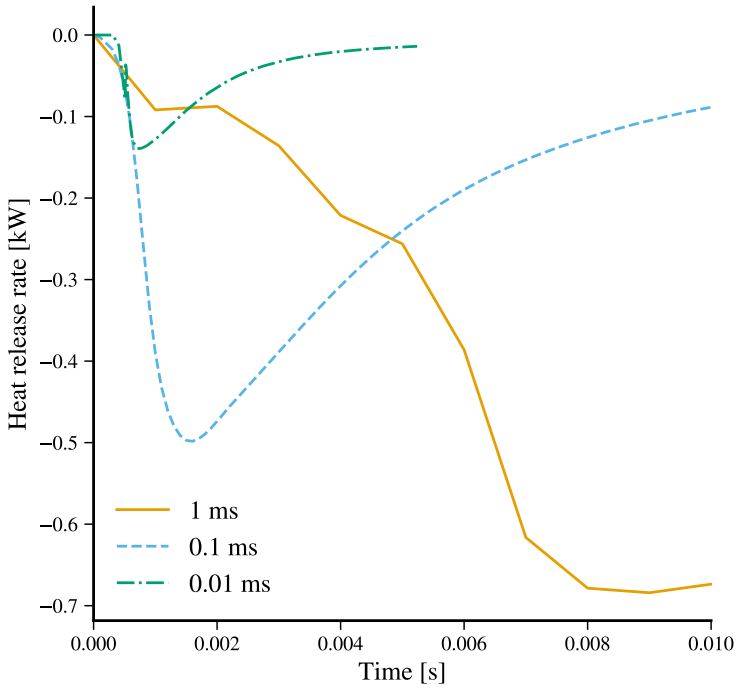

Figure 4.6 - Heat release rate from the EDC model computed with Eq.(4.1) during the first 10 ms

However, a timestep size of 10 μs is not viable when simulating a TR lasting tens of seconds, especially if such a small timestep size is required even when the venting gas is not ignited. Furthermore, reducing the timestep size does not fully resolve the negative heat release rate issue, indicating that the root cause remains unidentified. Other aspects of the EDC model, such as the mixing timescale (Eq.(3.25)), require further investigation.

Reduced-Order models

Figure 4.7 shows the heat release rate computed with Eq.(4.1) and by the oxygen consumption method for both the SDF and FGM models. With these models, the inlet temperature is set at 900°C and for the FGM model, the progress variable is set at 1 in the domain. The profiles of the two models present similarities. The heat release rate computed with Eq.(4.1) quickly drops to -3.4 kW during the first milliseconds and remains constant for nearly 100 ms. At $t =$ 0.1 s, the heat release rate starts to rapidly increase and reaches a steady-state value. After

0.5 s, the computed value of heat release rate with SDF is 5.57 kW for a total released energy of 1.79 kJ. With FGM, the computed heat release rate value is 6.0 kW and the total energy released is 1.87 kJ. When using the oxygen consumption method, the computed heat release rate remains at zero or close to zero in both models for the first 80 ms. This means that negative heat release rate is not associated with the release of O_2 from fuel decomposition. The approximated heat release rate value after 0.5 s is 5.83 kW and 6.19 kW for SDF and FGM, respectively. The approximated total released energy is 2.3 kJ for SDF and 2.4 kJ for FGM. Both model predicts similar results. The oxygen consumption method heat release rate final value still differs by +4.7% with SDF and +3.2% with FGM compared to the value computed with Eq.(4.1).

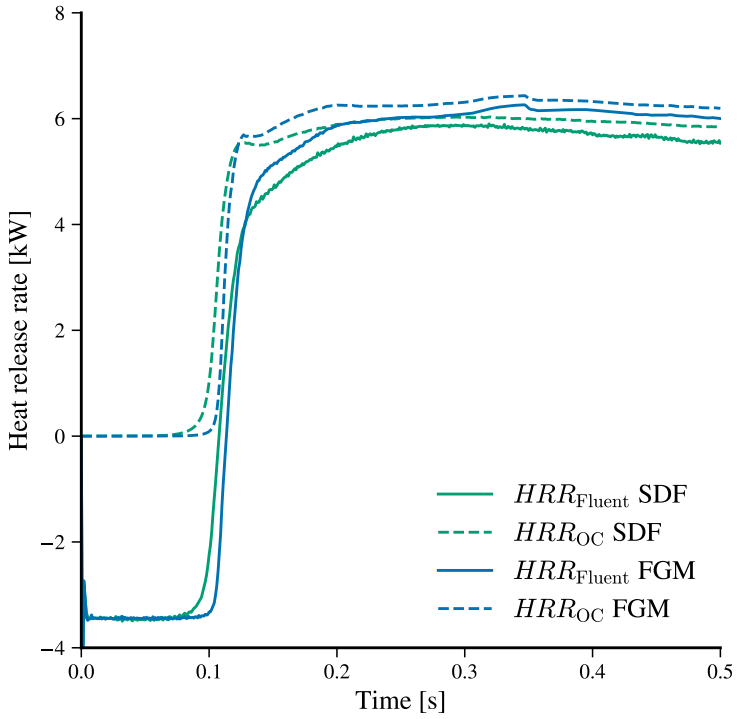

Figure 4.7 - Heat release rate computed with Eq.(4.1) and using the oxygen consumption method when using the SDF and FGM models

The negative value predicted with Eq.(4.1) is further investigated. First, the impact of the mesh and timestep size is investigated. For different timestep sizes, heat release rate profiles are shown in Figure 4.8a. For large timestep sizes, such as 100 ms, the heat release rate becomes negative only during the first timestep. However, as the timestep size is reduced, the negative period persists and becomes visible with timestep sizes of 10 ms and 1 ms. The consistent negative value of approximately -3.4 kW observed with the smallest timestep size suggests that this behavior is not dependent on the timestep size. For the mesh independence,

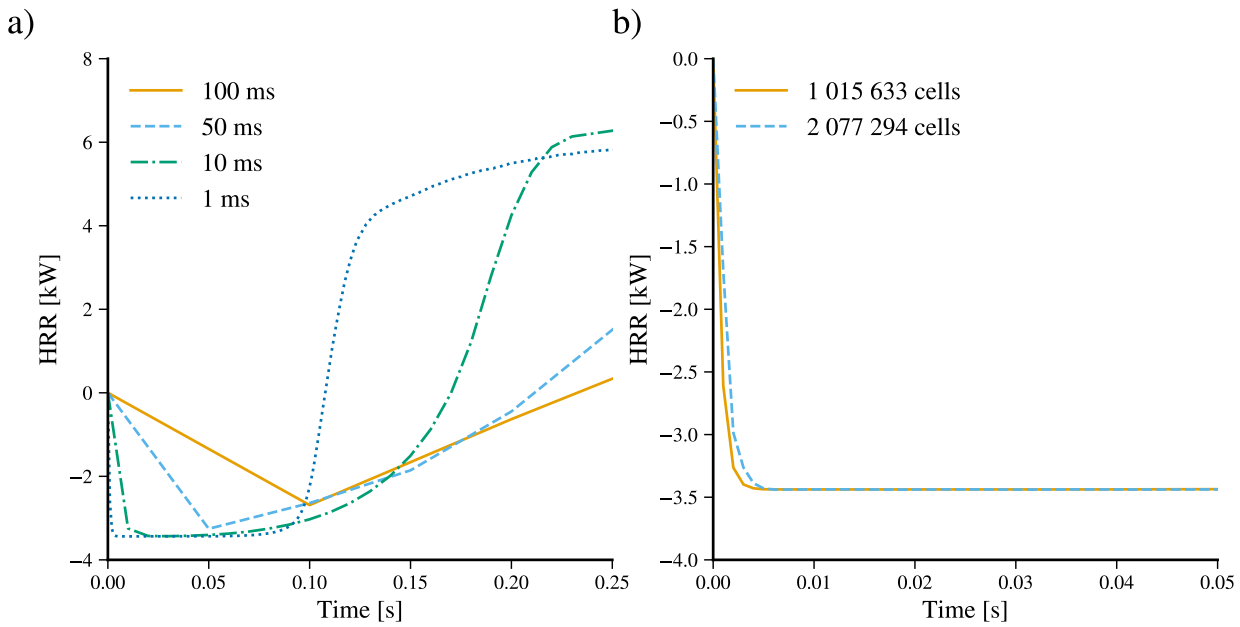

Figure 4.8 Heat release rate computed with Eq.(4.1) with the SDF model a) with different timestep sizes and b) on different meshes

the negative heat release does not change with a finer mesh as shown in Figure 4.8b.

Figure 4.8 suggests that the negative heat release rate is not dependent on the time and space discretization but directly related to the combustion models. This negative value is observed across all reduced-order models, regardless of whether they use the non-premixed or partially premixed approach, the flamelet hypothesis, and in both adiabatic and non-adiabatic cases. The root cause of the negative has not been identified and additional investigations are required on the PDF table calculations.

The main conclusions of the investigation on the heat release rate for the four models are:

- The oxygen consumption method heat release rate value differs by 25% to 30% with the species transport models, but only by 3% to 5 % with the reduced order models compared to the value obtained with Eq.(4.1).
- Negative heat release rate is obtained during early venting stages with EDC and the reduced-order models when the heat release rate is computed with Eq.(4.1). However, this period lasts up to 100 ms which represents only 1% of a TR duration. Nonetheless, it could impact the ignition process, as will be investigated and discussed in the following subsection.

4.2.2 Forced ignition

The forced ignition process of each model is investigated using the following simulation procedure: the inlet temperature is set at 900°C and simulation is run for 100 ms with a timestep size of 1 ms to allow the flow to exit the cell and reach a steady state. At $t = 0.1$ s, ignition is forced using a sphere of hot gas (2000°C) with a 2 mm radius placed 5 mm away from the three vents. During the ignition process, the timestep size is reduced to 10 μs before being gradually increased back to 1 ms once the flame appears. This procedure is designed to simulate conditions that replicate the thermal environment during the critical part of thermal runaway. The inlet temperature used is often found inside the jellyroll and the hot gas spheres replicate incandescent sparks generated by the cell during TR. A similar ignition procedure was used by Cellier et al. [55].

The forced ignition process using the FR model is investigated following the procedure described above. The HRR as a function of time is plotted in Figure 4.9. The temperature contours at different times are also shown to observe the flame throughout the ignition process. At $t = 0.1$ s, the sparks are added to the domain. The three jets ignite rapidly (Contour a)), reaching a peak HRR of approximately 7 kW (Contour b)). However, the jet velocity is too high for the flame to stabilize, causing it to blow off (Contour c)) and the heat release rate to drop back to zero after 50 ms (Contour d)).

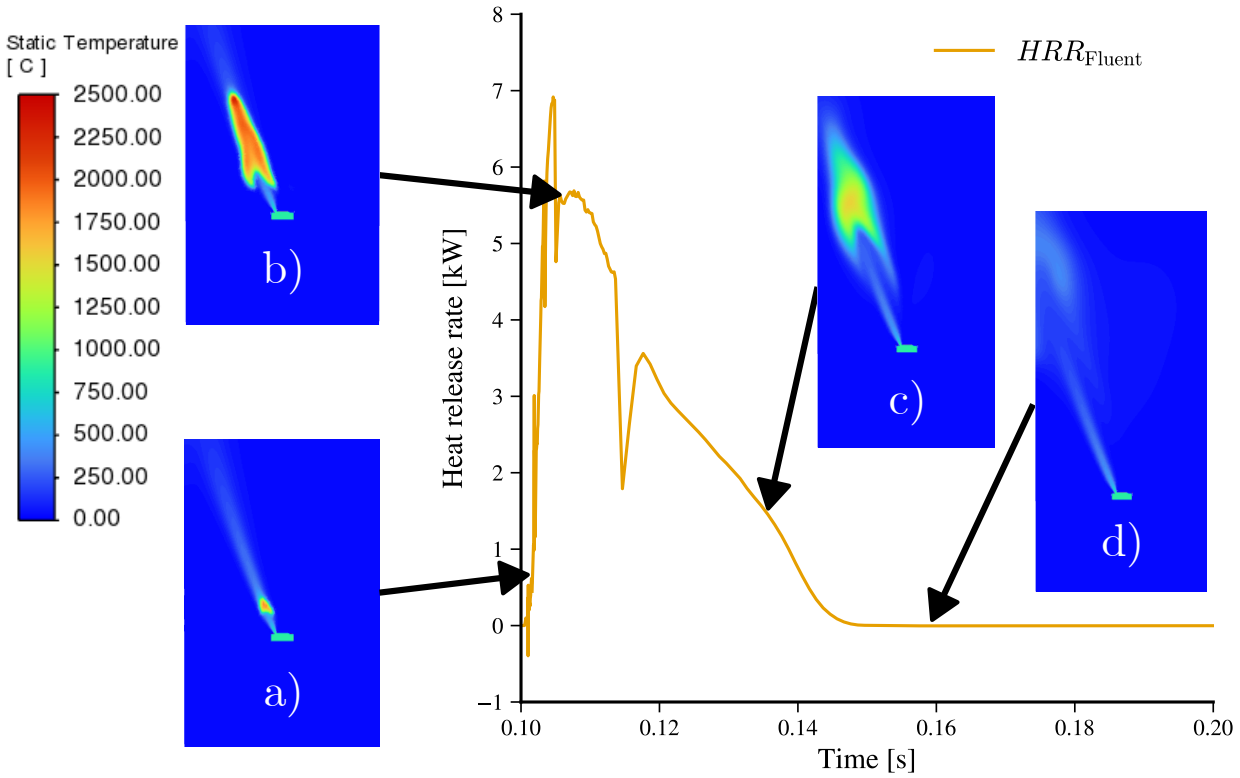

Figure 4.9 - Heat release rate computed by Fluent with forced ignition using the FR model. a), b), c), and d) are the temperature contours at $t = 0.103$ s, 0.107 s, 0.135 s, and 0.16 s, respectively

Figure 4.10 plots the heat release rate computed with Eq.(4.1) as the function of time using the EDC model. The sparks are added at $t = 100$ ms. However, in less than 5 ms the heat release rate dropped back near its original value indicating that no ignition occurred.

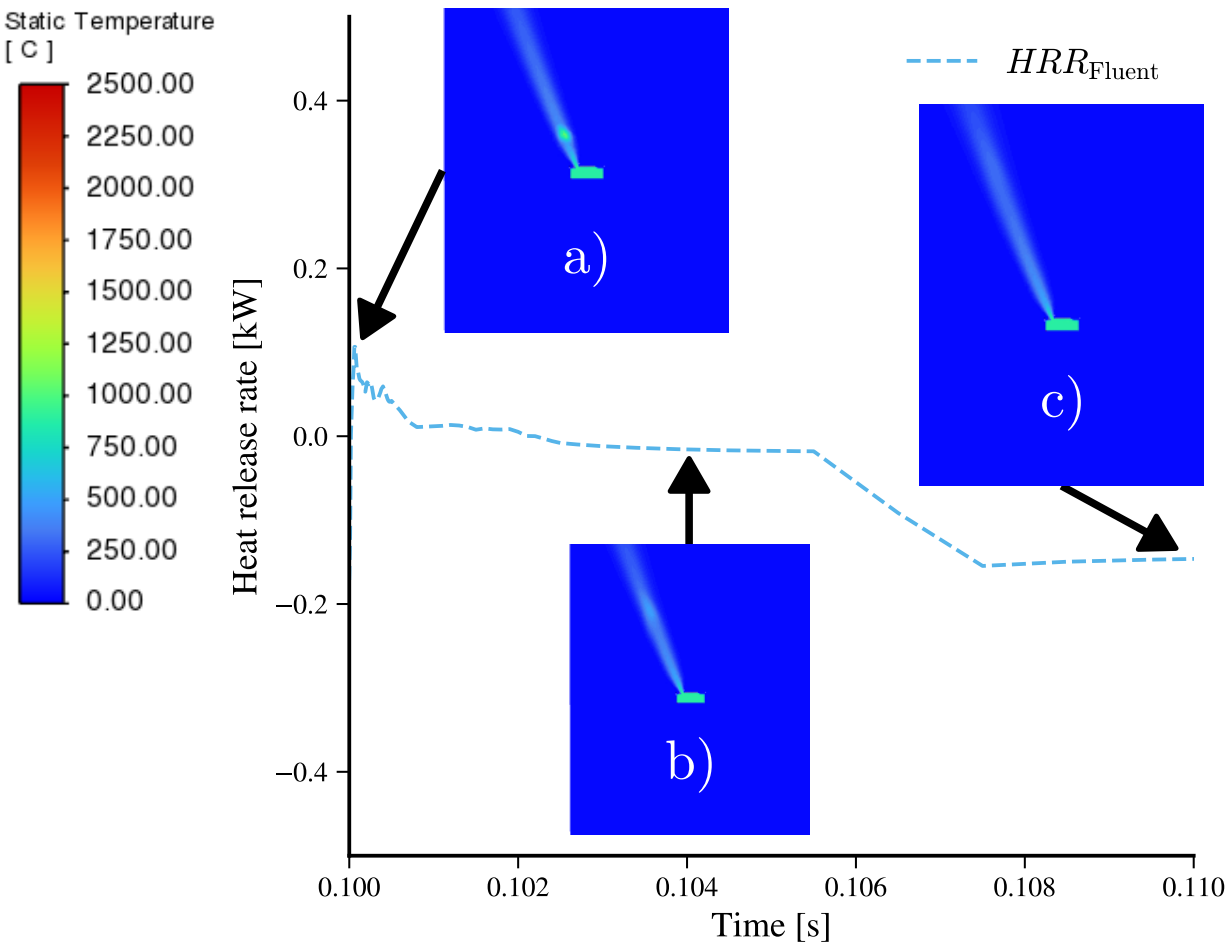

Figure 4.10 - Heat release rate computed with Eq.(4.1) with forced ignition using the EDC model. a), b), and c) are the temperature contours at $t = 0.1001$ s, 0.104 s, and 0.11 s, respectively

The forced ignition process using the SDF model is not investigated as the model is not equipped to capture ignition due to immediate fuel combustion upon mixing with the oxidizer. However, the ignition process can be studied using the FGM model. In this model, the temperature is tabulated as a function of mixture fraction and progress variable, so, to reproduce the sparks, the progress variable is set at 1 in the sphere instead of setting the temperature at 2000°C. The HRR computed by Fluent after the forced ignition as a function of time is plotted in Figure 4.11. Temperature contours are also shown in Figure 4.11 with the ignition (Contour a)) and stabilization (Contour b)) of the flame visible. After 100 ms, the flame is nearly fully developed and impinged the cylinder wall (Contour c)).

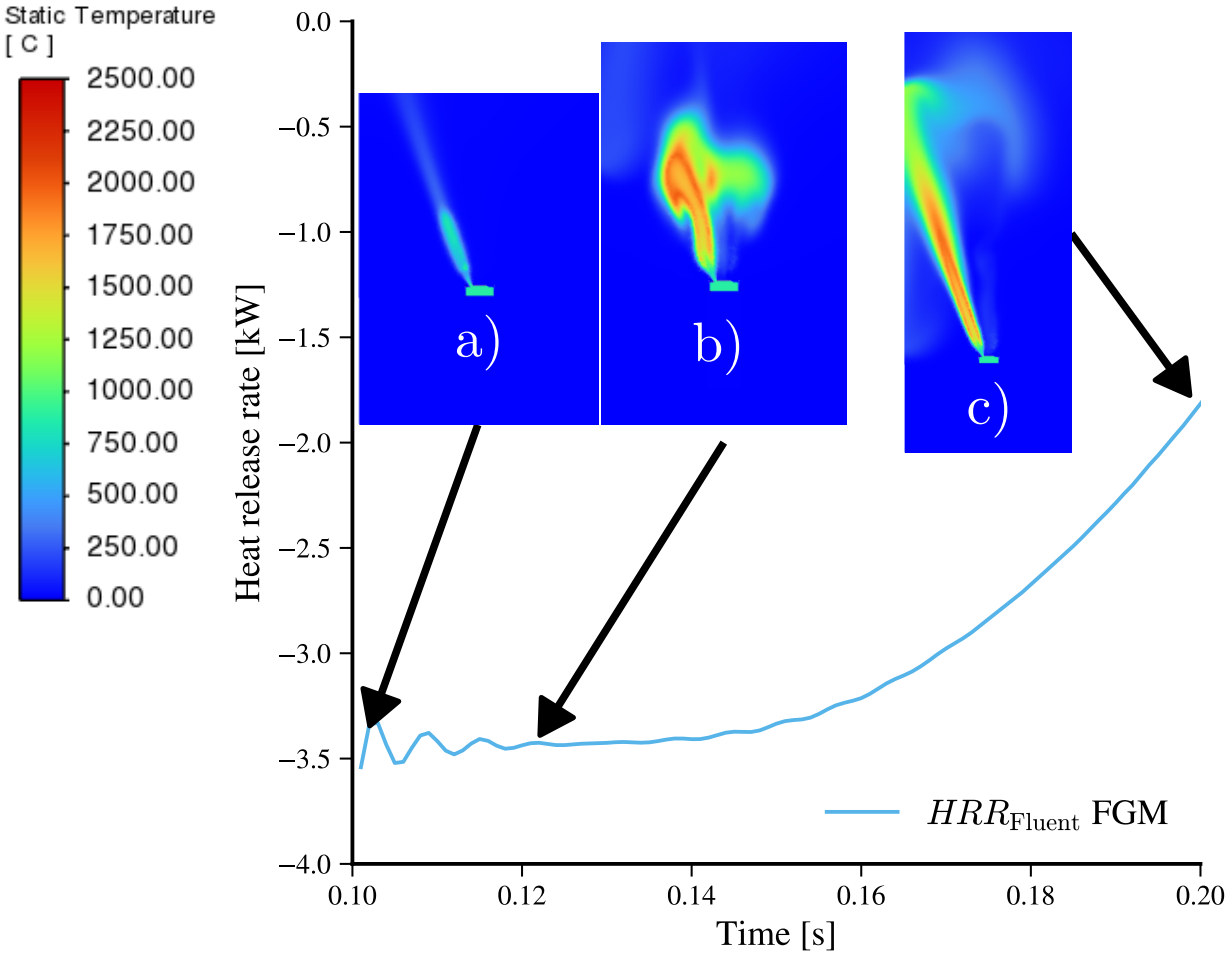

Figure 4.11 - Heat release rate computed by Fluent with forced ignition using the FGM model. a), b), and c) are the temperature contours at $t = 0.105$ s, 0.12 s, and 0.2 s, respectively

From this investigation of the ignition process, we can conclude that the negative heat release rate calculated at early stages from Fluent with Eq.(4.1) does not prevent forced ignition. Also, only FGM (and SDF) predict ignition for the relevant case study here. Spark placement and venting velocity are parameters that may influence forced ignition and require further study.

4.2.3 Critical analysis

At the time of writing, no experimental data are available to compare the heat release rate values. However, Cellier et al. [55] conducted a similar setup using an LES simulation with the No-Model using identical mass flow rates and gas composition. They obtained a heat release rate of 6.2 kW during the steady-state period. The different ignition methods complicate

direct comparison, but all models predict an heat release rate within the same order of magnitude. No convincing explanation has been identified for the negative HRR values observed with the EDC, SDF, and FGM models, warranting further investigation. In the forced ignition process, sustained ignition is not achieved with either species transport model with this configuration.

Overall, each model presented here has its strengths and weaknesses when it comes to simulating the turbulent combustion of gases vented from a cell. The Finite-Rate model provides the most reasonable prediction of the time evolution of HRR, but it does not account for the impact of turbulence on the reaction rates calculations and comes with high computational costs. The Eddy-Dissipation Concept model exhibits negative heat release rate values and requires a very small timestep size, which leads to non-viable computational costs. Reduced-order models predict an heat release rate magnitude similar to that obtained with the Finite-Rate model during steady-state but predict negative values during the early stage of gas venting. However, they are much less sensitive to timestep size and are associated with significantly lower computational costs (6 times less than FR or EDC).

The non-premixed approach with the steady diffusion flamelets is chosen for the full thermal runaway simulation as it matches peak HRR and total heat release compared to FR, at a fraction of the cost. This approach also has the advantage of simplifying the ignition process and heavily reducing the computational costs compared to the other models considered.

4.3 Thermal runaway simulation

The thermal runaway simulation is carried out with the full geometry presented in Figure 3.2 with all the models presented in the methodology section enabled. The simulation results are compared with experimental data obtained from calorimeter tests on ten 18650-25R cells. The test results are averaged before comparison to evaluate the model's capacity to capture thermal runaway accurately. To fit the thermal abuse parameters for the studied cell, a parametric study was conducted and it is described in Appendix B. The parameters used in this section are given in Table 3.1.

4.3.1 Heating phase and first venting

During the first phase of TR, the cell is heated at a rate of 10°C/min by applying a volumetric energy source on the copper tube when the cell side case temperature is lower than the ramp. This setup replicates the experimental heating system temperature composed of two heating wires delivering 100 W of power controlled by a PID loop.

The case temperature and head-space pressure during the simulation are presented in Figure 4.12. At the start of the simulation, the cell temperature rises steadily following the heating ramp. During the first 400 seconds, the cell temperature remains below 120°C and the internal pressure constant as no thermal abuse reactions are progressing. Once the temperature exceeds 120°C, the SEI layer begins to decompose, slowly releasing gas. As the SEI decomposition progresses, the gas accumulates, causing the internal pressure to rise. The first venting occurs a $t = 640.0$ s when the internal cell absolute pressure reaches 1.6 MPa and the case temperature is recorded at 152.7°C. At this instant, the pressure disk inside the cell is changed from a wall to an internal boundary condition to allow the gas to flow freely. As soon as the disk is opened, the pressure starts dropping back to ambient and the cell continues to be heated at a constant rate until the TR is reached. This phase lasts 276 s until the cell reaches 196.6°C at $t = 916.0$ s, effectively entering TR. Contrary to the procedure described in RTCA's DO 311-A, the external heating is not cut off following the first venting to force the cell to undergo thermal runaway.

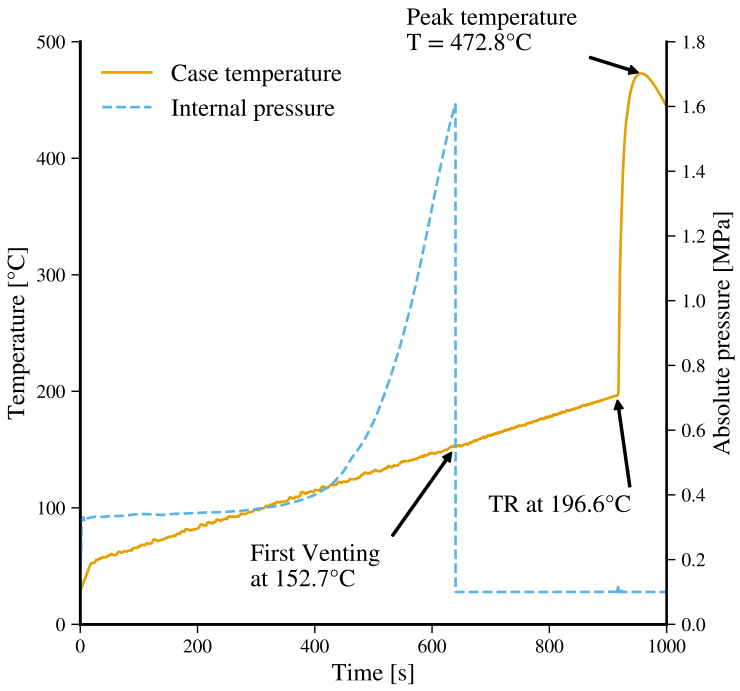

Figure 4.12 - Case temperature and head-space pressure during the simulation

Figure 4.13 gives the maximum velocity computed in the model. This value is located outside the cell, at the vent holes. The two main events of thermal runaway are visible. The first peak, reaching 787 m/s, corresponds to the initial venting, where the pressure within the cell drops, expelling 0.015 g of gas at high velocity. This peak is very brief, lasting only a few

microseconds. The second peak in Figure 4.13, reaching 372 m/s, corresponds to the most intense phase of thermal runaway and will be discussed in the next section.

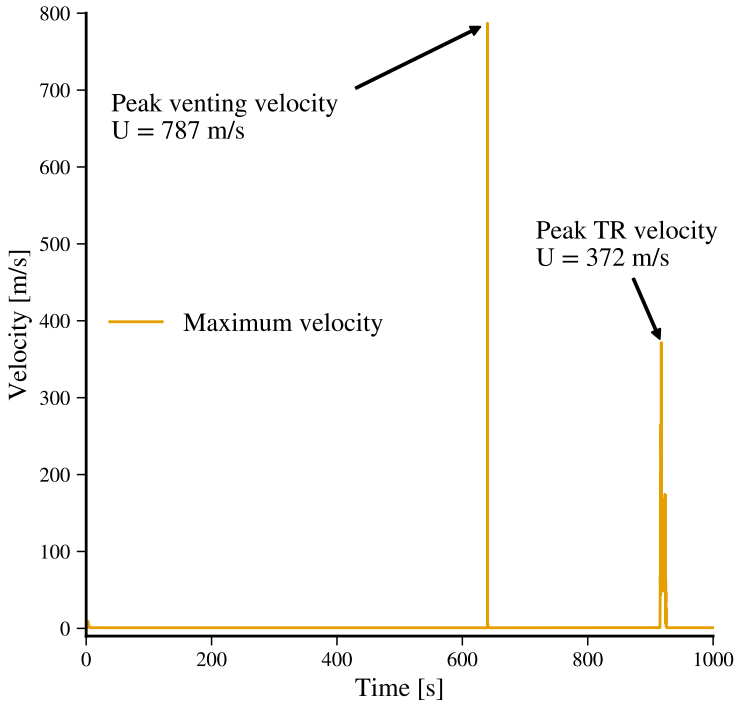

Figure 4.13 - Maximum computed velocity during the simulation

Figure 4.14 plots the thermal abuse parameters defined in Eqs.(3.40)-(3.44) as a function of time. As already discussed with Figure 4.12, during the first hundred seconds, the parameters remain constant as the cell temperature is too low for the thermal abuse reactions to progress significantly. Once the cell reaches 120°C, the SEI decomposition becomes visible with c_{sei} starting to decrease until reaching the first venting. At this time, the SEI generated 0.011 g of gas, the rest of the mass required to trigger the venting comes from the Positive-solvent reaction. After the first venting, the Negative-solvent begins generating heat at an increasing rate and the Positive-solvent reaction slowly progresses before accelerating in the tens of seconds before the main event. The electrolyte decomposition reaction requires a higher temperature thus only becoming significant during the main event.

The simulated heating phase can be compared to the experimental data, as the case temperatures of the tested cell were recorded using a thermocouple. During the experimental tests, the cell is heated at a rate of 10°C/min until the first venting occurs. Once the vent disk bursts open, heating is stopped to determine if the cell generates sufficient internal heat to undergo TR independently. After the cell has cooled, heating is resumed until the cell enters

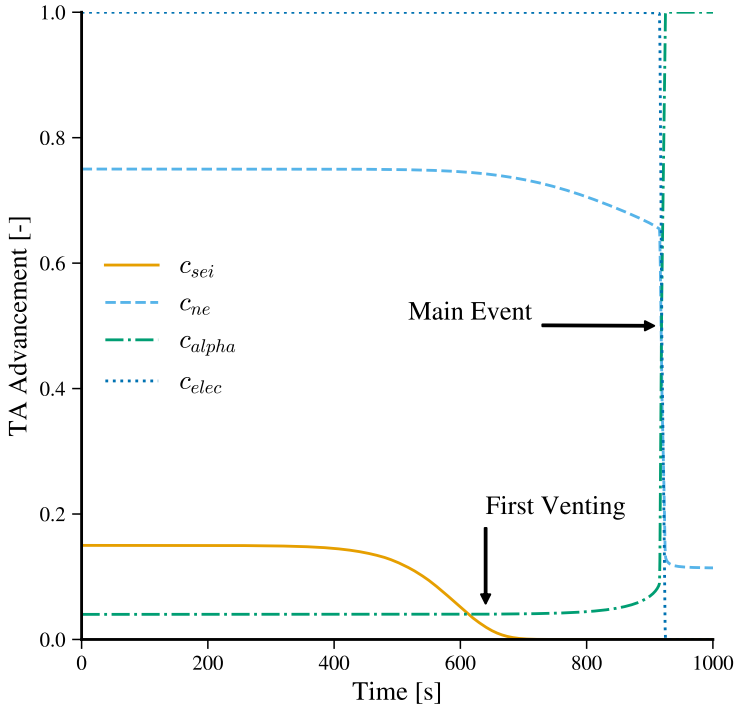

Figure 4.14 - Thermal abuse parameters during the simulation

thermal runaway. Numerically, heating is continuous to reduce simulation time and computational costs. While the case temperature cannot be directly compared, the first venting temperatures provide a basis for the comparison. Experimentally, the averaged first venting temperature is 171.4°C, with an observed range from 158.9°C to 184.5°C. The numerical model predicts a slightly earlier first venting at 152.7°C. To better match the experimental data, the first venting temperature in the model needs to be increased. This can be achieved by reducing the δ parameter for the SEI decomposition reaction without impacting any other parts of the model.

4.3.2 Main event

The main event corresponds to the most catastrophic part of TR, which lasts approximately 10 seconds, during which the cell case reaches a peak temperature of 472.8°C. The pressure inside the cell reaches 0.2 MPa during the main event and 5.6 g of gas is released.

Figure 4.15 illustrates the temporal evolution of the temperature contour during the main event. The 2D contour corresponds to the XY plane, displaying only one of the three vent holes. The view is cropped to focus on the lower part containing the cell. The main thermal runaway can be divided into three phases:

- Phase I: Intense initial phase where the peak gas generation and HRR are reached.
- Phase II: Lower steady-state phase.
- Phase III: Ending phase of TR with second lower peak.

During phase I, the TR initiates at t=915.3 s, at this point, a flame becomes visible above the cell as shown in Figure 4.15. No ignition effects are modeled because when using the non-premixed approach with steady diffusion flamelets, the flame appears immediately as the fuel and oxidizer mix. The flames take one second to expand and reach the wall of the cylinder. Between $t = 917$ s and $t = 918$ s, the peak of the thermal runaway is reached, with the vented gas reaching a maximum velocity of 372 m/s. During the peak, the heat starts to accumulate and a temperature rise can be observed in the cylinder. Past this point, the heat release rates start to decrease until reaching the steady phase (Phase II). It lasts from $t = 918$ s to $t = 923$ s. During this phase, the heat inside the cylinder starts to dissipate as fresh air arrives from the coflow. Finally, the second peak starts at $t = 923$ s and reaches a local maximum at $t = 924$ s. During this period, the flame begins to diminish as the cell generates less gas. Once the TR concludes, the flame disappears, and the cell starts to cool down.

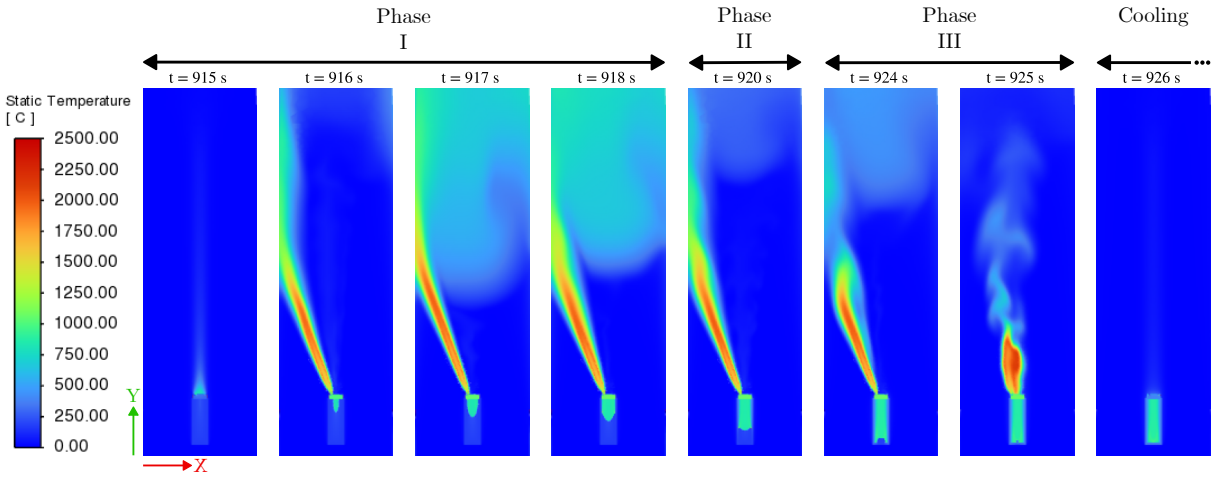

Figure 4.15 - Contours of temperature at different times during TR

The case temperature during the main event is compared to the experimental data and presented in Figure 4.16, demonstrating a good agreement during the initial seconds. As TR progresses, the model starts to under-predict the temperature compared to the mean values from the tests while staying within the confidence interval. The experimental peak temperature of 459°C is reached at $t = 939.8$ s whereas the model predicts a peak of 472.8°C

at $t = 956.3$ s. Finally, in the experiment, the cells cool faster than in the model. Due to the thermal conductivity of the jellyroll, heat takes time to reach the case. This causes the case temperature to continue increasing even after the thermal abuse reactions are complete.

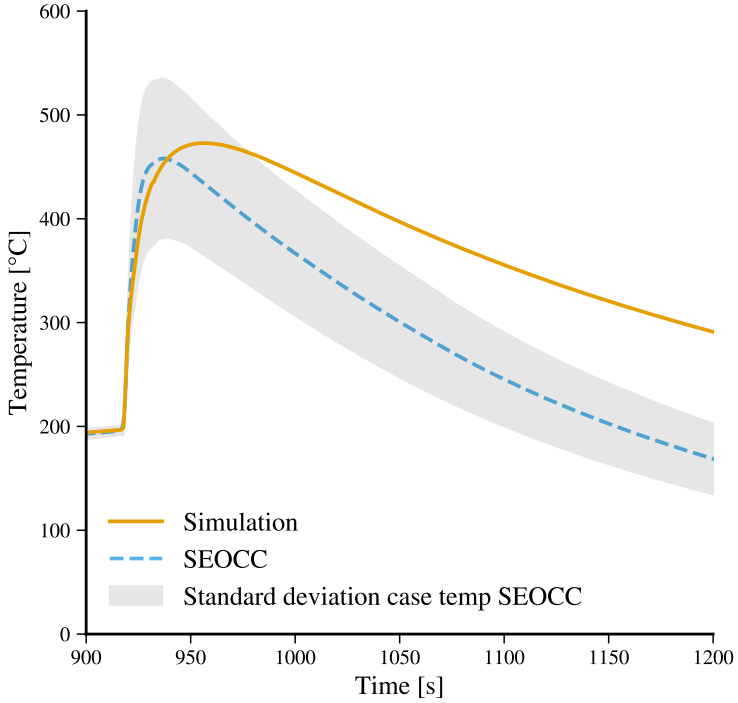

Figure 4.16 - Comparison of the case temperature between the numerical simulation and experimental data

The difference in peak temperature and cooling is mainly due to a thermal mass difference between the model and the experiments. With the numerical model, the cell loses only the mass of gas generated, 6.5 g in this study, whereas experimentally, 18650 cells can lose up to 30 g of mass during the TR. The average mass lost during the tests was 25.0 g. Most of this mass results from the ejection of solid particles and is caught by the mesh shown in Figure 3.1. In the experiments, the average mass captured in the mesh was 17.6 g.

Figure 4.17a shows the heat release rate due to the solid-phase, gas-phase, and the sum of both. The advancements of the different thermal reaction parameters are then plotted in Figure 4.17b. The heat release rate due to the gas-phase reactions is computed using the O_2 consumption method described in the previous section to enable the comparison with experimental data. The three phases described previously are also illustrated in Figure 4.17. During Phase I, both heat release rates steadily increase until they reach a maximum of 8.6 kW and 26.5 kW respectively both at $t = 917.35$. In Phase II, the thermal abuse parameters evolve linearly as can be seen in Figure 4.17. Finally, during Phase III, the thermal abuse

reactions accelerate before ending at $t = 925$ s while the gas phase reactions last for another second.

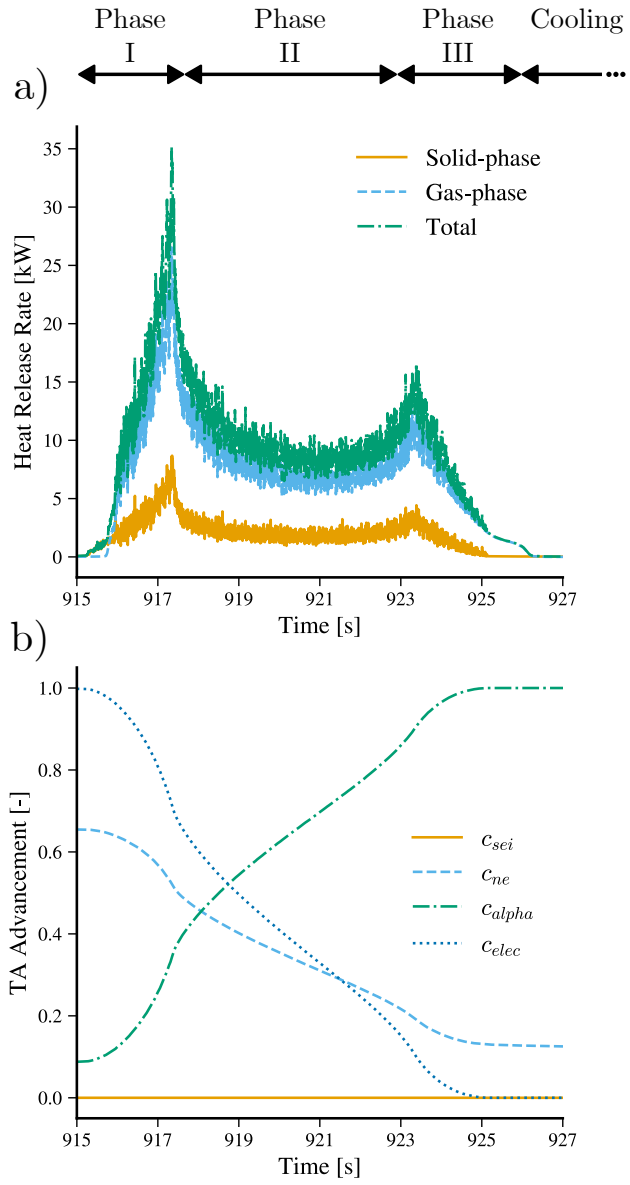

Figure 4.17 a) Heat release rate from solid-phase and gas-phase reactions, and their total, and b) advancement of thermal abuse parameters

The heat release rate of both the solid and gas phases show similar profiles, as gas generation is linked to the thermal abuse model. An increase in thermal abuse reactions produces more gases, increasing the gas-phase heat release rate. Additionally, the cell radiates up to 55 W to the environment with a profile following the case temperature. However, as the cell is placed inside the copper tube, a share of the heat generated by the cell is used to heat the tube, lowering the radiative heat load. It can be noted that as the wall of the cylinder is

impinged by the flames and heated, it radiates up to 1000 W with 80 W directly back to the cell during the initial phase of TR.

Thermal abuse reactions generate 24.21 kJ of energy while the combustion releases 83.17 kJ. During the TR, the heat generation is dominated by the combustion representing 81.6% of the total energy released.

Experimentally, the gas-phase heat release rate was measured using the oxygen consumption method, while the total power released by the cell was determined using the sensible enthalpy (SE) method under the assumptions of adiabatic wall conditions, uniform inlet and outlet conditions, and very lean combustion at the outlet.

$$\frac{dE_{\text{cell}}}{dt} = \dot{m}_{\text{air}} c_{\text{p,air}} \left(T_{\text{out}} - T_{\text{in}}\right) + \frac{dE_{\text{solid}}}{dt} + \dot{W}_{\text{ei}} \tag{4.3}$$

where $\dot{W}_{\text{ei}}$ is the electrical energy added to the system to trigger the TR and $\frac{dE_{\text{cell}}}{dt}$ represents the effect of energy accumulated in the solid parts of the calorimeter. To obtain the experimental data used for comparison, the measurements from the tests were averaged, and the standard deviation was calculated. The experimental data is temporally synchronized with the simulation results to facilitate the comparison.

Figure 4.18 compares the gas-phase heat release rate computed using the OC method with the result from the numerical simulation shown in Figure 4.17a. The experimental setup for O_2 sampling introduces a delay and smoothing effect in the heat release rate calculation, which are not accounted for in the numerical model. Experimentally, it is observed that the cell releases 124.94 kJ, whereas the model predicts 83.17 kJ, representing a 33% underestimation of the released heat from combustion.

Figure 4.19 plots the total heat release rate defined as the sum of the solid and gas phase heat release rate computed by the model alongside the experimentally computed power using the sensible enthalpy method. Experimentally, the sensible enthalpy at the inlet and outlet is computed using Cantera, based on the measured temperatures at these locations. The same calculation is performed using the simulation data, and the results are plotted in Figure 4.19.

When computing the total heat release as the sum of solid and gas phases heat release, the model predicts a peak heat release rate of 35.1 kW and a total energy release of 107.4 kJ. However, when applying the sensible enthalpy method, the model predicts a peak of 21.9 kW and a total energy of 74.0 kJ The calorimeter measured a peak heat release rate of 22.9 kW and a total energy of 193 kJ. With the first definition of total heat release rate, the peak heat release rate is over-predicted by 53.2%. Still, the total energy is underestimated by 44% compared to experimental observations. With the sensible enthalpy calculation, the

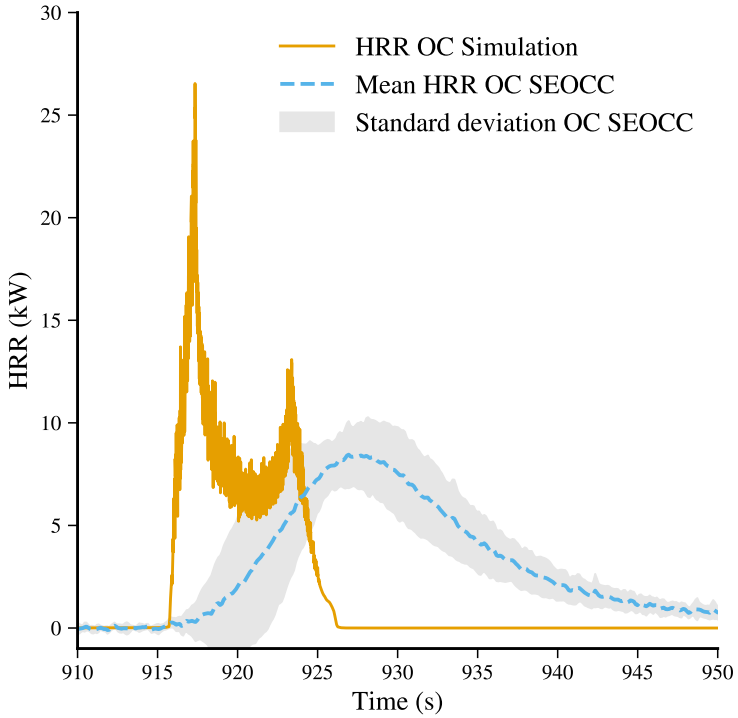

Figure 4.18 - Comparison of the gas phase heat release rate between the numerical simulation and experimental data

peak heat release rate is under-predicted by only 4% but the model predicts 61% less energy released than the calorimeter.

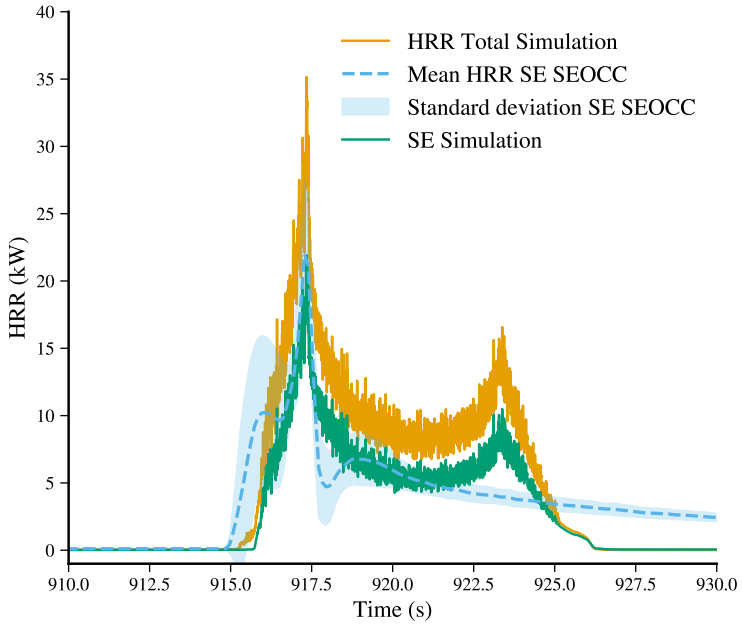

Figure 4.19 - Comparison of total heat release between the numerical simulation and experimental data

Overall, the model predicts a shorter thermal runaway that produces less energy but at higher power compared to experimental results. Moreover, the last phase of the numerical thermal runaway is not observed experimentally. The thermal runaway does not end with a peak but slowly diminishes releasing energy at low power over a longer period. Nonetheless, the model presented here shows a good capacity to capture the main features of the thermal runaway phenomenon.

Note that this model is not yet validated according to the certification ASME V&V20 - 2009 (Standard for Verification and Validation in Computational Fluid Dynamics and Heat Transfer) [101]. This standard requires among other things, quantification of the uncertainties, which would typically be obtained through a large campaign of simulations to assess error propagation. Given the numerical cost associated with such a campaign, this validation procedure is left outside of the scope of this thesis. However, based on the input parameters provided in Table 3.4, the primary source of uncertainty is likely attributable to the thermal abuse parameters and the gas composition, given the limited experimental data available for these parameters and the role they play on TR timing and heat release rate.

4.4 Battery pack modeling

This section demonstrates the model's capabilities in simulating a battery pack composed of multiple identical cells, each of which is capable of undergoing thermal runaway independently.

4.4.1 Geometry and configuration

A second battery is added to the geometry. Figure 4.20 shows the computational domain and cell positions. In Figure 4.20a the adiabatic wall is hidden to improve clarity. The horizontal cell-to-cell distance between the cells is 0 mm, with the second cell positioned 80 mm higher than the first to create vent gas impingement. This placement is chosen arbitrarily to force the second cell to undergo TR.

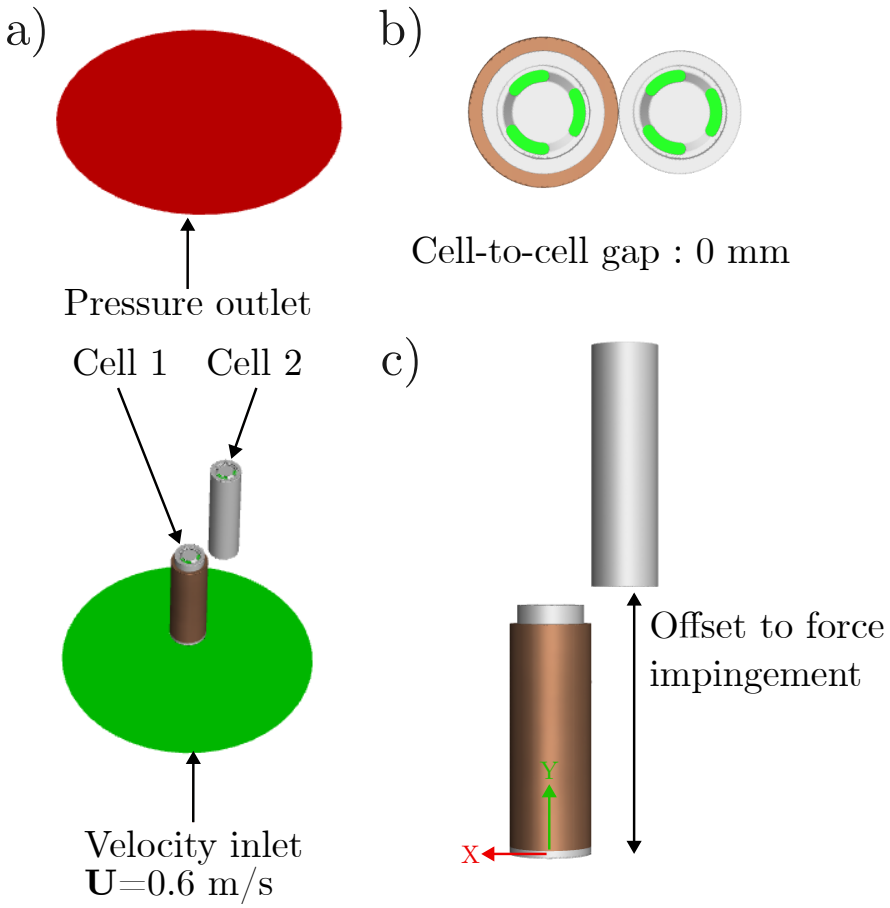

Figure 4.20 a) Isometric view of the domain, b) Top view, and c) Side view

This configuration serves as a proof of concept, demonstrating that the model presented in

this work can simulate multiple cells simultaneously. Each cell must be capable of undergoing thermal runaway, encompassing all associated phenomena—heat and gas generation, venting, combustion, and propagation. Additionally, computational costs must remain manageable to ensure the model's relevance for industrial applications. Consequently, the methodology and configuration have been adapted compared to the single-cell model. Most of the configuration remains the same, with only a few adjustments: venting and varying jellyroll density are not included, and the minimum timestep size used is 0.01 s. These adjustments were made to reduce the total computational time. Furthermore, the results presented here are only briefly analyzed and have not been compared with experimental data.

4.4.2 Results

The case temperatures of the two cells during the simulation are plotted in Figure 4.21. As for the single cell model, cell 1 is heated by the copper tube at a rate of 10°C/min and enters thermal runaway at $t = 920$ s. The case temperature of Cell 1 increases similarly to the single-cell model, reaching a maximum temperature of 417°C before cooling down. For Cell 2, its case temperature starts to rise when Cell 1 enters TR. A maximum temperature of 552°C is reached, which is higher due to the hot gas vented by cell 1.

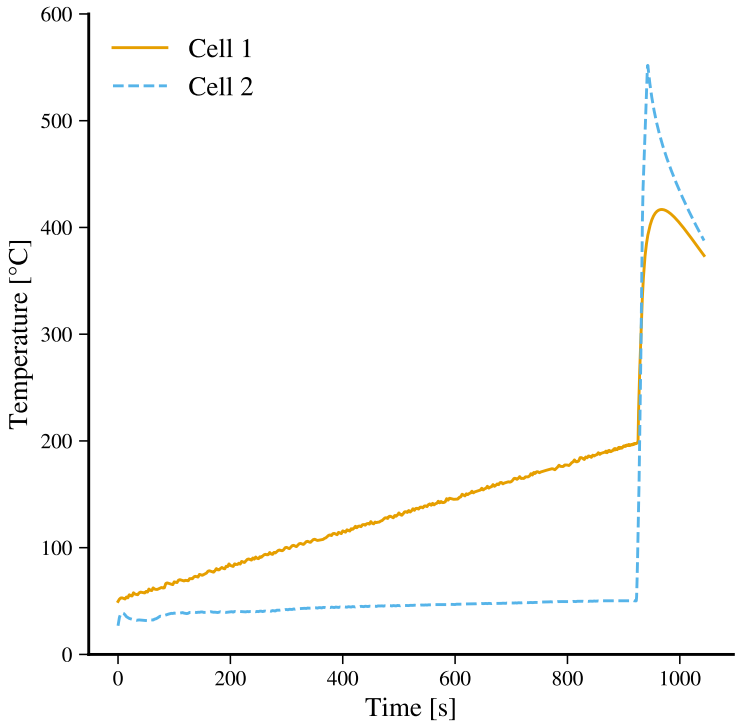

Figure 4.21 - Case temperature profile of each cell

Figure 4.22 shows the temperature contours at different times during the main event of both cells. At $t = 923$ s and $t = 925$ s, only Cell 1 is undergoing thermal runaway, with its jet of hot gas directly impinging on Cell 2. After a few seconds, thermal runaway initiates in Cell 2, beginning from the top left and middle left of the jellyroll. At $t = 940$ s, Cell 1 has started cooling, while Cell 2 is in the middle of its thermal runaway. Cell 2 continues its thermal runaway, and after $t = 945$ s, both cells are cooling down.

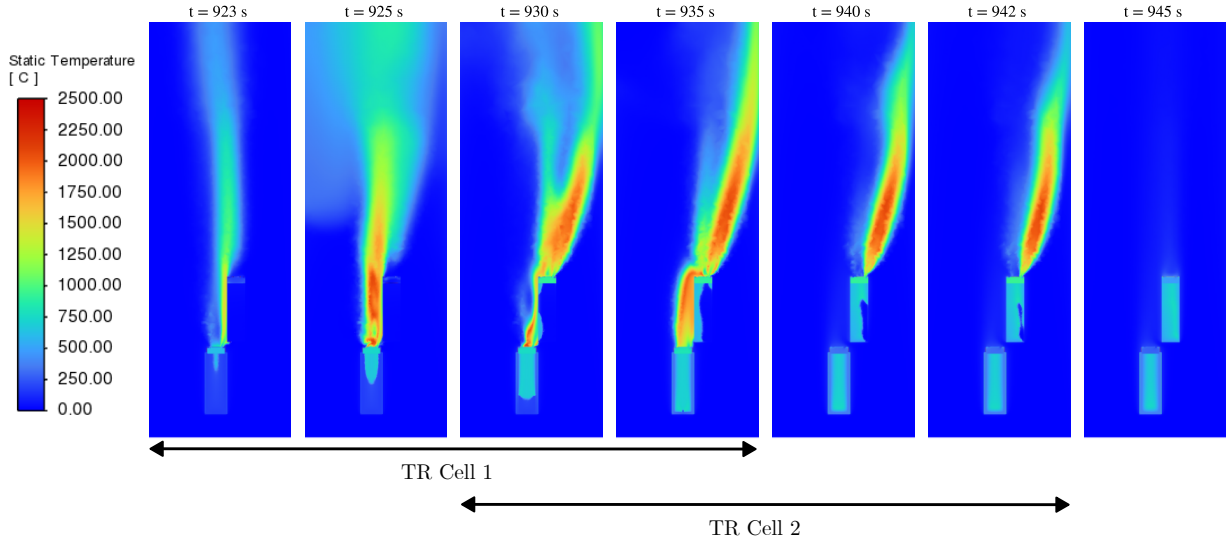

Figure 4.22 - Contours of temperature at different times during TRs

The heat release rate generated by the cells is shown in Figure 4.23. The gas-phase heat release rate is computed using the oxygen consumption method, thereby including contributions from both cells. The HRR profile of cell 1 is similar to that of the single-cell model. However, cell 2 exhibits a different HRR profile that can be divided into two phases: a sustained increase from $t = 926$ s to $t = 933$ s, followed by a slower decrease until the end at $t = 943$ s. The peak of solid phase heat release of Cell 2 matches the intensity of the second peak observed in Cell 1. This difference in profile can be explained by the heating applied to the cells: cell 1 is heated gradually and uniformly by the copper tube, while cell 2 is heated by the hot gas on only one side of its case. The gas-phase HRR follows a profile that resembles a combination of the solid-phase HRR profiles of both cells.

These preliminary results show the model's ability to handle several cells at the same time.

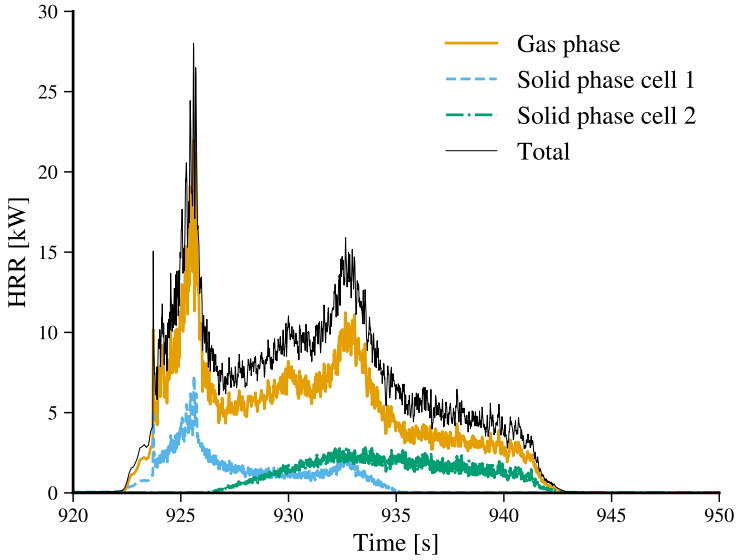

Figure 4.23 - Heat release rate during the TR of the two cells

In the two-cell configuration, computational costs did not significantly increase compared to the single-cell setup, as a similar mesh was used. Figure 4.24 shows the cost distribution: half of the computational cost is attributed to the coupled RANS equations, 22.8% to the transport of the mixture fraction and its variance as well as reading the PDF table, 15.2% to solving the energy equations, and 10.3% to the turbulence model. The thermal abuse, gas generation, and radiation models account for around 0.2% of the costs. From this distribution, we can conclude that adding more cells should not significantly increase computational costs, as flow model equations are not solved within these solid zones. However, increasing the number of cells may necessitate an extension of the computational domain, potentially leading to higher overall costs.

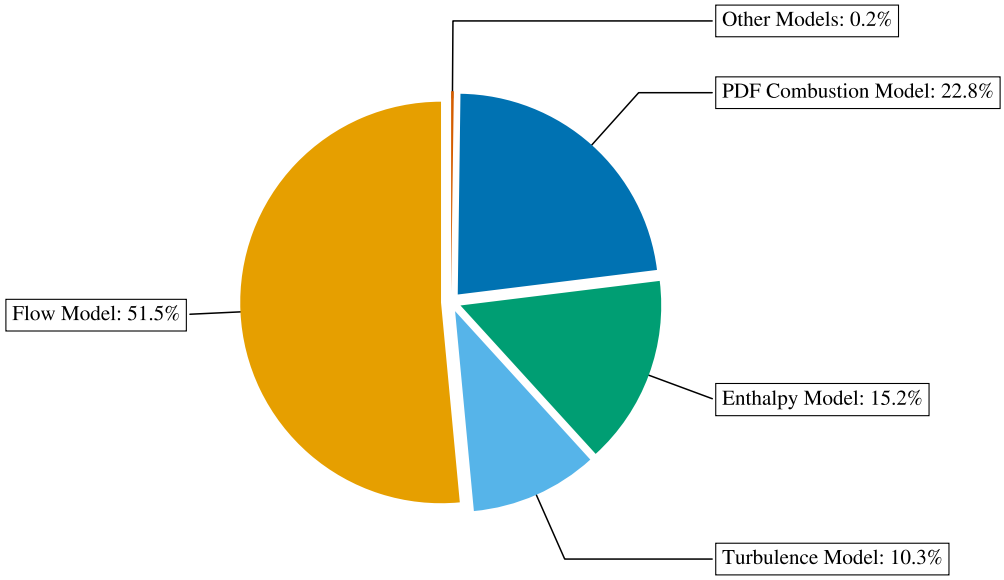

Figure 4.24 - Computational costs repartition when modeling two cells. The "Other Models" category includes the thermal abuse, gas generation, and radiation models

4.4.3 Critical analysis

Certain aspects of the thermal runaway phenomenon are absent in this model compared to the single-cell model, specifically venting and the variable jellyroll density. Venting can be easily implemented by using a second SCHEME. However, implementing variable jellyroll density requires a more complex UDF to ensure that the correct value of c_{elec} is applied to each cell. Additionally, a mesh and timestep independence study must be conducted before validating the results.

CHAPTER 5 CONCLUSION

5.1 Summary

In this work, a 3D, multi-physics, fully coupled numerical simulation framework is presented. It is developed on the commercial CFD solver Ansys FLUENT and integrates internal reactions (leading to heat and gas generation), venting, and combustion. The different phenomena are included using published models either already implemented in Fluent (as of the 2024R1 release: heat generation, combustion, and radiation) or through manual implementation, such as gas generation. The framework is used to study the thermal runaway of a specific 18650 NMC cell induced by overheating; comparing its prediction with experimental data acquired in-house using calorimeters. The results show a good agreement on the case temperature and give a heat release rate within the same order of magnitude. However, the thermal runaway calculated numerically remains shorter and stronger than experimentally observed.

Additionally, the different turbulent combustion models are studied based on their ignition process and heat release rate calculation. This comparison shows the complexity of turbulent combustion modeling in a RANS setup. The non-premixed approach with steady diffusion was selected for the full simulation as it acts as the worst-case scenario for the heat release rate and heavily reduces the computational cost. However, it also presents some weaknesses, primarily in the ignition and heat release rate computation during the first seconds of TR. Finally, the model was used in a two-cell configuration showing its ability to capture propagation inside a battery pack.

5.2 Discussion of the results and limitations

The model can be improved in several areas, divided into three categories: numerical optimizations, in-depth modeling, and additional phenomena. Numerical optimizations include further refinement of the timestep size and the implementation of numerical methods to reduce the stiffness of thermal abuse reactions. Employing automatic adaptive time-stepping, rather than fixed adjustments, can also improve numerical accuracy.

The in-depth modeling category focuses on refining parameters within the existing models. For heat generation, thermal abuse parameters vary with component composition; each cell model from a specific manufacturer utilizes unique chemistry, necessitating the calculation of new thermal abuse parameters to better match experimental data. For the gas generation

model, the quantity and composition of gases produced must be adapted to the specific cell, and the distribution of the amount across reactions requires further analysis. The venting process can be improved by incorporating a more detailed cell geometry that includes all components of the top part. Exploring alternative combustion models, such as the Transport PDF model, would allow further comparisons of available approaches. Radiation modeling could be improved with more accurate approaches such as the Discrete Ordinates or the Monte-Carlo models, both of which account for radiation from burning gases.

Finally, this work can be enhanced by incorporating additional thermal runaway phenomena, such as the venting of solid ejecta and the evaporation of liquid electrolytes. These phenomena can be included either through user-defined functions or by utilizing the available models in Fluent. The latter approach will maintain the framework's flexibility, but it is dependent upon the availability of models in Fluent.

The work is also constrained by the implementation of the available models in ANSYS Fluent. As a commercial solver, it operates as a "black box", and the lack of transparency regarding the precise equations being solved poses a challenge to fully understanding certain behaviors of the model.

5.3 Impact and outlook

The combination of the different available models in Ansys Fluent implemented in this work enabled the accurate modeling of the thermal runaway phenomenon in a lithium-ion cell. The proposed framework is adaptable for industrial use, allowing modifications to model other cell chemistry or geometries. It can also be scaled and extended to investigate the propagation of thermal runaway within battery packs, where each cell is capable of undergoing a fully modeled thermal runaway.

Numerical models of TR are already available in the literature with some of them including all the main phenomena. However, to our knowledge, this work is the first to use the reduced-order approach for turbulent combustion modeling with a detailed mechanism in conjunction with solid-phase models. Furthermore, this framework is scalable and doesn't rely on user-defined functions to include part of the thermal runaway. Additionally, a comparison of the different combustion models is presented, which, together with the use of reduced-order models, opens a discussion on the most suitable model for battery fires, highlighting the trade-off between accuracy and computational costs. Finally, the dynamics of the main thermal runaway event are studied from the perspective of heat release rate, as this metric is crucial in fire safety studies but not included in most numerical studies of thermal runaway.

REFERENCES

[1] U. N. D. of Economics and S. Affairs, "Frontier Technology Issues: Lithium-ion batteries: a pillar for a fossil fuel-free economy?" 2021.

[2] M. Yuan, J. Z. Thellufsen, H. Lund, and Y. Liang, "The electrification of transportation in energy transition," *Energy*, vol. 236, p. 121564, Dec. 2021.

[3] IEA, "CO2 Emissions in 2022 – Analysis," Mar. 2023. [Online]. Available: https://www.iea.org/reports/co2-emissions-in-2022

[4] J. B. Goodenough, "Energy storage materials: A perspective," *Energy Storage Materials*, vol. 1, pp. 158–161, 2015.

[5] J. Tarascon and M. Armand, "Issues and Challenges Facing Rechargeable Lithium Batteries," *Nature*, vol. 414, pp. 359–67, Dec. 2001.

[6] R. A. Marsh, S. Vukson, S. Surampudi, B. V. Ratnakumar, M. C. Smart, M. Manzo, and P. J. Dalton, "Li ion batteries for aerospace applications," *Journal of Power Sources*, vol. 97-98, pp. 25–27, Jul. 2001.

[7] A. Yoshino, "The birth of the lithium-ion battery," vol. 51, no. 24, pp. 5798–5800.

[8] IEA, "Batteries and Secure Energy Transitions – Analysis," Paris, Tech. Rep., Apr. 2024, licence: CC BY 4.0.

[9] EVO report 2024 | BloombergNEF | bloomberg finance LP. [Online]. Available: https://about.bnef.com/electric-vehicle-outlook/

[10] A. W. Golubkov, S. Scheikl, R. Planteu, G. Voitic, H. Wiltsche, C. Stangl, G. Fauler, A. Thaler, and V. Hacker, "Thermal runaway of commercial 18650 Li-ion batteries with LFP and NCA cathodes – impact of state of charge and overcharge," *RSC Advances*, vol. 5, no. 70, pp. 57 171–57 186, Jun. 2015.

[11] V. Etacheri, R. Marom, R. Elazari, G. Salitra, and D. Aurbach, "Challenges in the development of advanced Li-ion batteries: a review," *Energy & Environmental Science*, vol. 4, no. 9, pp. 3243–3262, Aug. 2011.

[12] P. Arora and Z. J. Zhang, "Battery Separators," *Chemical Reviews*, vol. 104, no. 10, pp. 4419–4462, Oct. 2004.

[13] S. Abada, "Compréhension et modélisation de l'emballement thermique de batteries Li-ion neuves et vieillies," Ph.D. dissertation, Université Pierre et Marie Curie - Paris VI, 2016.

[14] P. Verma, P. Maire, and P. Novák, "A review of the features and analyses of the solid electrolyte interphase in Li-ion batteries," *Electrochimica Acta*, vol. 55, no. 22, pp. 6332–6341, Sep. 2010.

[15] Q. Wang, P. Ping, X. Zhao, G. Chu, J. Sun, and C. Chen, "Thermal runaway caused fire and explosion of lithium ion battery," *Journal of Power Sources*, vol. 208, pp. 210–224, jun 2012.

[16] X. Feng, M. Ouyang, X. Liu, L. Lu, Y. Xia, and X. He, "Thermal runaway mechanism of lithium ion battery for electric vehicles: A review," *Energy Storage Materials*, vol. 10, pp. 246–267, Jan. 2018.

[17] "Events with smoke, fire, extreme heat or explosion involving lithium batteries." Federal Aviation Administration, Tech. Rep., 2022.

[18] S. Mallick and D. Gayen, "Thermal behaviour and thermal runaway propagation in lithium-ion battery systems – A critical review," *Journal of Energy Storage*, vol. 62, p. 106894, Jun. 2023.

[19] C. F. Lopez, J. A. Jeevarajan, and P. P. Mukherjee, "Experimental Analysis of Thermal Runaway and Propagation in Lithium-Ion Battery Modules," *Journal of The Electrochemical Society*, vol. 162, no. 9, p. A1905, Jul. 2015.

[20] NTSB, "Auto Manufacturers Incorporating NTSB Recommendation on Electric Vehicles." [Online]. Available: https://www.ntsb.gov/news/press-releases/Pages/NR20220601.aspx

[21] T. Rappsilber, N. Yusfi, S. Krüger, S.-K. Hahn, T.-P. Fellinger, J. Krug von Nidda, and R. Tschirschwitz, "Meta-analysis of heat release and smoke gas emission during thermal runaway of lithium-ion batteries," *Journal of Energy Storage*, vol. 60, p. 106579, Apr. 2023.

[22] H. Löbberding, S. Wessel, C. Offermanns, M. Kehrer, J. Rother, H. Heimes, and A. Kampker, "From cell to battery system in BEVs: Analysis of system packing efficiency and cell types," *World Electric Vehicle Journal*, vol. 11, no. 4, p. 77, Dec. 2020.

[23] S. Link, C. Neef, and T. Wicke, "Trends in automotive battery cell design: A statistical analysis of empirical data," *Batteries*, vol. 9, no. 5, p. 261, May 2023.

[24] B. Scrosati and J. Garche, "Lithium batteries: Status, prospects and future," *Journal of Power Sources*, vol. 195, no. 9, pp. 2419–2430, 2010.

[25] M. Wakihara, "Recent developments in lithium ion batteries," *Materials Science and Engineering: R: Reports*, vol. 33, no. 4, pp. 109–134, Jun. 2001.

[26] M. Greenwood, M. Wentker, and J. Leker, "A region-specific raw material and lithium-ion battery criticality methodology with an assessment of NMC cathode technology," *Applied Energy*, vol. 302, p. 117512, Nov. 2021.

[27] C. Pillot, "The Rechargeable Battery Market and Main Trends 2011-2020," 2017.

[28] C. Essl, A. W. Golubkov, and A. Fuchs, "Comparing Different Thermal Runaway Triggers for Two Automotive Lithium-Ion Battery Cell Types," *Journal of The Electrochemical Society*, vol. 167, no. 13, p. 130542, Oct. 2020.

[29] N. Ponchaut, F. Colella, R. Spray, and Q. Horn, "Thermal Management Modeling for Avoidance of Thermal Runaway Conditions in Lithium-Ion Batteries," *SAE Technical Papers*, vol. 1, Apr. 2014.

[30] V. Goupil, "Analysis and modelling of Li-ion cells degassing and combustion under thermal runaway," Master's thesis, Ecole Polytechnique de Montréal, 2021.

[31] J. K. Ostanek, W. Li, P. P. Mukherjee, K. R. Crompton, and C. Hacker, "Simulating onset and evolution of thermal runaway in Li-ion cells using a coupled thermal and venting model," *Applied Energy*, vol. 268, p. 114972, Jun. 2020.

[32] B. Xu, L. Kong, G. Wen, and M. G. Pecht, "Protection Devices in Commercial 18650 Lithium-Ion Batteries," *IEEE Access*, vol. 9, pp. 66 687–66 695, 2021.

[33] M. A. Manzo, J. C. Brewer, R. V. Bugga, E. C. Darcy, J. A. Jeevarajan, B. I. McKissock, and P. C. Schmitz, "NASA Aerospace Flight Battery Program: Generic Safety, Handling and Qualification Guidelines for Lithium-Ion (Li-Ion) Batteries; Availability of Source Materials for Lithium-Ion (Li-Ion) Batteries; Maintaining Technical Communications Related to Aerospace Batteries (NASA Aerospace Battery Workshop)," Tech. Rep. NESC-RP-08-75, Aug. 2010.

[34] W. Li, K. R. Crompton, C. Hacker, and J. K. Ostanek, "Comparison of Current Interrupt Device and Vent Design for 18650 Format Lithium-ion Battery Caps," *Journal of Energy Storage*, vol. 32, p. 101890, Dec. 2020.

[35] F. Austin Mier, M. J. Hargather, and S. R. Ferreira, "Experimental Quantification of Vent Mechanism Flow Parameters in 18650 Format Lithium Ion Batteries," *Journal of Fluids Engineering*, vol. 141, no. 061403, Apr. 2019.

[36] A. W. Golubkov, D. Fuchs, J. Wagner, H. Wiltsche, C. Stangl, G. Fauler, G. Voitic, A. Thaler, and V. Hacker, "Thermal-runaway experiments on consumer Li-ion batteries with metal-oxide and olivin-type cathodes," *RSC Advances*, vol. 4, no. 7, pp. 3633–3642, Dec. 2013.

[37] L. Yuan, T. Dubaniewicz, I. Zlochower, R. Thomas, and N. Rayyan, "Experimental study on thermal runaway and vented gases of lithium-ion cells," *Process Safety and Environmental Protection*, vol. 144, pp. 186–192, Dec. 2020.

[38] S. Chen, Z. Wang, J. Wang, X. Tong, and W. Yan, "Lower explosion limit of the vented gases from Li-ion batteries thermal runaway in high temperature condition," *Journal of Loss Prevention in the Process Industries*, vol. 63, p. 103992, Jan. 2020.

[39] Gully, "Technical Reference for Li-ion Battery Explosion Risk and Fire Suppression DNV," DNV, Tech. Rep., 2019.

[40] H. Yan and O. A. Ezekoye, "State of charge effects on active material elemental composition changes between pre-thermal-runaway and post-failure states for 8-1-1 nickel-manganese-cobalt 18650 cells," *Journal of Energy Storage*, vol. 63, p. 106974, Jul. 2023.

[41] M. Lammer, A. Königseder, P. Gluschitz, and V. Hacker, "Influence of aging on the heat and gas emissions from commercial lithium ion cells in case of thermal failure," *Journal of Electrochemical Science and Engineering*, vol. 8, no. 1, pp. 101–110, Mar. 2018.

[42] S. Koch, A. Fill, and K. P. Birke, "Comprehensive gas analysis on large scale automotive lithium-ion cells in thermal runaway," *Journal of Power Sources*, vol. 398, pp. 106–112, Sep. 2018.

[43] I. Belharouak, W. Lu, D. Vissers, and K. Amine, "Safety characteristics of Li(Ni0.8Co0.15Al0.05)O2 and Li(Ni1/3Co1/3Mn1/3)O2," *Electrochemistry Communications*, vol. 8, no. 2, pp. 329–335, Feb. 2006.

[44] P. Ribière, S. Grugeon, M. Morcrette, S. Boyanov, S. Laruelle, and G. Marlair, "Investigation on the fire-induced hazards of Li-ion battery cells by fire calorimetry," *Energy & Environmental Science*, vol. 5, no. 1, pp. 5271–5280, Jan. 2012.

[45] J. Sun, J. Li, T. Zhou, K. Yang, S. Wei, N. Tang, N. Dang, H. Li, X. Qiu, and L. Chen, "Toxicity, a serious concern of thermal runaway from commercial Li-ion battery," *Nano Energy*, vol. 27, pp. 313–319, Sep. 2016.

[46] R. Spotnitz and J. Franklin, "Abuse behavior of high-power, lithium-ion cells," *Journal of Power Sources*, vol. 113, no. 1, pp. 81–100, Jan. 2003.

[47] R. Zhao, Z. Lai, W. Li, M. Ye, and S. Yu, "Development of a coupled model of heat generation and jet flow of lithium-ion batteries during thermal runaway," *Journal of Energy Storage*, vol. 63, 2023.

[48] "AVBP website - CERFACS." [Online]. Available: https://cerfacs.fr/avbp7x/#

[49] G.-H. Kim, A. Pesaran, and R. Spotnitz, "A three-dimensional thermal abuse model for lithium-ion cells," *Journal of Power Sources*, vol. 170, no. 2, pp. 476–489, Jul. 2007.

[50] P. T. Coman, S. Rayman, and R. E. White, "A lumped model of venting during thermal runaway in a cylindrical Lithium Cobalt Oxide lithium-ion cell," *Journal of Power Sources*, vol. 307, pp. 56–62, Mar. 2016.

[51] P. T. Coman, S. Mátéfi-Tempfli, C. T. Veje, and R. E. White, "Modeling Vaporization, Gas Generation and Venting in Li-Ion Battery Cells with a Dimethyl Carbonate Electrolyte," *Journal of The Electrochemical Society*, vol. 164, no. 9, p. A1858, Jul. 2017.

[52] J. Kim, A. Mallarapu, D. P. Finegan, and S. Santhanagopalan, "Modeling cell venting and gas-phase reactions in 18650 lithium ion batteries during thermal runaway," *Journal of Power Sources*, vol. 489, 2021.

[53] D. Mishra, K. Shah, and A. Jain, "Investigation of the Impact of Flow of Vented Gas on Propagation of Thermal Runaway in a Li-Ion Battery Pack," *Journal of the Electrochemical Society*, vol. 168, no. 6, 2021.

[54] D. Mishra, P. Zhao, and A. Jain, "Thermal Runaway Propagation in Li-ion Battery Packs Due to Combustion of Vent Gases," *Journal of the Electrochemical Society*, vol. 169, no. 10, 2022.

[55] A. Cellier, F. Duchaine, T. Poinsot, G. Okyay, M. Leyko, and M. Pallud, "An analytically reduced chemistry scheme for large eddy simulation of lithium-ion battery fires," *Combustion and Flame*, vol. 250, p. 112648, Apr. 2023.

[56] J. K. Ostanek, M. Parhizi, W. Li, G. Kilaz, and K. R. Crompton, "CFD-Based Thermal Abuse Simulations including Gas Generation and Venting of an 18650 Li-Ion Battery Cell," *Journal of The Electrochemical Society*, vol. 170, no. 9, p. 090512, Sep. 2023.

[57] P. Zhang, J. Lu, K. Yang, H. Chen, and Y. Huang, "A 3d simulation model of thermal runaway in li-ion batteries coupled particles ejection and jet flow," *Journal of Power Sources*, vol. 580, p. 233357, Oct. 2023.

[58] J. K. Ostanek, N. R. Baehl, M. Parhizi, and J. A. Jeevarajan, "Hot gas impingement and radiation on neighboring surfaces from venting and combustion in a package of 18650 cells," *Journal of Power Sources Advances*, vol. 28, p. 100150, Aug. 2024.

[59] T. Echekki and E. Mastorakos, Eds., *Turbulent Combustion Modeling: Advances, New Trends and Perspectives*, ser. Fluid Mechanics and Its Applications. Dordrecht: Springer Netherlands, 2011, vol. 95.

[60] T. Poinsot and D. Veynante, *Theoretical and Numerical Combustion*, third edition ed., 2006.

[61] T. D. Hatchard, D. D. MacNeil, A. Basu, and J. R. Dahn, "Thermal Model of Cylindrical and Prismatic Lithium-Ion Cells," *Journal of The Electrochemical Society*, vol. 148, no. 7, p. A755, Jun. 2001.

[62] A. Melcher, C. Ziebert, M. Rohde, and H. J. Seifert, "Modeling and Simulation of the Thermal Runaway Behavior of Cylindrical Li-Ion Cells—Computing of Critical Parameters," *Energies*, vol. 9, no. 4, p. 292, apr 2016.

[63] P. T. Coman, E. C. Darcy, C. T. Veje, and R. E. White, "Modelling Li-Ion Cell Thermal Runaway Triggered by an Internal Short Circuit Device Using an Efficiency Factor and Arrhenius Formulations," *Journal of The Electrochemical Society*, vol. 164, no. 4, pp. A587–A593, 2017.

[64] C.-Y. Jhu, Y.-W. Wang, C.-Y. Wen, C.-C. Chiang, and C.-M. Shu, "Self-reactive rating of thermal runaway hazards on 18650 lithium-ion batteries," *Journal of Thermal Analysis and Calorimetry*, vol. 106, no. 1, pp. 159–163, Oct. 2011.

[65] E. P. Roth and C. J. Orendorff, "How Electrolytes Influence Battery Safety," *The Electrochemical Society Interface*, vol. 21, no. 2, p. 45, Jan. 2012.

[66] V. Goupil, C. Gaya, A. Boisard, and E. Robert, "Effect of the heating rate on the degassing and combustion of cylindrical Li-Ion cells," *Fire Safety Journal*, vol. 133, p. 103648, Oct. 2022.

[67] W. Li, V. Leon Quiroga, K. Crompton, and J. K. Ostanek, "High Resolution 3-D Simulations of Venting in 18650 Lithium-Ion Cells," *Frontiers in Energy Research*, vol. 9, 2021.

[68] D. Veynante and L. Vervisch, "Turbulent combustion modeling," *Progress in Energy and Combustion Science*, vol. 28, no. 3, pp. 193–266, Mar. 2002.

[69] B. F. Magnussen and B. H. Hjertager, "On mathematical modeling of turbulent combustion with special emphasis on soot formation and combustion," *Symposium (International) on Combustion*, vol. 16, no. 1, pp. 719–729, Jan. 1977.

[70] B. Magnussen, "On the structure of turbulence and a generalized eddy dissipation concept for chemical reaction in turbulent flow," in *19th Aerospace Sciences Meeting*. American Institute of Aeronautics and Astronautics, 1981.

[71] M. Ferrarotti, Z. Li, and A. Parente, "On the role of mixing models in the simulation of MILD combustion using finite-rate chemistry combustion models," *Proceedings of the Combustion Institute*, vol. 37, no. 4, pp. 4531–4538, Jan. 2019.

[72] M. J. Evans, C. Petre, P. R. Medwell, and A. Parente, "Generalisation of the eddy-dissipation concept for jet flames with low turbulence and low Damköhler number," *Proceedings of the Combustion Institute*, vol. 37, no. 4, pp. 4497–4505, Jan. 2019.

[73] Y. R. Sivathanu and G. M. Faeth, "Generalized state relationships for scalar properties in nonpremixed hydrocarbon/air flames," *Combustion and Flame*, vol. 82, no. 2, pp. 211–230, nov 1990.

[74] N. Peters, "Laminar diffusion flamelet models in non-premixed turbulent combustion," *Progress in Energy and Combustion Science*, vol. 10, no. 3, pp. 319–339, Jan. 1984.

[75] F. A. Williams, *Combustion Theory*, 2nd ed. Boca Raton: CRC Press, May 2019.

[76] A. Y. Klimenko, "Multicomponent diffusion of various admixtures in turbulent flow," *Fluid Dynamics*, vol. 25, no. 3, pp. 327–334, May 1990.

[77] H. Barths, N. Peters, N. Brehm, A. Mack, M. Pfitzner, and V. Smiljanovski, "Simulation of pollutant formation in a gas-turbine combustor using unsteady flamelets," *Symposium (International) on Combustion*, vol. 27, no. 2, pp. 1841–1847, Jan. 1998.

[78] M. Henriksen, K. Vaagsaether, J. Lundberg, S. Forseth, and D. Bjerketvedt, "Simulation of a premixed explosion of gas vented during Li-ion battery failure," *Fire Safety Journal*, vol. 126, p. 103478, Dec. 2021.

[79] J. V. Oijen and L. D. Goey, "Modelling of Premixed Laminar Flames using Flamelet-Generated Manifolds," *Combustion Science and Technology*, vol. 161, no. 1, pp. 113–137, Dec. 2000.

[80] L. Wang, Z. Liu, S. Chen, and C. Zheng, "Comparison of Different Global Combustion Mechanisms Under Hot and Diluted Oxidation Conditions," *Combustion Science and Technology*, vol. 184, no. 2, pp. 259–276, Feb. 2012.

[81] C. K. WESTBROOK and F. L. DRYER, "Simplified Reaction Mechanisms for the Oxidation of Hydrocarbon Fuels in Flames," *Combustion Science and Technology*, vol. 27, no. 1-2, pp. 31–43, Dec. 1981.

[82] W. Q. Walker, J. J. Darst, D. P. Finegan, G. A. Bayles, K. L. Johnson, E. C. Darcy, and S. L. Rickman, "Decoupling of heat generated from ejected and non-ejected contents of 18650-format lithium-ion cells using statistical methods," *Journal of Power Sources*, vol. 415, pp. 207–218, Mar. 2019.

[83] C. M. R. Vendra, A. V. Shelke, J. E. H. Buston, J. Gill, D. Howard, E. Read, A. Abaza, B. Cooper, and J. X. Wen, "Numerical and experimental characterisation of high energy density 21700 lithium-ion battery fires," *Process Safety and Environmental Protection*, vol. 160, pp. 153–165, Apr. 2022.

[84] ""Chemical-Kinetic Mechanisms for Combustion Applications", San Diego Mechanism web page, Mechanical and Aerospace Engineering (Combustion Research), University of California at San Diego." [Online]. Available: http://combustion.ucsd.edu

[85] J. R. Howell, M. P. Mengüc, K. Daun, and R. Siegel, *Thermal Radiation Heat Transfer*, 7th ed. Boca Raton: CRC Press, Dec. 2020.

[86] K. Stoll, K. Crompton, W. Li, and J. K. Ostanek, "K2 18650 Vent Cap CT Scans."

[87] T.-H. Shih, W. W. Liou, A. Shabbir, Z. Yang, and J. Zhu, "A new k-ϵ eddy viscosity model for high reynolds number turbulent flows," *Computers & Fluids*, vol. 24, no. 3, pp. 227–238, Mar. 1995.

[88] R. A. W. M. Henkes, F. F. Van Der Vlugt, and C. J. Hoogendoorn, "Natural-convection flow in a square cavity calculated with low-Reynolds-number turbulence models," *International Journal of Heat and Mass Transfer*, vol. 34, no. 2, pp. 377–388, Feb. 1991. [Online]. Available: https://www.sciencedirect.com/science/article/pii/001793109190258G

[89] S. Sarkar and B. Lakshmanan, "Application of a Reynolds stress turbulence model to the compressible shear layer," *AIAA Journal*, vol. 29, no. 5, pp. 743–749, May 1991, publisher: American Institute of Aeronautics and Astronautics.

[90] Ansys Inc, "ANSYS Fluent Theory Guide, Release 24.1," 2024.

[91] K. Bray, P. Domingo, and L. Vervisch, "Role of the progress variable in models for partially premixed turbulent combustion," *Combustion and Flame*, vol. 141, no. 4, pp. 431–437, Jun. 2005.

[92] P. Peng and F. Jiang, "Thermal safety of lithium-ion batteries with various cathode materials: A numerical study," *International Journal of Heat and Mass Transfer*, vol. 103, pp. 1008–1016, Dec. 2016.

[93] W. Thornton, "XV. The relation of oxygen to the heat of combustion of organic compounds," *The London, Edinburgh, and Dublin Philosophical Magazine and Journal of Science*, vol. 33, no. 194, pp. 196–203, Feb. 1917.

[94] C. Huggett, "Estimation of rate of heat release by means of oxygen consumption measurements," *Fire and Materials*, vol. 4, no. 2, pp. 61–65, 1980.

[95] M.-A. Bérubé, P. Versailles, B. Savard, and E. Robert, "High temporal resolution sensible enthalpy and oxygen consumption calorimeter," *CICS 2024*, 2024.

[96] "The Scheme Programming Language." [Online]. Available: https://www.scheme.org/

[97] RTCA, "RTCA DO-311 - Minimum Operational Performance Standards for Rechargeable Lithium Batteries and Battery Systems | GlobalSpec," 2017. [Online]. Available: https://standards.globalspec.com/std/10270501/RTCA%20DO-311

[98] J. Ostanek, M. Parhizi, and J. Jeevarajan, "A novel method for alleviating numerical stiffness in Li-ion thermal abuse models," *Journal of Power Sources Advances*, vol. 23, p. 100123, Aug. 2023.

[99] J. Kim, D. Kim, S. Lim, S. Lee, J. Oh, and G. Lee, "Accelerating simulations of Li-ion battery thermal runaway using modified Patankar–Runge–Kutta approach," *Applied Thermal Engineering*, vol. 251, p. 123518, Aug. 2024.

[100] I. O. for Standardization, "ISO 5660-1:2015 Reaction-to-fire tests - Heat release, smoke production and mass loss rate - Part 1: heat release rate (cone calorimeter method) and smoke production rate (dynamic measurement)," 2015.

[101] "ASME - VV20-Standard for Verification and Validation in Computational Fluid Dynamics and Heat Transfer," 2009.

APPENDIX A REALIZABLE K-EPSILON TURBULENCE MODEL

The computation of C_μ in the Realizable k-ϵ turbulence model is described below. Unlike in the other $k-\varepsilon$ models, C_μ is not constant. It is computed with:

$$C_\mu = \frac{1}{A_0 + A_s \frac{\tilde{k}U^*}{\tilde{\varepsilon}}} \tag{A.1}$$

where:

$$U^* \equiv \sqrt{S_{ij}S_{ji} + \widetilde{\Omega_{ij}}\widetilde{\Omega_{ij}}} \tag{A.2}$$

with:

$$\widetilde{\Omega_{ij}} = \Omega_{ij} - 2\varepsilon_{ijk}\omega_k$$

$$\Omega_{ij} = \overline{\Omega_{ij}} - 2\varepsilon_{ijk}\omega_k$$

$\overline{\Omega_{ij}}$ is the mean rate-of-rotation tensor viewed in a moving reference frame with the angular velocity ω_k. A_0 and A_S are two constants given by:

$$A_0 = 4.04$$

$$A_S = \sqrt{6}cos(\varphi)$$

where $\varphi = \frac{1}{3}cos^{-1}(\sqrt{6}W)$, $W = \frac{S_{ij}S_{jk}S_{ki}}{\tilde{S}^3}$, $\tilde{S} = \sqrt{S_{ij}S_{ij}}$.

APPENDIX B PARAMETRIC STUDY ON THERMAL ABUSE PARAMETERS.

This appendix presents the results of a parametric study on thermal abuse parameters. As defined in Chapter 3, the thermal abuse reactions are Arrhenius-type equations with the following form:

$$R = A \exp\left(\frac{-E}{\mathcal{R}\overline{T}}\right) c^m \tag{B.1}$$

where R [1/s] represents the reaction rate, A [1/s] is the frequency factor, E [J/mol] is the activation energy, $\mathcal{R}$ [J/mol/K] is the universal gas constant, c is a non-dimensional parameter, and m [-] is the order of reaction.

This appendix will focus on studying the pre-exponential factor and activation energy, as these are the primary user inputs in the thermal abuse model. The key quantities analyzed include the peak heat release rate due to thermal abuse reactions, the duration of thermal runaway, and the onset temperature. Here, the duration and onset temperature are defined as the period during which the cell generates more than 500 W of thermal power and the temperature at which the power generation first exceeds 500 W, respectively.

B.0.1 Pre-exponential factor

The pre-exponential factors control the overall dynamics of the reactions. Figure B.1 shows the heat release rate of the thermal abuse reaction and the case temperature at different values of pre-exponential factors. The values are taken from the work of Peng et al. [92] and are reduced gradually by a constant factor. Table B.1 gives the peak HRR reached, the thermal runaway duration, and the onset temperature for each tested value of A. A decrease in 10% of the base values leads to increasing the duration, and onset temperature by 1.3% and 0.25% respectively while decreasing the peak HRR by -4.8%. The total energy released remained constant. When reducing the values to 1% of the base values, the duration increased by 64.9%, the onset temperature increased by 32.6%, and the HRR peak decreased by -71.2%. Finally, with 0.01% of the initial values the duration is increased by 133% and peak HRR decreased by -86% but with an onset temperature 41% higher. Overall, decreasing all the pre-exponential factors tends to slow down the thermal abuse, the same amount of total energy is released over a longer period, leading to a lower power. However, the onset temperature greatly increases reaching values well above the values experimentally observed. Overall, the thermal runaway is not highly sensitive to the change of all pre-exponential

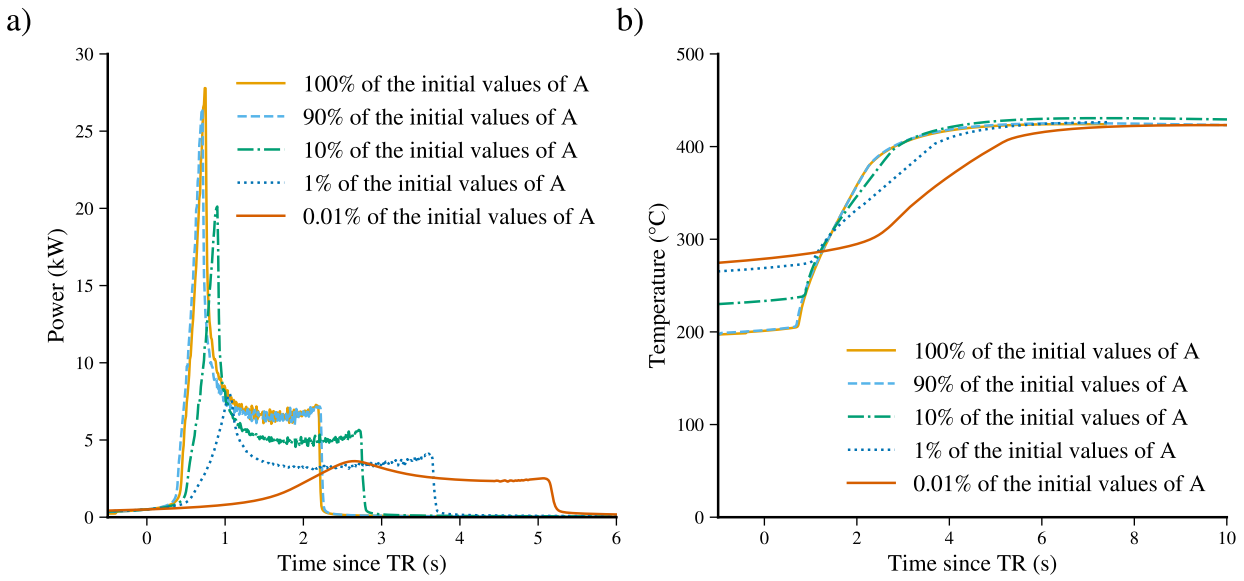

Figure B.1 a) Thermal abuse HRR and b) case temperature for different values of the pre-exponential factor

factors at the same time.

When studying the reactions individually, it is observed that not all reactions contribute equally to the thermal runaway. Depending on the initial value for c and the specific energy of the material, some reactions produce more energy. Figure B.2 shows the total energy released by each reaction based on the parameters given in Table 3.1. Additional work is required to isolate the effect of each reaction but the main driving reaction for heat generation are the Negative-solvent and Positive-Solvent reactions. For the main model presented in previous chapters, the pre-exponential factors were not modified from the work of Peng et al. [92].

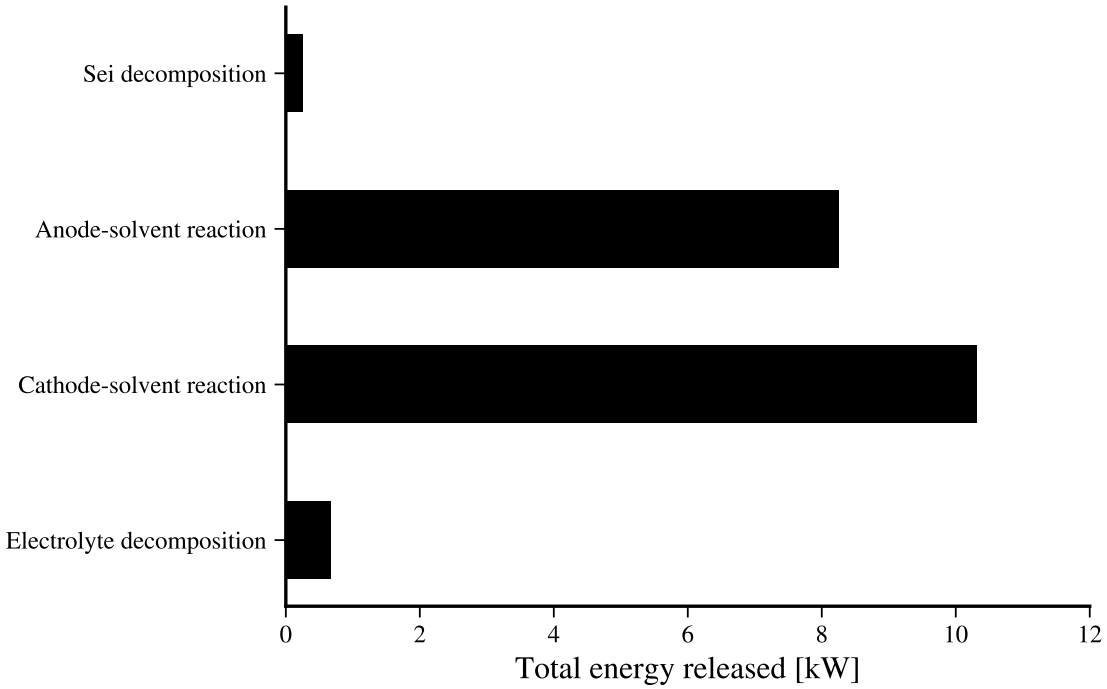

Figure B.2 - Energy released by each reaction

Table B.1 - Peak HRR, total energy released, thermal runaway duration, and onset temperature for different values of A

% of initial value used	Peak HRR [kW]	Total energy release [kJ]	Thermal runaway duration [s]	Onset temperature [°C]	
100	27.8	20.8	2.25	202.86	
90	26.5	20.8	2.28	203.37	
10	20.1	19.8	2.8	235.91	
1	8.0	3.7	18.47	3.7	269.09
0.01	3.6	18.3	5.25	286.82	

B.0.2 Activation energy

The activation energy mainly controls the onset temperature of the reaction. Figure B.3 shows the heat release rate of thermal energy for different values of the activation energy of the cathode-solvent reaction E_α. Only this reaction was investigated, as it is the one that releases the most energy. The activation energy highly impacts the duration of thermal runaway. Reducing the activation energy will result in a shorter, high-intensity TR as shown in Figure B.3. The activation energy factor can therefore be used to fine-tune the onset

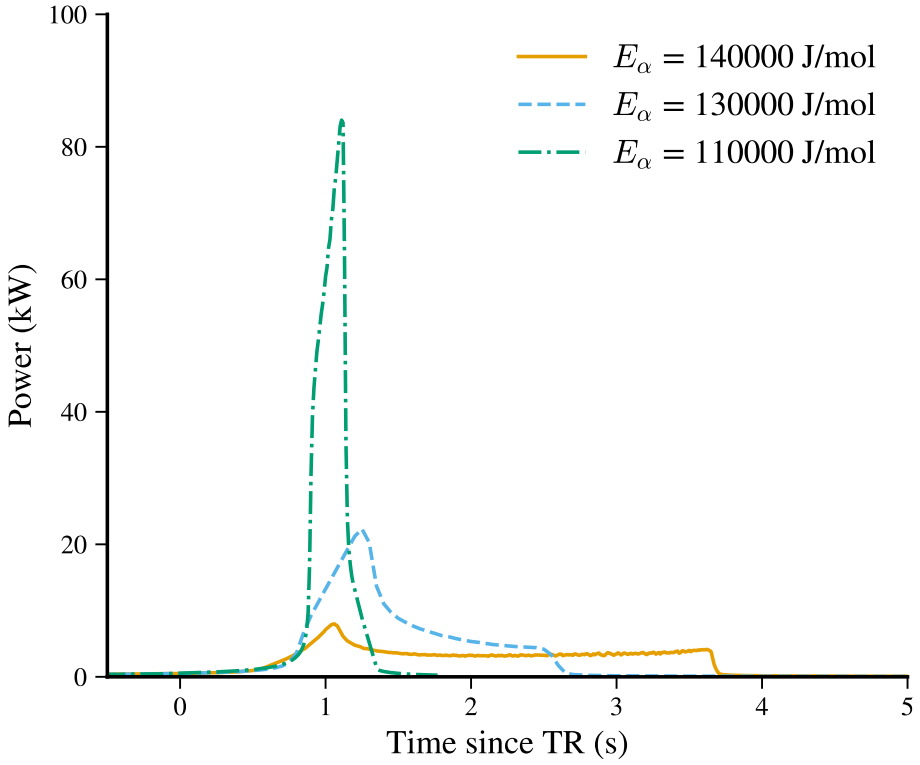

Figure B.3 - Thermal abuse HRR different values of the activation energy for the cathode-solvent reaction E_α

temperature. The value of E_α for an NMC given by Peng et al. [92] leads to an onset temperature of 220°C. Experimentally, the observed onset temperature of a 18650-25R is between 190°C-205°C. Several values of E_α were tested until the onset temperature was located in the middle experimental range. Tested values are given in Table B.2

For the main TR model, the selected value for E_α is 147500 J/mol.

Table B.2 - Onset temperature for different values of E

Value of E_α [J/mol]	Onset temperature [°C]
154000	220
150000	205
149500	203
147500	198

B.0.3 Additional parameters

This subsection addresses parameters that, while not directly related to the thermal abuse reactions, can influence thermal runaway behavior. The investigated parameters are the thermal conductivity and heat capacity of the jellyroll.

The jellyroll is composed of multiple material layers, making it cylindrically orthotropic or "cyl-orthotropic". According to the literature, the radial thermal conductivity is estimated to 0.8 W/m/K and the axial thermal conductivity to 20 W/m/K [52]. However, the cylindrical orthotropic formulation of thermal conductivity is not available when using a reduced-order combustion model. Due to this technical constraint, the isotropic formulation is used. Figure B.4 shows the thermal abuse heat release rate for a thermal conductivity of 20 W/m/K and 0.8 W/m/K. The axial thermal conductivity results in a thermal runaway that is three times shorter and twice as intense compared to the radial value. However, due to the jellyroll's layered structure, heat must traverse multiple material layers, making the radial conductivity value preferable, as it yields results closer to the cylindrical orthotropic formulation.

When the battery burns, thermal conductivity is expected to change, the melting of the separator increases conductivity as the metallic cathode and anode come into more direct contact, while the decomposition of the electrolyte may create gaseous voids within the cell, reducing heat conduction. Using the radial value provides a reasonable first approximation for thermal conductivity, though further work is needed to model the cyl-orthotropic formulation across combustion models. Additional experimental data is required to characterize thermal conductivity within the cell during thermal runaway.

The heat capacity also affects the thermal runaway dynamics. Figure B.5 shows the thermal abuse heat release rate with different heat capacities. The base value of 1000 J/kg/K used here and in the model is taken from the work of Kim et al. [52].

An increase of 5 % in heat capacity leads to only small variations in thermal runaway quantities: the duration is increased by 0.6% and onset temperature by +0.82°C. However, similar

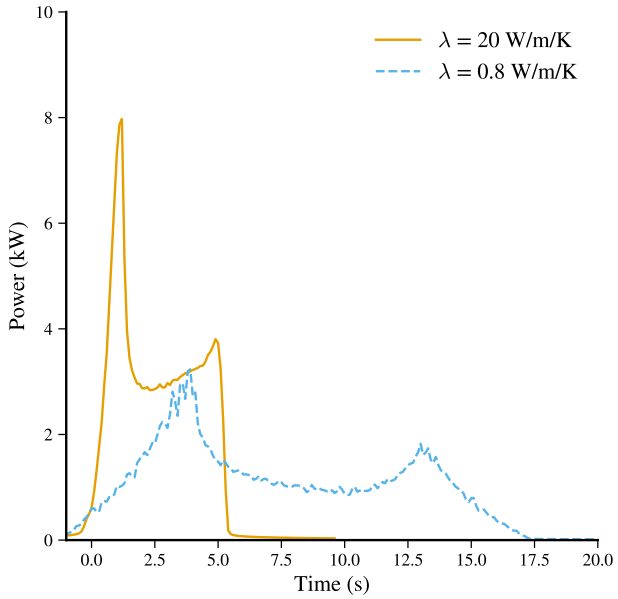

Figure B.4 - Thermal abuse heat release rate for a jellyroll thermal conductivity of 20 W/m/K and 0.8 W/m/K

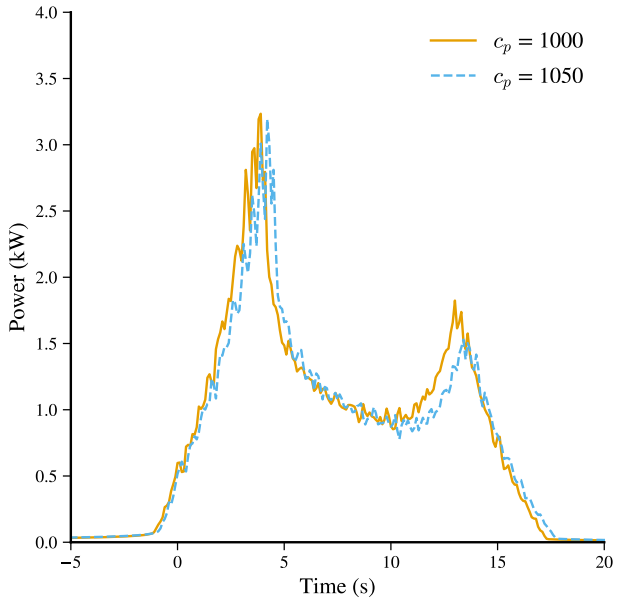

Figure B.5 - Thermal abuse heat release rate for a jellyroll heat capacity of 1000 J/kg/g and 1050 J/kg/K

to thermal conductivity, heat capacity is expected to change significantly during TR. Accurately modeling these parameters requires further numerical and experimental research to quantify these changes before adding them to numerical models.